Spontaneous Magnetic Flux Induced by Ferromagnetic π-Junctions

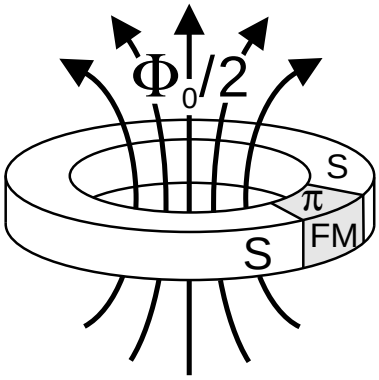

Dissertation
zur Erlangung des Doktorgrades
der Naturwissenschaften (Dr. rer. nat.)
der naturwissenschaftlichen Fakultät II - Physik
der Universität Regensburg

vorgelegt von
Andreas Bauer
aus Donaustauf

Januar 2005

Die Arbeit wurde von Prof. Dr. C. Strunk angeleitet.
Das Promotionsgesuch wurde am 13.1.2005 eingereicht.
Das Kolloquium fand am 17.3.2005 statt.

Prüfungsausschuss:	Vorsitzender:	Prof. Dr. K. F. Renk
	1. Gutachter:	Prof. Dr. C. Strunk
	2. Gutachter:	Prof. Dr. J. Keller
	weiterer Prüfer:	Prof. Dr. W. Wegscheider

Contents

Chapter 1

Motivation

If ferromagnets and superconductors are brought in good metallic contact, two types of order parameters compete at the interface: While in the ferromagnetic metal the spins of the electrons are preferably aligned in the same direction, in the classical (s-wave) superconductor the spinless Cooper-pairs are composed of two electrons with opposite spin (see Fig. 1.1). Naively, the antagonistic nature of the two order parameters forbids the coexistence of ferromagnetism and superconductivity. A closer look, however, reveals that this is not completely true:

The proximity effect is able to induce superconducting properties from a superconductor (S) into a ferromagnetic metal (F), but only limited to a short length-scale given by the coherence length in F. By fabricating SFS Josephson junctions with sufficiently small F layer thicknesses, even a supercurrent can flow across the ferromagnetic junction. For a certain thickness of the ferromagnetic layer, junctions with an intrinsic phase difference of π can be realized, which leads to interesting consequences.

Already in 1977 it was predicted by Bulaevskii that the ground state of a superconducting loop with a Josephson junction that contains magnetic impurities, is a state with nonzero current and magnetic flux equal to half a flux quantum [1]. This implies, that upon cooling such a loop below the critical temperature in zero field a spontaneous current is expected to arise. A necessary ingredient for the development of such a spontaneous current is that the Josephson junction is in the so called π-state, which is characterized by an intrinsic phase shift of the superconducting phase on both sides of the junction.

In 1994 Kirtley et al. have found a spontaneous magnetization of half a flux quantum measured by scanning SQUID (superconducting quantum interference device) microscopy in loops made of high-T_C superconductors with three incorporated grain

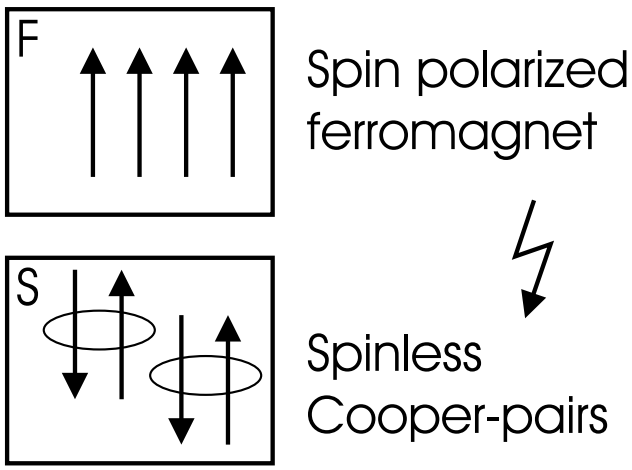

Figure 1.1: The antagonistic nature of the two competing order parameters in ferromagnets (F) and superconductors (S) naively forbids their coexistence. But under certain circumstances, combination of these two material systems can even *generate* current: By incorporating a π-junction in form of a thin ferromagnetic barrier in a superconducting loop, a spontaneous current is expected to arise (see cover picture).

boundary junctions [2, 3]. In these experiments, the direction dependence of the sign of the superconducting order parameter accounts for an intrinsic phase difference which results in the spontaneous flux.

Baselmans et al. found screening currents in a controllable π-SQUID at zero applied field. Controllable Josephson junctions are SNS junctions with two additional current leads to the normal region. By applying a voltage across these contacts, the junction can be switched from the 0 to the π-state [4].

The π-state in the ferromagnetic Josephson junctions, which are used in this work, is induced by the exchange splitting. According to Kontos et al., the dependence of the $R_N I_C$ product on the layer thickness is non-monotonic for the diluted ferromagnet PdNi. This is attributed to the occurrence of the π-state for certain F layer thicknesses in such junctions [5]. Guichard et al. used these ferromagnetic junctions to fabricate 0-π-SQUIDS (with one 0- and one π-junction) and observed a shift in the diffraction pattern when compared to 0-0 or π-π-SQUIDS [6].

While these experiments focused on the high temperature regime close to T_C, in this work the low temperature regime, where $LI_C \gg \Phi_0$, is investigated (L is the loop inductance, I_C the critical current and Φ_0 the flux quantum). A ferromagnetic π-junction is included in a superconducting loop , which is placed onto a microstructured Hall-sensor. With the Hall-sensor, the magnetic flux produced by the loop while cooling down is measured. The main result is the direct detection of a sponta-

neous magnetic flux produced by a superconducting loop containing a ferromagnetic π-junction [7].

This thesis is organized as follows: In chapter 2 the physics of ferromagnetic π-junctions and their consequences on flux quantization in a superconducting loop are discussed. In chapter 3 the preparation of the Hall-sensors and the superconducting loops is described; a detailed collection of recipes is given in Appendix A. Chapter 4 describes the measurement setup and presents the results. Finally, chapter 5 concludes and gives a brief outlook.

Chapter 2

Ferromagnetic π-Junctions

In this chapter, the basic theoretical concepts which are connected to this work are discussed. Section 2.1 describes some selected topics from the BCS theory of superconductivity. In section 2.2, the *proximity effect* is discussed for superconductor/normal metal (S/N) and superconductor/ferromagnetic metal (S/F) hybrid structures. Section 2.3 deals with the dc-Josephson effect and describes how the proximity effect in S/F structures can be exploited to fabricate π-junctions. Finally, in section 2.4, the concept of flux quantization is introduced and an interesting consequence for π-loops, the spontaneous supercurrent, is discussed.

2.1 Superconductivity

This section is intended to give an overview of the microscopic picture of superconductivity and to justify the description of superconductivity as macroscopic quantum state, used in the later sections. For this purpose, the corresponding chapters of the textbooks of Buckel [8] and Tinkham [9] are summarized.

The origin of conventional superconductivity is found in an attractive, phonon mediated electron-electron interaction, first described by Fröhlich and Bardeen in 1950/51. An important proof of it's relevance in the early stage of the formulation of this new attractive interaction was the influence of the atom mass on the superconducting transition temperature, the isotope effect. An illustrative model of the interaction can be given by the picture of two balls on a rubber membrane: Due to their mass, the balls will deform the rubber membrane, so that the balls are situated in valleys. If the two balls are in proximity it is plausible, that the energy of the system is lower when both balls are in the same valley opposed to the case where both balls are in separated valleys.

Analogous to this mechanical counterpart, an electron polarizes the atom lattice due to its negative charge. This polarization trace can be sensed by a second electron, which sees the accumulation of charge resulting from the first electron. This mechanism can be understood as an attractive electron-electron interaction and allows two electrons to lower their total energy. Cooper showed in 1956 that the Fermi sea is unstable against a small attractive interaction between electrons. In a superconductor, some electrons form pairs, they condense to *Cooper-pairs* and thereby lower the total energy of the system. The two electrons forming a Cooper-pair have opposite spin and opposite k-vectors.

Now that the formation of electron pairs is plausible, the question is addressed why all pairs are described by the same quantum mechanical state.

Starting point is the Fermi-sphere in k-space at T=0 which is formed by unpaired free electrons at T=0. Due to boundary conditions, the values of allowed k-states are quantized and according to the Fermi distribution at T=0, all states below k_F are occupied with probability 1, while all states with k> k_F are surely empty. The corresponding energies of the electrons are given by

$$\epsilon_k = \frac{\hbar^2}{2m}\left(k_x^2 + k_y^2 + k_z^2\right), \tag{2.1}$$

$\hbar = h/2\pi$, h is Planck's constant.

Now an constant attractive interaction between electrons $-V$ in an interval $\pm\hbar\omega_c$ around the Fermi energy ϵ_F is introduced. For electrons outside this interval the interaction shall be zero. The BCS theory states that because of this small attractive interaction, some electrons in a superconductor form Cooper-pairs which condense to a new state close to the Fermi-sphere, where the interaction is non-zero. In this area, pair-states are occupied with an probability $|v_k|^2$ and empty with an probability $|u_k|^2$ at the same time. The complex functions u_k and v_k obey the condition $|u_k|^2 + |v_k|^2 = 1$. The parameters u_k and v_k are derived by solving the Schrödinger equation of the system and minimizing the energy with respect to u_k and v_k:

$$|v_k|^2 = \frac{1}{2}\left[1 - \frac{\epsilon_k - E_F}{\sqrt{|\Delta|^2 + (\epsilon_k - E_F)^2}}\right] \tag{2.2}$$

$$|u_k|^2 = \frac{1}{2}\left[1 + \frac{\epsilon_k - E_F}{\sqrt{|\Delta|^2 + (\epsilon_k - E_F)^2}}\right] \tag{2.3}$$

E_F is the Fermi energy and the pair potential Δ is given by $\Delta = -V\sum_k u_k^* v_k = \Delta_0 e^{i\varphi}$ (Δ_0 is the energy gap). $F_k = u_k^* v_k$ is the pair amplitude.

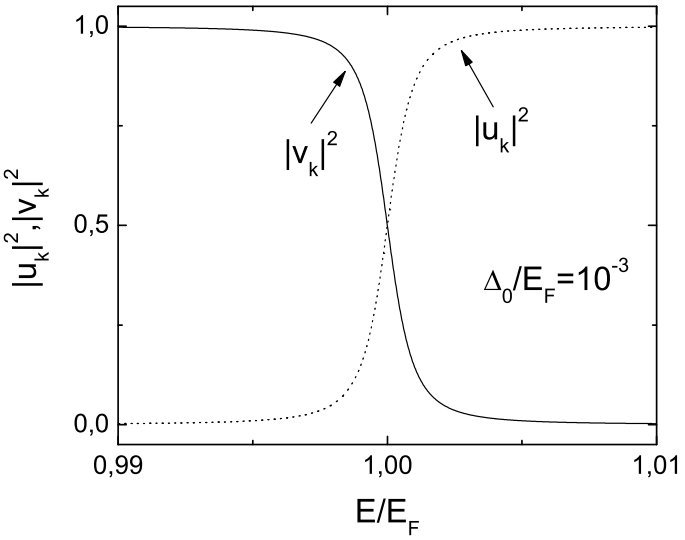

Figure 2.1: The probability to find a Cooper-pair at energy E/E_F at T=0 is given by $|v_k|^2$, the probability not to find Cooper-pair is given by $|u_k|^2$. Far below the Fermi energy $|v_k|^2$ is 1, far above it is 0. Only in an interval of the size of the energy gap around E_F, $|v_k|$ takes on values other than 1 and 0 [8].

The dependence of $|u_k|$ and $|v_k|$ on E/E_F for a typical metallic superconductor [1] is shown in Figure 2.1. Deep inside the Fermi sphere, the probability to find a Cooper-pair $|v_k|$ is almost 1, far above E_F it is almost zero. Only in an interval of size $\pm\Delta_0$ around the Fermi surface, both values of $|u_k|$ and $|v_k|$ deviate considerable from 1 and 0, and only the electrons located in this area of k-space contribute to the superconductivity.

The BCS ground state is composed starting from the vacuum state $|\phi_0\rangle$ in the language of the second quantization by,

$$|\Psi_G\rangle = \prod_{k=k_1 \ldots k_M} \left(u_k + v_k c^*_{k\uparrow} c^*_{-k\downarrow}\right) |\phi_0\rangle, \tag{2.4}$$

the operator $c^*_{k\uparrow}$ creates an electron with wave vector k and spin up.

In the BCS ground state, the physical properties of all Cooper-pairs are identical, which justifies the description by one single macroscopic wave function $\Psi = \Psi_0 e^{i\varphi}$, which will be used in section 2.4 for the flux quantization. The gain in energy resulting from the pairing of electrons is given by $-N(E_F)\Delta_0^2/2$, where $N(E_F)$ is the density of states (DOS) at the Fermi energy.

The elementary excitation of a superconductor is the breaking of a Cooper-pair which results in two independent quasiparticles in S. The lowest possible energy of

[1] $\Delta_0/E_F = 10^{-3}$

an unpaired electron in S (also called quasiparticle) is given by the energy gap Δ_0. The minimum energy necessary for an excitation is therefore $2\Delta_0$. This results in an energy gap of size $\pm\Delta_0$ around E_F in the DOS of the quasiparticles. The opening of this gap suppresses scattering processes which are responsible for the electrical resistance and can be used to explain the resistance drop in superconductors at T_C.

For finite temperatures, some Cooper-pairs are broken into quasiparticles due to thermal fluctuations. The quasi particles are Fermions and obey the Fermi distribution. For increasing temperature, the number of Cooper-pairs and the size of the energy gap Δ_0 decreases; for $T \to T_C$, the energy gap Δ_0 goes to 0.

The BCS theory described so far is practical to describe homogenous superconductors where k is a good quantum number. For dirty superconductors, as well as inhomogeneous systems, where $\Delta(r)$ varies spatially, it is more appropriate to use a description in real space rather than in k-space. The Bogoliubov equation is a very useful tool to investigate inhomogeneous systems like S/N heterostructures.

In real space, the electron- or hole-like quasiparticles, represented by the components of the vector $(u(r), v(r))$, obey the Bogoliubov equation [10, 11]:

$$\begin{pmatrix} H(r) & \Delta(r) \\ \Delta^*(r) & -H(r) \end{pmatrix} \begin{pmatrix} u(r) \\ v(r) \end{pmatrix} = E \begin{pmatrix} u(r) \\ v(r) \end{pmatrix} \tag{2.5}$$

with the one electron Hamiltonian

$$H(r) = \frac{1}{2m^*} \left(-i\hbar\nabla - eA(r)\right)^2 + U(r) - E_F \tag{2.6}$$

where m^* the effective electron mass, $A(r)$ is a vector potential, $U(r)$ is a scalar potential and $\Delta(r)$ is the spatially varying pair potential, which couples the electron-like and hole-like states [10].

In the dirty limit, with a large number of scattering centers, the Usadel equations have proven to be an useful tool to describe inhomogeneous superconductivity [10, 12]. They are a simplification of the Eilenberger equation, which is valid if the mean free path is much smaller than the coherence length [13].

The pair amplitude F(x), which will appear in the subsequent sections when discussing the *proximity effect*, is related to the density of Cooper-pairs n_S. Inside a superconductor n_s is proportional to Δ_0^2.

2.2 Proximity Effect

A superconductor in good electrical contact to a normal metal (N) modifies the local DOS and transport properties in the normal material. Limited to a certain distance from the interface, the coherence length ξ_N, the pair amplitude of the superconductor penetrates into the normal metal. By doing so, the normal metal can gain some superconducting properties (an induced pair amplitude), without possessing a pair potential itself. This fact can be exploited to drive a supercurrent across a S/F/S hybrid structure with sufficiently small thickness of the F layer, where typically the exchange energy E_{ex} in F is much larger than Δ. This so called proximity effect requires highly transparent interfaces and has been observed e.g. in Nb/Au bilayers by using a very low temperature scanning tunnel microscope [14]. The proximity effect can be visualized as a diffusion of Cooper-pairs from the superconductor into the normal metal.

On the other hand, the normal metal also influences the superconductor: The diffusion of normal electrons into the superconductor, the *inverse proximity effect*, suppresses the superconducting pair amplitude in S near the interface (see Figure 2.2, dashed line).

The microscopic mechanism to provide the extension of the superconducting properties into the normal metal is the Andreev-reflection (see Figure 2.3). It provides the phase coherent conversion from single electrons in N into Cooper-pairs in S. Here only the one dimensional case is considered. An incoming electron from the normal metal side with energy lower than the superconducting gap can not be directly transferred into the superconductor due to the energy gap in the quasiparticle spectrum. But by involving a second electron of opposite spin and momentum, the electron can enter into the superconductor as a Cooper-pair, while a hole is left behind in the normal metal. From the N side, it looks like the incoming electron has been reflected as hole; from the S side, a Cooper-pair has entered. The reflected hole carries information of the phases of the incoming electron as well as of the superconducting condensate in S. The Andreev-reflection is a phase coherent process. For a review on the topics Andreev-reflection and proximity effect see [15].

In the following section 2.2.1, the proximity effect is illustrated for the case of a superconductor/normal metal bilayer. In section 2.2.2, superconductor/ferromagnet proximity systems are discussed.

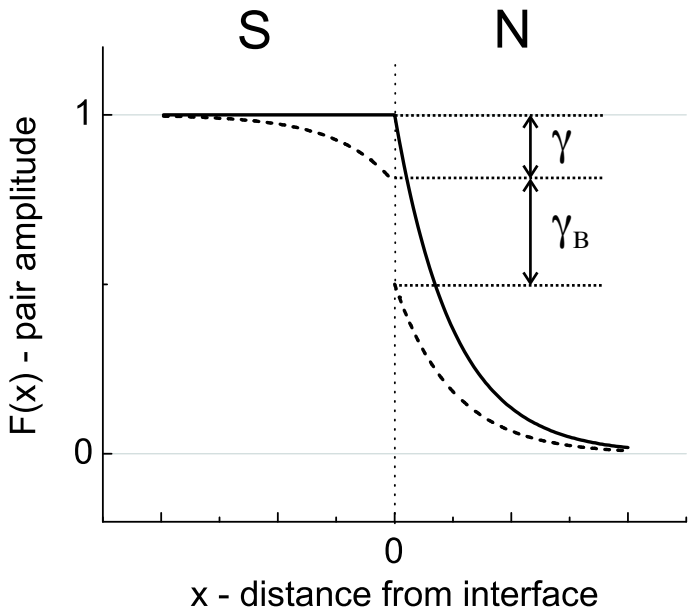

Figure 2.2: Proximity effect: The superconducting pair amplitude extends into the normal metal (N) close to a highly transparent interface thereby transferring the superconducting properties to this region (solid line, simplified picture). The length-scale of the exponential decay in N is given by the normal metal coherence length ξ_N. The dashed line gives a more realistic picture of the pair amplitude close to the interface: The proximity of the normal metal decreases the pair amplitude on the superconducting side (*inverse proximity effect*). Furthermore a jump which is proportional to the interface resistance occurs at the interface of the two metals [10, 13]. The values γ and γ_B are defined in section 2.2.1.

2.2.1 Normal Metal/Superconductor

As mentioned above, the superconducting properties are transferred to the normal metal via Andreev-reflection. This mechanism provides a possibility of phase coherent charge transfer from the paired electrons in S to a pair of quasiparticles in N.

On the N side, this process involves an electron at energy $E_F+\epsilon$ and a hole at energy $E_F-\epsilon$, which have wavevectors $k_e = k_F + \delta_k$ and $k_h = k_F - \delta_k$, where $\delta_k = \epsilon/\hbar v_F$ (see Figure 2.4), v_F is the Fermi velocity. Here a linear E-k dependence close to the Fermi energy is approximated.

Immediately after the Andreev-reflection, this electron-hole pair is phase coherent. However, due to the difference of the wave vectors

$$2\delta_k = k_e - k_h \tag{2.7}$$

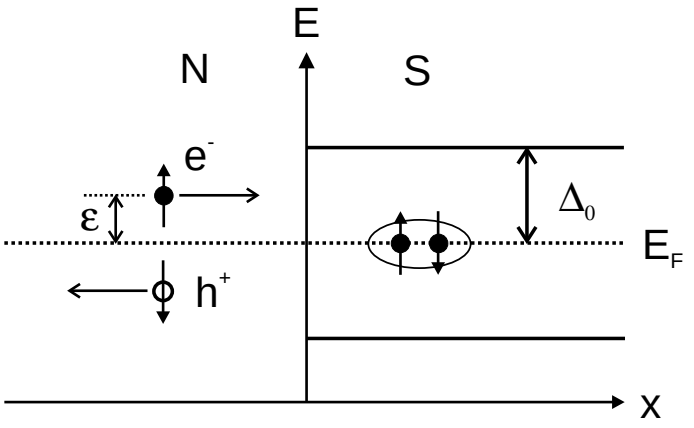

Figure 2.3: Schematic description of the Andreev-reflection at a SN interface in real space: An incoming electron with energy $\epsilon < \Delta_0$ from the normal metal can only enter the superconductor by involving a second electron of opposite spin and momentum, to form a Cooper-pair in S and leave behind a hole in N. From the superconductor's point of view, a Cooper-pair enters, from the normal metal side an electron is Andreev-reflected as a hole.

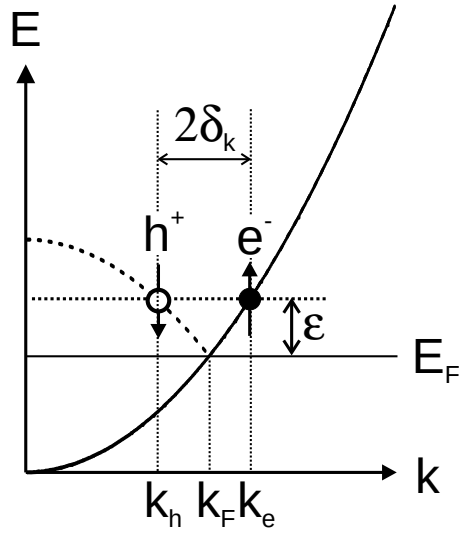

Figure 2.4: Andreev-reflection in k-space: An incoming electron with energy ϵ smaller than the superconducting energy gap and k-vector $k_e = k_F + \delta_k$ is Andreev-reflected as a hole with k-vector $k_h = k_F - \delta_k$. The difference of the k-vectors of the electron and the reflected hole is $2\delta_k$.

the orbits of the correlated pair are in general[2] not completely identical, which leads to a dephasing of the electron-hole pair within the normal metal. The phase difference $\Delta\varphi$ picked up by the electron-hole pair in N is proportional to the traveled distance from the interface l, and on the difference of the wave vectors δ_k:

$$\Delta\varphi = 2\delta_k l. \tag{2.8}$$

As can be seen from equation 2.8, with increasing distance from the interface, the phase difference of the Andreev reflected electron-hole pair increases. If the phase difference becomes larger than π, the phase correlation between electron and hole is finally lost.

The thermal coherence length ξ_N sets the length-scale of the proximity effect, that is the average length, on which the Andreev reflected electron-hole pairs maintain their phase correlation in the normal metal

$$\xi_N^{clean} = \frac{\hbar v_F}{2\pi k_B T}. \tag{2.9}$$

.

In the clean limit (the elastic mean-free-path of the electrons is larger than ξ_N) it is determined by the Fermi velocity v_F and temperature T as shown by equation 2.9, k_B is Boltzmann's constant. If the mean free path is smaller than ξ_N (diffusive case), the coherence length is given by

$$\xi_N^{diff} = \sqrt{\frac{\hbar D}{2\pi k_B T}}, \tag{2.10}$$

where D is the diffusion constant.

Figure 2.2 shows the spatial dependence of the superconducting pair amplitude, which is a measure for the Cooper pair density, close to a S/N interface with high transparency. Characteristic for the normal side is the exponential decay of the pair amplitude:

$$F_N(x) \sim F_N(0)\exp(-x/\xi_N). \tag{2.11}$$

While in the simplest approximation of the proximity effect (solid line) $F(x)$ is assumed constant within the superconductor, the dashed line in figure 2.2 gives a more realistic picture of the induced pair amplitude. Thereby the parameter

$$\gamma = \rho_S\xi_S/\rho_N\xi_N \tag{2.12}$$

[2] $\delta_k = 0$ only for an incoming electron exactly at the Fermi energy

describes the suppression of the pair amplitude close to the interface on the S side, due to the inverse proximity effect. ξ_S is the coherence length in the superconductor, ρ_S and ρ_N are the specific normal state resistances of the superconductor and the normal metal, respectively. The height of the jump of the pair amplitude at the interface of the two metals is given by

$$\gamma_B = R_B/\rho_N \; xi_N \tag{2.13}$$

which depends on the interface resistance R_B [10, 13].

2.2.2 Ferromagnet/Superconductor

In the following section the proximity effect between a superconductor and a ferromagnetic metal is discussed. For further details see e.g. [16, 17].

The decoherence between an Andreev reflected electron-hole pair in a normal metal is influenced by the energy ϵ (counted from E_F) of the electron and the reflected hole. In the proximity effect between a superconductor and a ferromagnet, the exchange energy has a predominant effect on the thermal coherence length. If the exchange energy is large compared to the temperature $E_{Ex} > k_B T$ the coherence length is much shorter than in the case of the superconductor/normal metal proximity effect. Because the ferromagnetic metal layers which define the SFS Josephson junctions have a thickness of the order of the coherence length, this imposes experimental difficulties when it comes to the growth of homogenous layers of only several Å thickness.

However, by using diluted ferromagnetic metals with relatively small exchange energies, the induced superconductivity can survive ferromagnetic layer thicknesses of some nm and thereby reach an order of magnitude which can be accessed experimentally without applying epitaxy. The weak ferromagnet used in this experiment is $Pd_{0.82}Ni_{0.18}$ with an exchange energy of the order of 50 meV and a ξ_F of 2.3 nm [18] (the magnetic properties of this material are discussed in section 3.4).

In a ferromagnet in proximity to a superconductor, the coherence length ξ_F is a complex quantity due to the presence of an exchange field. In the diffusive limit it is given by

$$\xi_F = \sqrt{\frac{\hbar D}{2\left(\pi k_B T + i E_{Ex}\right)}}. \tag{2.14}$$

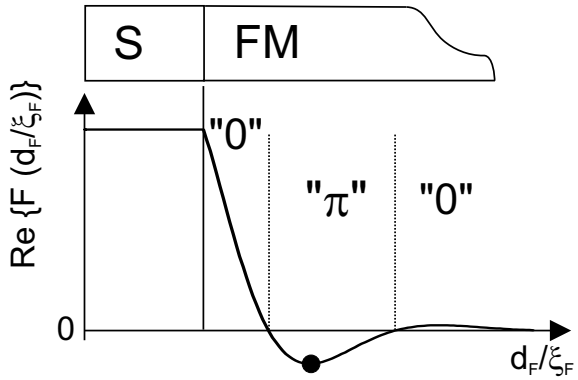

Figure 2.5: Proximity effect between a superconductor and a ferromagnetic metal. Characteristic for the presence of an exchange field in the proximity superconductor is the oscillation of the induced pair amplitude which is superimposed on the exponential decay in F [17]. This oscillation includes a change of sign and can be exploited to realize negative coupling between two superconductors and to fabricate π-junctions (indicated by the black dot). The inverse proximity effect in S is not shown in this simplified picture.

In addition to the reduced coherence length compared to typical SN structures, a second characteristic property arises from the complex nature of the coherence length: The induced pair amplitude oscillates spatially in the ferromagnetic metal as a consequence of the exchange field acting upon the spins of the two electrons forming a Cooper-pair (see Figure 2.5). This oscillation includes a change of sign and by using appropriate values for the exchange energy and layer thickness, negative coupling can be realized. This effect can be exploited in order to fabricate ferromagnetic π-junctions. Further details on this topic will be given in section 2.3.3.

The mechanism leading to the oscillation of the pair amplitude in F can be explained as follows: The Andreev reflected electron and hole in F have opposite spin and therefore the energies of the electron and the hole are shifted by the Zeeman energy in the ferromagnet. To compensate this energy shift and to conserve their total energy, the k vectors of the electron and the hole are shifted by Q (Figure 2.6). As initially the electron and the hole had k-vectors in opposite directions and equal magnitude, this leads to a nonzero center of mass momentum of $2Q$ of the electron-hole pair

$$2Q = k_\uparrow - k_\downarrow = \frac{2E_{Ex}}{\hbar v_F}. \tag{2.15}$$

The Cooper-pair wave function contains an oscillating component due to the non zero center of mass momentum:

$$\Psi(x) \sim e^{-ik_\downarrow x} e^{ik_\uparrow x} \approx e^{i2Qx}. \tag{2.16}$$

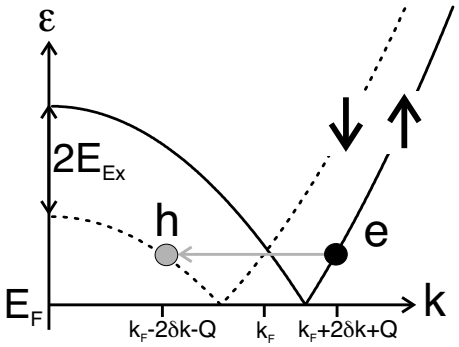

Figure 2.6: Andreev-reflection at an F/S interface: Because the incoming electron and the Andreev reflected hole occupy different spin bands in F, the difference of the k-vectors of the incoming electron and the Andreev reflected hole is strongly influenced by the exchange splitting E_x of the two spin directions in the ferromagnet.

As a result, the oscillating component gives rise to an oscillating pair amplitude

$$F(x) = \langle \Psi_\uparrow(x)\Psi_\downarrow(x)\rangle. \tag{2.17}$$

The real part of ξ_F determines the exponential decay of the induced pair amplitude

$$\Re(\xi_F^{diffusive}) = \xi_{F1}^{diffusive} = \sqrt{\frac{\hbar D}{\sqrt{E_{Ex}^2 + (\pi k_B T)^2} + k_B T}}, \tag{2.18}$$

while the oscillation of the induced order parameter is characterized by the imaginary part

$$\Im(\xi_F^{diffusive}) = \xi_{F2}^{diffusive} = \sqrt{\frac{\hbar D}{\sqrt{E_{Ex}^2 + (\pi k_B T)^2} - k_B T}}. \tag{2.19}$$

If E_{Ex} is much larger than k_BT (or for $T = 0$ and arbitrary E_{Ex}), ξ_{F1}^{diff} and ξ_{F2}^{diff} are equal, which means that the oscillation period and the decay length are identical [13, 19, 20]. In the clean limit, ξ_{F1}^{clean} is infinite for $T = 0$ and the decay length is only limited by elastic impurity scattering or spin-orbit scattering [13, 21, 16] and is usually larger than the oscillation period ξ_{F2}^{clean}. It is therefore easier to observe the spatial oscillation of the order parameter in clean systems [13].

Table 2.1 summarizes some important length- and energy-scales of a ferromagnet in proximity to a superconductor in the clean and dirty limit. For a detailed theoretical discussion of the oscillatory effects in S/F sandwiches see [16, 17].

Diffusive Limit	Clean Limit
$\xi_F = \sqrt{\frac{\hbar D}{E_{ex}}}$	$\xi_F = \frac{\hbar v_F}{3E_{ex}}$
$d_F = \sqrt{\frac{\hbar D}{E_{Th}}}$	$d_F = \frac{\hbar v_F}{E_{Th}}$
$E_{Th} = \frac{\hbar D}{d_F^2}$	$E_{Th} = \frac{\hbar v_F}{d_F}$
$E_{ex} = \frac{\hbar D}{\xi_F^2}$	$E_{Ex} = \frac{\hbar v_F}{3\xi_F}$

Table 2.1: Some important length and energy scales for S/F heterostructures. ξ_F is the coherence length in F, d_F the thickness for the crossover point between positive and negative coupling, E_{Th} the Thouless energy and E_{Ex} the exchange energy ($E_{Ex} \gg k_B T$).

2.3 The dc-Josephson Effect

In 1962 it was predicted by Josephson that a supercurrent can flow across a weak link between two superconducting electrodes [22]. The Josephson effect was initially described for a thin insulating barrier between two superconductors. Actually, it is a more general effect and exists for a variety of weak links embedded between two superconductors. Besides the classical SIS junctions, these weak links can consist of nonmagnetic normal metals (SNS), constrictions (ScS), ferromagnetic metals (SFS) or two dimensional electron gases (S-2DEG-S). A review of the various types of weak links and the corresponding current phase relations (CPRs) is given in [13]. Some types of weak links (SIS, SNS and SFS) are discussed in the following sections.

2.3.1 Supercurrent across an Insulating Barrier

The dependence of the supercurrent flowing across a Josephson junction as a function of the phase difference is described by the current phase relation (CPR), which is an important characteristic of a Josephson junction. In the case of a tunneling barrier, realized e.g. by a thin insulating layer, it is given by

$$I_S = I_C \sin \varphi, \tag{2.20}$$

which is plotted in Figure 2.7. As can be seen by Eqn. 2.20, the supercurrent I_S across the weak link is driven by the phase difference $\varphi = \Phi_1 - \Phi_2$ of the supercon-

ducting wave functions on both sides of the weak link. The critical current I_C is the maximum supercurrent that can be sustained by the weak link.

The CPR can deviate considerably from the basic sinusoidal shape expected for a tunnel barrier (shown in Figure 2.7) and can be generally expressed by

$$I_S = \sum_n I_n \sin n\varphi + J_n \cos n\varphi, \tag{2.21}$$

where the coefficients J_n vanish if the time reversal symmetry is not broken. A review of the various types of possible CPRs is given by Golubov in [13].

2.3.2 Supercurrent across a Normal Metal

Due to the proximity effect (see sections 2.2.1 and 2.2.2), supercurrent can also flow across a weak link consisting of a normal metal or a ferromagnetic metal. In the following section, the focus will be on the one dimensional case in the clean limit [23]. The supercurrent across a SNS junction is carried by Andreev bound states (ABS), which can be viewed as standing waves of Andreev reflected electron-hole pairs in the potential well defined by the pairing potential of the two superconducting electrodes on either side of the weak link. The spectrum of the ABS in the clean limit is a sequence of δ-peaks. In the presence of disorder, the energies corresponding to the Andreev bound states are broadened, leading to a continuous spectral supercurrent density.

An ABS at energy ϵ_n is formed if the global phase difference φ between the superconductors is equal to the phase $\Delta\varphi$ picked up by the electron-hole pair in N plus an additional term due to the fact that the quasi particles penetrate a small but finite distance into the superconducting electrodes S.

For a clean normal metal between two superconducting electrodes an Andreev bound state with energy $\epsilon_n < \Delta$ is formed if the condition

$$\Delta\varphi = 2\frac{\epsilon_n}{\hbar v_F} d = \mp\varphi + 2\arccos\frac{\epsilon_n}{\Delta} + 2\pi n, \tag{2.22}$$

is fulfilled (d is the length of the normal metal). Each of the Andreev bound states can carry supercurrent whose direction is given by the sign in front of φ. In equation 2.22 the arccos-term takes into account the phase picked up by the pair during the process of Andreev reflection in the superconducting reservoirs. As the spectrum of the ABS depends on the phase difference φ, the supercurrent is phase dependent.

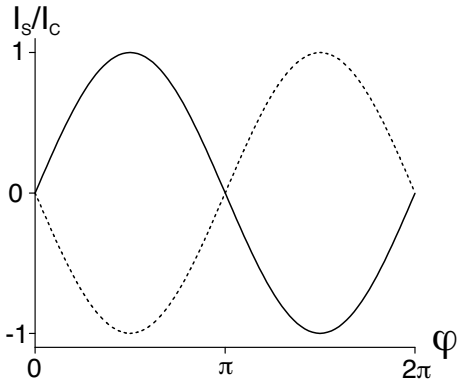

Figure 2.7: The solid line shows the sinusoidal current phase relation expected for a SIS Josephson junction. The dotted line shows the inverted CPR of a ferromagnetic Josephson junction, which is a consequence of the negative sign of the supercurrent (a sinusoidal CPR is assumed). Josephson junctions with such an inverted CPR are called π-junctions, because they are characterized by an intrinsic phase shift of π when compared to the SIS case.

For $\varphi = 0$ the level spacing is given by πE_{Th} (see table 2.1) [24]. It can be seen in equation 2.22 that for $\varphi = 0$ the ABS for opposite current directions are energetically degenerate, so they compensate each other, thus leading to zero total supercurrent.

For $\varphi \neq 0$ the degeneracy is lifted. Because the ABS are occupied according to a thermal distribution function, the energetically lower lying levels are more populated than the higher ones, even at $T = 0$. This results in a non-zero net supercurrent for finite phase differences, the direction of which is determined by the lowest lying level.

The CPR can be obtained from the ABS spectrum by integrating over all occupied ABS (Eqn. 2.25). A comprehensive experimental investigation of CPRs of SNS Josephson junctions was done by Bentner [25].

2.3.3 Supercurrent across a Ferromagnetic Weak Link: How to Fabricate π-Junctions

Due to the spatially oscillating induced pair amplitude in SF proximity structures (see section 2.2.2) it is possible to realize negative coupling of two superconductors across a ferromagnetic weak link. In this case of negative coupling, the critical current across the junction is reversed when compared to the normal case giving rise to an inverted CPR (see Figure 2.7). Because they are characterized by an intrinsic phase shift of π these junctions are called π-junctions.

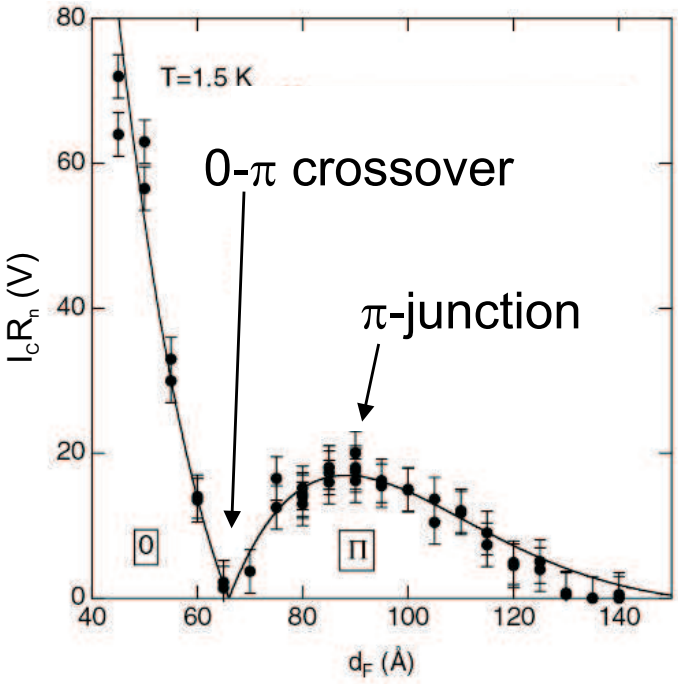

Figure 2.8: Dependence of the $I_C R_N$ product of a SIFS Josephson junction on the F layer thickness d_F [5]. The diluted ferromagnet used in this experiment is $Pd_{0.88}Ni_{0.12}$, the temperature is 1.5 K. The zero at $d_F = 65$ Å and the reoccurrence for larger layer thicknesses indicates the crossover from zero- to π-coupling. The d_F corresponding to the two types of ferromagnetic Josephson junctions investigated in this work are indicated by the arrows.

The dependence of the $R_N I_C$ product on the thickness of the ferromagnetic layer in SIFS junctions has been experimentally investigated by Kontos et al. (see Figure 2.8, [5]).

In the case of ferromagnetic weak links, Eqn. 2.22 which gives the energies of the Andreev bound states ϵ_n, has to be completed by E_{Ex} to account for the additional phase shift the electron-hole pairs acquire due to the presence of the exchange field in the ferromagnet:

$$\Delta\varphi = 2\frac{\epsilon_n \pm E_{Ex}}{\hbar v_F} d = \pm\varphi + 2\arccos\frac{\epsilon_n}{\Delta} + 2\pi n. \tag{2.23}$$

The additional term in equation 2.23 shifts the spectral positions ϵ_n of the ABS. The sign in front of E_{Ex} corresponds to the two possible spin configurations $\uparrow\downarrow$ or $\downarrow\uparrow$ for the electron-hole pair. For $\varphi = 0$ the levels which carry current in opposite directions are again energetically degenerate and compensate each other, so the net current is still zero. For non-zero phase differences however, the degeneracy is lifted and it is possible, depending on E_{Ex} and d, that the lowest lying level, which is the most

populated one[3], now carries a negative supercurrent, i.e. in the opposite direction when compared to the normal metal case. This means that the supercurrent for these special types of ferromagnetic junctions has changed its sign. The negative sign of the supercurrent results in an inverted CPR

$$I_S^{\pi} = -I_C \sin\varphi = I_C \sin(\varphi + \pi), \tag{2.24}$$

where a sinusoidal CPR is assumed.

Figure 2.7 compares the CPRs of a standard (SIS) Josephson junction with a π-junction (according to Eqn. 2.24). The CPR of the π-junction can be obtained from the standard CPR by a phase shift of π. A π-junction can therefore be considered as a Josephson junction with a built-in phase difference of $\varphi = \pi$.

As in the normal metal case, in the diffusive regime, the sharp δ-peaks corresponding to the ballistic ABS are broadened and evolve towards a continuous spectral supercurrent density $N_J(\epsilon)$. The total supercurrent I_S is obtained by integrating over the spectral contribution weighted with the thermal occupation of the ABS

$$I_S(T) = \frac{1}{eR_N} \int_0^{+\infty} N_J(\epsilon) \tanh(\epsilon/2k_BT) d\epsilon. \tag{2.25}$$

By varying the temperature, the spectral contribution to the total supercurrent can be weighted. By employing this mechanism, even a temperature dependent crossover from 0 to π-junctions can be observed [26, 24]. The condition for utilizing the temperature as a parameter to tune the junction from 0- to π-coupling is

$$k_BT \approx E_{Ex}. \tag{2.26}$$

Another way to look at the temperature induced crossover from the 0 to the π state in diffusive samples can be found in Eqn. 2.19 [26]. The crossover (0 to π) of a junction with given layer thickness can be attributed to the temperature dependence of ξ_F, which sets the length-scale of the oscillation of the induced pair amplitude (see Figure 2.5).

In our samples the diluted ferromagnet $Pd_{0.82}Ni_{0.18}$ is employed, the corresponding exchange energy is estimated to be of the order of 52 meV. This value corresponds to a temperature of more than 600 K. The condition to have T as an parameter (Eqn. 2.26) is obviously not fulfilled and therefore it is reasonable to assume for

[3] and determines the direction of the supercurrent

this experiment that the temperature has no influence on the 0- or π-character of the ferromagnetic Josephson junction.

In general, the CPR relation for a π-junction is predicted to deviate from the simple sinusoidal shape. The CPR for point contacts (SFcFS) and double barrier junctions (SIFIS) for thin diffusive ferromagnetic interlayers was theoretically investigated by Golubov [27].

Experimentally, the exact shape of a CPR is difficult to measure. Bentner has developed a method to directly measure the CPR of mesoscopic SNS junctions [25]. To do so, the junctions are incorporated into contacted superconducting loops and placed on a micro-Hall sensor. The method can be applied for values of the LI_C products smaller than $0.4 \times \Phi_0$ (see section 2.4.2). I_C is the critical current of the junction, L is the inductance of the loop and Φ_0 the flux quantum.

It has been predicted, that ferromagnetic Josephson junctions close to the transition point between 0 and π show a CPR with dominating 2φ-periodic contribution [28, 29]. Sellier has given an illustrative explanation for the expected 2φ periodicity for ballistic junctions[24, 23]. For certain values of the exchange field, the level spacing of the ABS is half of the spacing without exchange field. The reason for this change is the lifted degeneracy of the pairs of ABS with reversed spin configurations. Frolov et al. investigated the CPR of $Nb/Cu_{0.47}Ni_{0.53}/Nb$ junctions which show a temperature induced crossover between the 0- and the π-state. They found a vanishing critical current at the crossover point, and no higher harmonics in the CPR [30]. Sellier et al. investigated the CPR of $Nb/CuNi/Nb$ junctions by applying a high frequency excitation to the junction and observing the formation of Shapiro steps [23]. They found half-integer Shapiro steps at the crossover temperature which are attributed to the $\sin 2\varphi$ dependence of the corresponding CPR.

Besides the ferromagnetic π-junctions described above, there are other ways to prepare π-junctions. By contacting the normal layer of a SNS junction and driving a current through it, controllable $0/\pi$-junctions can be realized. Depending on the control current through the normal part of the junction, the energy distribution of the quasiparticles in N is modified and thereby the weighting of the spectral supercurrent density is modified, giving rise to either 0- or π-junction behavior [31, 4]. In high T_C superconductors with d-wave symmetry of the order parameter, grain boundaries are used to create Josephson junctions with negative coupling. The physical mechanism leading to π-junctions in this case is the direction dependence of the order parameter in HTC superconductors [3].

Backhaus et al. found a superfluid analogue to a superconducting π-junction [32]. They observed a metastable superfluid state, where a phase difference of π is main-

tained between two weakly coupled macroscopic quantum states which are formed by reservoirs of superfluid ^{3}He.

2.4 Flux Quantization

If a Josephson junction is integrated into a superconducting loop, the phase difference of the junction can be adjusted by applying a magnetic flux through the loop. This mechanism to control the phase is applied during the measurements of this work. A detailed description can be found in the textbook of Barone and Paterno, chapter 12 [33].

In the section 2.4.1, a plain superconducting loop is discussed. In the following two sections, a superconducting loop with integrated 0- and π-Josephson junction is considered. Finally an interesting consequence of the *half integer* flux quantization in superconducting loops with integrated π-junction (π-loops), the spontaneous supercurrent, is presented in section 2.4.3

2.4.1 Flux Quantization in a Superconducting Loop

In a superconductor, all the Cooper-pairs are described by the same wavefunction $\Psi = \Psi_0 e^{i\varphi}$ (see section 2.1). The uniqueness of the Cooper-pair wavefunction requires that the integral of the phase difference $\Delta\varphi$ once around in a closed loop may only take on values equal to integer multiples of 2π:

$$2\pi n = \oint \mathbf{\Delta}\varphi \mathbf{dl} = \frac{2\pi}{\Phi_0}\left\{\oint \mathbf{A}dl + \oint \frac{m^*}{2e^{*2}|\Psi_0|^2}\mathbf{j}_S dl\right\} = 2\pi\frac{\Phi}{\Phi_0} \tag{2.27}$$

$$\Phi_0 = \frac{h}{2e} = 2.07 \times 10^{-15}\ \mathrm{T\ m^2} \tag{2.28}$$

where n is an integer, $\mathbf{A}$ is the vector potential, m^* is twice the electron mass, e^* is twice the electron charge, $\mathbf{j}_S$ is the supercurrent density, Φ is the total flux through the loop and Φ_0 the flux quantum.

In a superconducting loop, if the dimensions of the superconducting lead are large compared to the London penetration depth, the magnetic field deep inside the leads which form the superconducting loop can be assumed zero. Therefore an integration path for formula 2.27 can be chosen, where only the vector potential $\mathbf{A}$ contributes to the phase picked up by the condensate, but not the current density $\mathbf{j}_S$.

The result of this integration is, that due to the uniqueness of the phase of the condensate, the magnetic flux Φ penetrating a superconducting loop is quantized in units of the flux quantum Φ_0 [33].

If an arbitrary external field is applied to a superconducting loop, in general a circulating supercurrent I will start to flow in the loop. The applied magnetic field and the field generated by the circulating current will sum up to fulfill the condition of flux quantization in the loop

$$\Phi = \Phi_{applied} + LI = n\Phi_0. \tag{2.29}$$

2.4.2 Superconducting Loop with Integrated Josephson-Junction

If a Josephson junction is included into the superconducting loop considered in the preceding section, the integration of the phase difference once around the loop leads to

$$2\pi n = \varphi_J - \frac{2\pi}{\Phi_0} \int_{\gamma_1} \mathbf{A} dl \tag{2.30}$$

where φ_J is the phase difference across the weak link; the integration path from P_1 to P_2 is chosen along the loop except the part containing the Josephson junction. The points P_1 and P_2 shall be the boundaries of the Josephson junction (see Figure 2.9).

The missing part of the integral is completed to a closed loop by employing the gauge invariant expression for the phase difference across the junction

$$\varphi_J^* = \varphi_J - \frac{2\pi}{\Phi_0} \int_{\gamma_2} \mathbf{A} dl \tag{2.31}$$

where the *short* integration path γ_2 from P_1 to P_2, just across the junction, is used (see Figure 2.9).

By subtracting equations 2.30 and 2.31 the condition of flux quantization for a superconducting loop with integrated Josephson junction is obtained:

$$2\pi n = \varphi_J^* + 2\pi \frac{\Phi}{\Phi_0}. \tag{2.32}$$

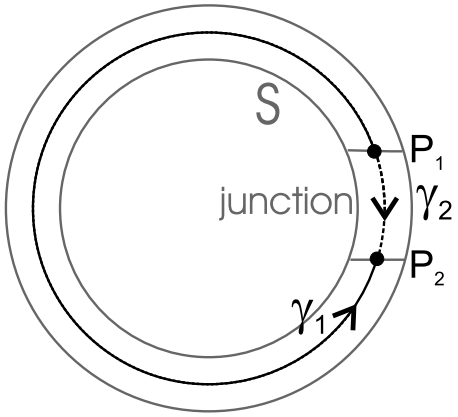

Figure 2.9: Diagram to illustrate the integration paths used in equations 2.30 and 2.31. S denotes the superconducting loop, the boundaries of the Josephson junction are indicated by P_1 and P_2.

Together with the CPR, which is assumed to be sinusoidal for simplicity and the fact that the total flux through the loop is the sum of the applied flux and the flux produced by the loop, this leads to a system of two coupled equations for Φ and I_S:

$$\Phi_{app.} = \Phi + \frac{1}{2\pi k}\Phi_0 \sin\left(2\pi\frac{\Phi}{\Phi_0}\right) \tag{2.33}$$

$$I_S = -I_C \sin\left(2\pi\frac{\Phi_{app.}}{\Phi_0} + \frac{I_S}{kI_C}\right). \tag{2.34}$$

Equations 2.33 and 2.34 describe the dependence of the total flux Φ and the circulating current I_S on the applied flux $\Phi_{applied}$ [33, 34]. Two different types of solutions of Eqns. 2.33 and 2.34 can be determined, depending on the value of the important parameter k:

$$k = \frac{\Phi_0}{2\pi L I_C}, \tag{2.35}$$

where L is the inductance of the loop. Note that k is temperature dependent, because I_C varies with T. For $k > 1$, the dependence of Φ and I_S on $\Phi_{applied}$ is single valued and can be solved analytically. For $k < 1$, the curves are multi-valued and only the parts with positive slope are traced. In this case, the continuous trend of Φ and I_S as a function of Φ_{app} is interrupted by sudden jumps and the magnetization traces of such loops are hysteretic. The jump height depends on k and the shape of the CPR and is in general smaller than Φ_0 ($0.75 \times \Phi_0$ for a value of k corresponding to our 0-loop at 1 K assuming a sinusoidal CPR).

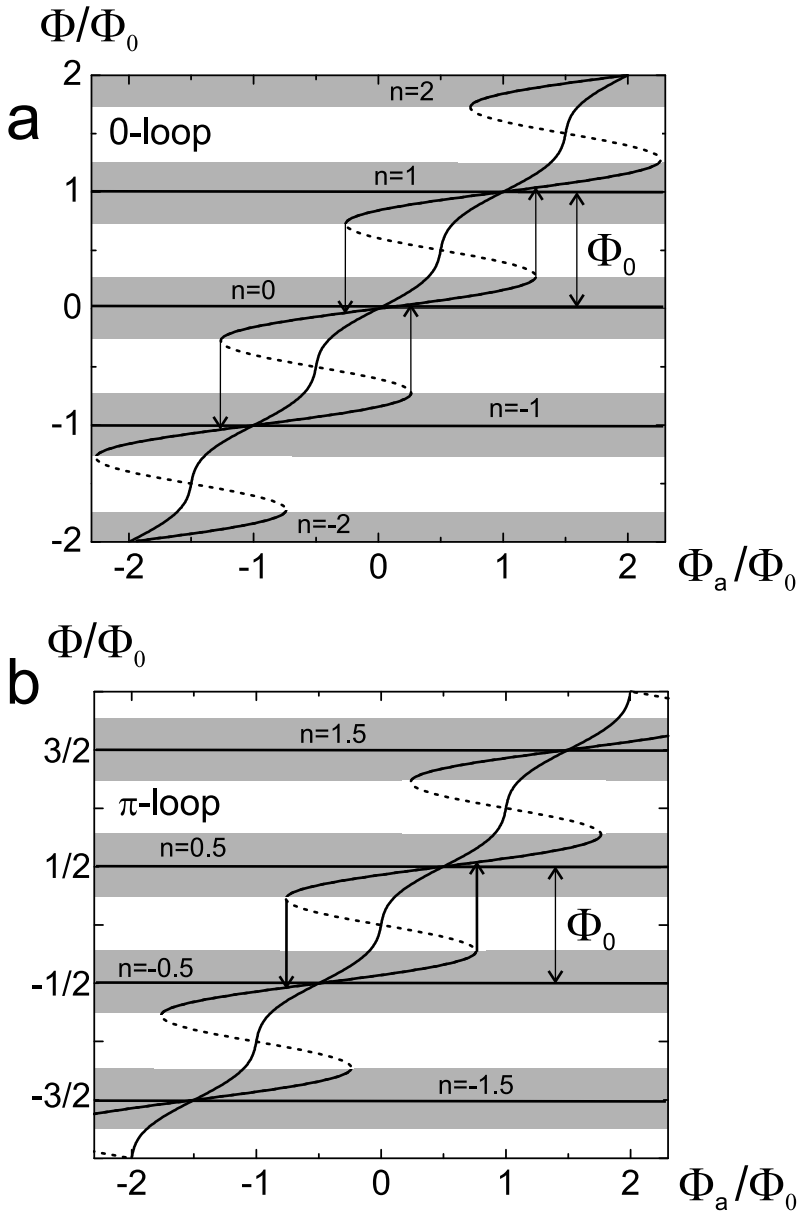

Figure 2.10: The total flux as a function of the applied flux (flux plot) for two values of the parameter k ($k = 1.2$ and $k = 0.16$). For $k = 1.2$ the flux relation is single valued for all values of the applied flux. For $k = 0.16$ the relation is multi valued and only parts of the curve with positive slope are traced (solid line), which leads to hysteretic behavior. Panel (a) shows the 0-loop. Note that the flux is not strictly quantized due to the CPR of the incorporated Josephson junction. The shaded areas denote the stable states corresponding to the *softened* integer flux quantization, where n is an integer that counts the number of flux quanta in the loop. (b) Same plot for a π-loop, note that the flux is quantized at half integer values.

Typical curves are plotted in Figures 2.10(a) and 2.10(b) for two values of k and for 0- and π-loops. These graphs are referred to as flux-plots in the following and will be helpful in interpreting the measured magnetization curves in section 4.3. Note that the flux is not *strictly* quantized due to the CPR of the integrated Josephson junction (equation 2.34). In the following, the term *flux quantization* will nevertheless be used, even if the flux is not exactly quantized. The stable areas of the flux-plots are indicated by the gray shaded areas in Figures 2.10(a) and 2.10(b).

2.4.3 Superconducting Loop with Integrated π-Junction: Spontaneous Current

Figure 2.10(b) shows the solution of equations 2.33 and 2.34 for a superconducting loop with integrated π-junction for two values of the parameter k. When comparing the hysteretic flux-plot for the π-loop ($k = \frac{1}{2\pi}$) to the corresponding flux-plot of the 0-loop, it can be seen that for the π-loop the stable parts of the curve (gray shaded in Figure 2.10(b)) are found at half integer values of the total flux counted in units of Φ_0. This observation is called *half integer flux quantization* and is characteristic for a superconducting loop with integrated π-junction.

It was predicted by Bulaevskii in 1977 [1], that if a π-junction is inserted into a superconducting loop (and $LI_C > \frac{\Phi_0}{2\pi}$ or equivalent $k < 1$), the ground state for this system is a state with nonzero electric current and magnetic flux, see figure 2.11. This can also be seen in Figure 2.10(b): There is no stable part of the flux-plot with $\Phi = 0$ at $\Phi_{app} = 0$ for the π-loop. Therefore a spontaneous current has to flow in the loop at $\Phi_{app} = 0$.

Dependence of the Spontaneous Current on the LI_C Product

The value of the circulating current and the resulting magnetic flux produced by a π-loop in zero field depends on the parameter k, that is the product LI_C, where L is the inductance of the loop and I_C the critical current of the π-junction.

In the absence of applied fields equation 2.33 reduces to

$$\Phi = -LI_C \sin\left(2\pi \frac{\Phi}{\Phi_0}\right). \tag{2.36}$$

Assuming a CPR corresponding to a π-junction (equation 2.24) and together with expression 2.32 one finds that the solutions of

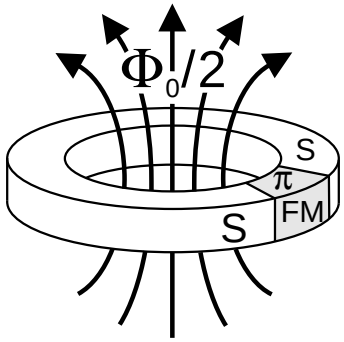

Figure 2.11: The single-valuedness of the phase of the superconducting wave function requires a spontaneous current to flow in a π-loop in the absence of external magnetic fields. This circulating current together with the loop inductance creates a spontaneous flux equal to half a flux quantum at low temperatures.

$$\sin\varphi - k\varphi = 0 \tag{2.37}$$

give the possible values of the phase differences φ across the Josephson junction, which can be sustained by the loop in zero applied field. But only the solutions of 2.37 for which the free energy has a local minimum correspond to stationary states [33].

The graphical solution for equation 2.37 is shown in Figure 2.12 for k=0.1 (panel a) and k=0.5 (panel b). The intersections of the sinusoidal curve at the bottom of each panel with the straight line denote the possible solutions of equation 2.37. The upper curve in each panel shows the corresponding free energy (see next section). Note that at $\varphi = 0$ the free energy of the π-loop has a maximum if $k < 1$. This means that at zero applied field there is no stable state with zero circulating current in the loop.

If $k > 1$, equation 2.37 has only the trivial solution $\varphi = 0$ corresponding to zero circulating current in the loop. This means that for a sinusoidal CPR, LI_C has to be larger than $\frac{\Phi_0}{2\pi}$ for the π-loop to develop a spontaneous current.

Free Energy of the Loop as a Function of I_S

The free energy of a superconducting loop with inserted Josephson junction as a function of the circulating current contains two terms: The magnetostatic energy connected to the magnetic field generated by the circulating current and the Josephson coupling-energy of the weak link.

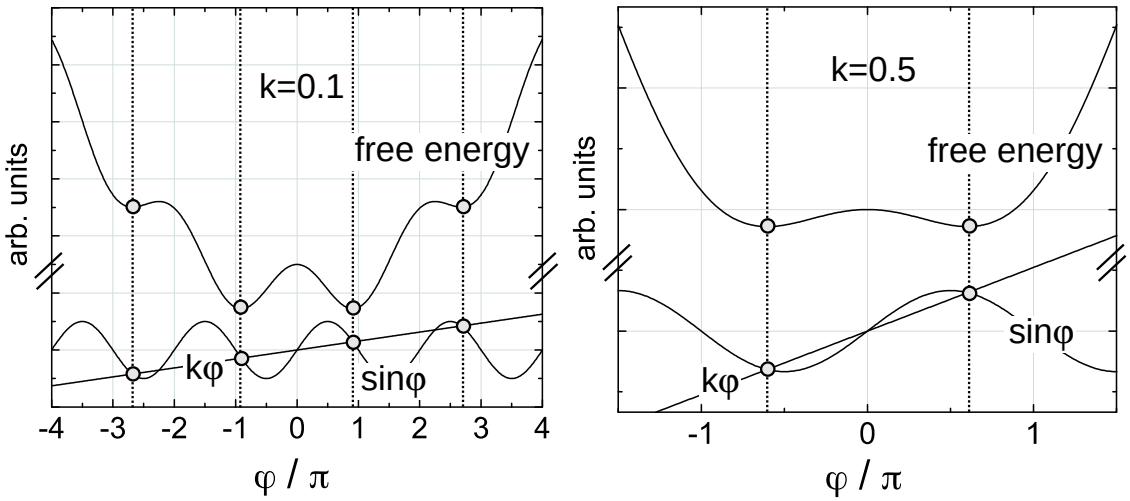

Figure 2.12: Illustration of the existence of a spontaneous supercurrent in a superconducting loop with integrated π-junction. Graphical solution of Equation 2.37 (lower curve) and the corresponding energy landscape (upper curve) for (a) k=0.1 and (b) k=0.5 in zero applied field. In both cases, only solutions with nonzero phase difference (marked with dots) are stable, as can be deduced from the minima in the free energy.

The free energy of the 0-loop is given by

$$E_0(I_S) = \frac{1}{2}LI_S^2 - \frac{\hbar I_C}{2e}\cos\left(2\pi\frac{LI_S}{\Phi_0}\right), \tag{2.38}$$

where the first term (proportional to I_S^2) is the magnetostatic energy and the second term is the Josephson coupling energy. When looking at the free energy of a 0-loop as a function of LI_S/Φ_0 (Figure 2.13(a)) in zero magnetic field, one finds that for all values of the critical current, the minimum of the free energy is located at zero circulating current in the 0-loop.

If a π-junction is inserted in a superconducting loop, the sign of the supercurrent changes as compared to a 0-junction (sinusoidal CPR); therefore also the Josephson coupling energy changes sign and equation 2.38 changes to

$$E_\pi(I_S) = \frac{1}{2}LI_S^2 + \frac{\hbar I_C}{2e}\cos\left(2\pi\frac{LI_S}{\Phi_0}\right). \tag{2.39}$$

The free energy of a π-loop as a function of LI_S/Φ_0 is plotted in Figure 2.13(b) in zero field.

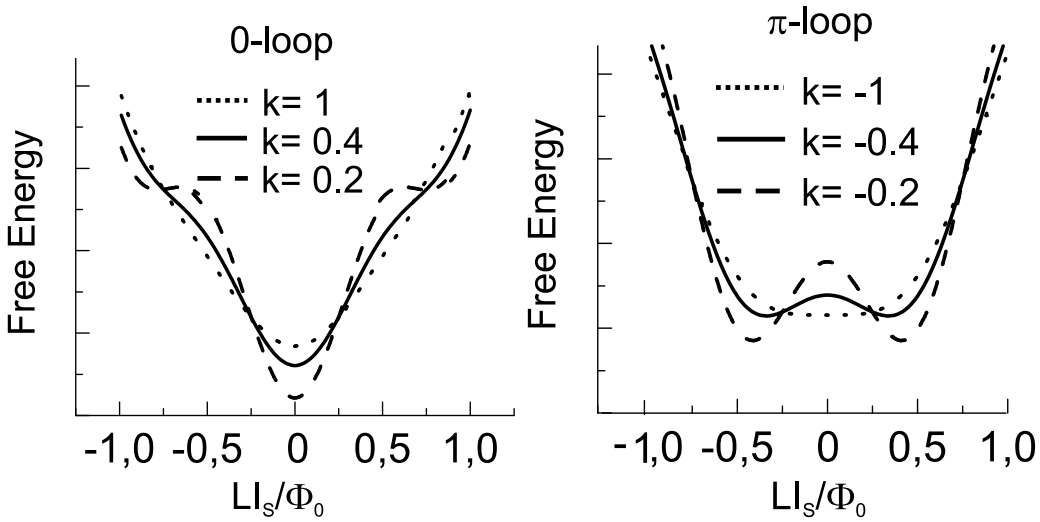

(a) (b)

Figure 2.13: The free energy of a 0-loop (a) and a π-loop (b) in zero applied field. The parameter k (equation 2.35) is determined by the LI_C product of the sample. The two components of the free energy are the magnetostatic energy of the circulating current (parabolic background) and the Josephson-energy (sinusoidal modulation). For $k < 1$ the ground state of the π-loop is characterized by a spontaneous current which produces magnetic flux that saturates close to half a flux quantum for $k \to 0$, as can be seen by the two minima which develop in panel (b) for small values of k. The corresponding energy plot for a zero loop (panel (a)), in contrary, shows one minimum at $LI_S = 0$ for all values of k.

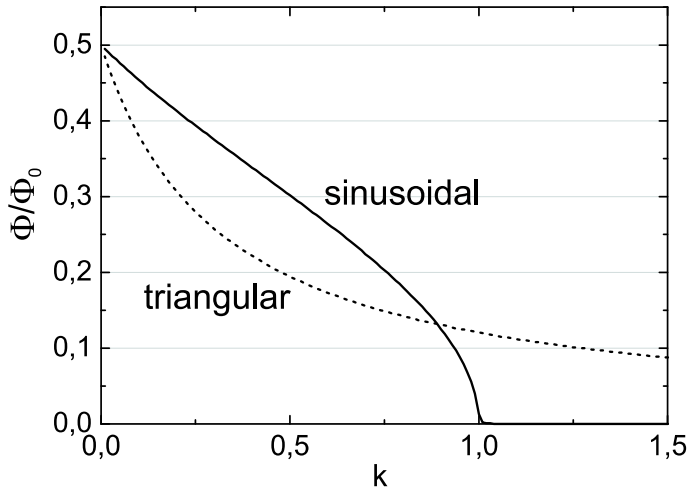

Figure 2.14: Normalized flux produced by a π-loop in zero field as a function of the parameter k (see equation 2.35). The solid line represents the result for a sinusoidal CPR, as shown in Figure 2.12, the dotted line the result for a triangular CPR. The flux shows a monotonic behavior as function of k. For a sinusoidal CPR the spontaneous flux is zero for $k > 1$. In both cases, the produced flux reaches half a flux quantum for $k \to 0$.

The important change compared to the energy landscape of a 0-loop plotted in Figure 2.13(a) is, that for sufficiently large values of the critical current, the energy minimum in zero field is no longer found at $I_S = 0$, that is at zero circulating current in the loop. Instead it is energetically more favorable for the π-loop to spontaneously start a circulating current, which produces a magnetic field equivalent to half a flux quantum at low temperatures, as illustrated in Figure 2.11.

Physically, the fact that the π-state exists only for $k < 1$ can be explained by comparing the two relevant energies for the loop, the magnetostatic energy and the Josephson coupling energy, which sum up in equation 2.39. For $k < 1$ the Josephson coupling energy becomes strong enough to overcompensate the magnetostatic energy, so an minimum of the free energy develops close to $LI_S = \Phi_0/2$.

Figure 2.14 shows the dependence of the normalized spontaneous magnetic flux on the parameter k (equation 2.35) for a sinusoidal and a triangular CPR. For a sinusoidal CPR, the loop develops a spontaneous supercurrent for values of the parameter k below 1, which increases monotonically as k is lowered and reaches its maximum value $\Phi/\Phi_0 = 1$ for $k \to 0$. For the case of a sawtooth CPR the spontaneous flux shows a similar dependencs on k, but in this case there is also a spontaneous flux for larger values of k (smaller LI_C product). In other words, for a sawtooth CPR the flux-plot is hysteretic for all values of k.

Chapter 3

Experimental Topics

The sample preparation can be subdivided into three parts which are described in chronological order in the following sections. First the micro Hall sensors are fabricated from a GaAs/AlGaAs heterostructure and tested (see section 3.1). In the next section (3.2) the properties of several resists and mask systems, which are more or less suitable for shadow evaporation of Nb, are discussed. In the final preparation step, the metal layers to form the loop are deposited on top of the Hall sensors by vacuum deposition (section 3.3). A detailed collection of recipes containing all relevant parameters can be found in Appendix A.

3.1 Micro Hall Sensors

Basics

Micro Hall sensors have been used successfully to investigate the local magnetic stray field of individual mesoscopic objects such as nanomagnets or superconducting discs [35, 36, 37, 38, 39]. In this work, the micro Hall sensors are employed to observe the magnetic stray field produced by circulating currents in a superconducting loop. The micro Hall sensors are fabricated by means of optical lithography from a modulation doped GaAs/AlGaAs heterostructure which contains a 2-dimensional electron gas (2-DEG).

The starting material for the Hall sensors used in this experiment was grown by Prof. Wegscheider and his group. Because of the small lattice mismatch between GaAs and AlGaAs, epitaxial growth of heterostructures with highly ordered interfaces on an atomic scale is possible. Due to the different band gaps of the two semiconductors, a triangular potential well forms at the interface between the GaAs and the

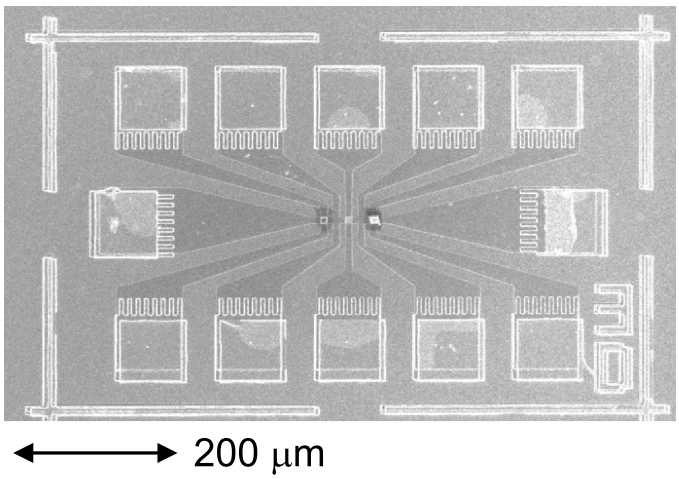

Figure 3.1: Image of a mesa structure etched from a GaAs/AlGaAs wafer containing five Hall crosses (three of them are occupied). The Hall crosses share on one common path which carries the driving current for all five sensors. The sensor area of the Hall crosses is a square of $8\,\mu$m side length. The electrical contact to the 2-DEG is mediated by twelve AuGe pads, which are distributed around the whole structure. In a second metallization step these contacts are covered by a 200 nm Au layer which is used for bonding pads.

$Al_xGa_{1-x}As$ layer. Electrons from the donator atoms are trapped in the potential well. The electrons move free in the plane of the GaAs/AlGaAs interface, while the movement in the direction normal to the interface is confined (2-DEG). The mobility of the 2-DEG electrons can be very high in such heterostructures since the donators and the conduction layer are spatially separated. Typical values for a 2-DEG which was successfully applied in this work[1] were a mobility of $\mu = 746\,000$ cm^2/Vs and an electron density of $n = 2.66 \times 10^{11}$cm^{-2}, both values measured at 4.2 K without illumination. The thickness of the cap layer[2] mainly determines the vertical distance (see Figure 3.2(b)) between the 2-DEG and the sample surface and was 190 nm in the sample described above. The thickness of the cap layer influences the coupling of the local stray field of the loop to the 2-DEG electrons and hence the signal strength which is summarized by the geometric filling-factor. The geometric filling-factor also depends on the details of the magnetic stray field, but in general a thicker cap layer means a greater distance from the loop to the sensor and therefore results in a smaller signal.

If the cap layer is thin, so that the 2-DEG is relatively close to the loop, the coupling is good. However it turned out that the loops deposited on the sample surface disturb the 2-DEG below them if the cap layer is too thin, which is attributed to

[1] wafer *C021009C* grown by M. Reinwald

[2] the uppermost layer in the sequence of the heterostructure

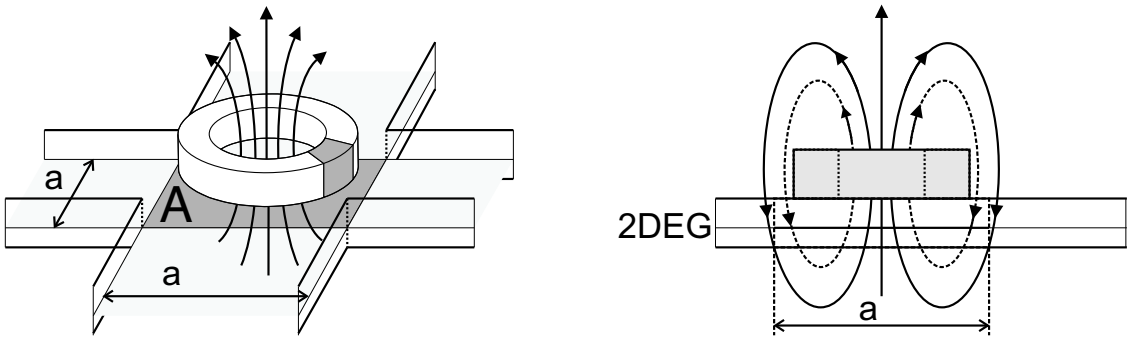

(a) (b)

Figure 3.2: Operation principle of the micro Hall sensor: (a) The superconducting loop is placed directly on top of the heterostructure which contains the 2-DEG. The dark gray shaded area below the loop denotes the active sensor area $A = a^2$ in the ballistic limit. (b) Cross-section of the loop on top of the micro Hall sensor where some magnetic flux lines are drawn schematically. Not all the flux lines produced by the circulating current in the loop are counted by the sensor: The dotted flux lines, for example, penetrate the active area twice in opposite directions, and therefore mutually cancel their contribution. The fraction of flux lines which are counted is described by the geometric filling factor α, which depends on the exact geometry of the sensor and the loop. For $\alpha = 100\%$ the coupling would be perfect and all the magnetic flux produced by the loop would be counted by the sensor.

piezo-electrical effects. This causes an increase of the noise in the Hall voltage of the occupied sensors as compared to the empty Hall crosses and spoils the sensitivity of the sensor [25]. A compromise between high coupling and low piezo-mechanical disturbance was found for cap layers in the range between 150 nm and 200 nm.

Principle of Operation

There are two modes of operation for the micro Hall sensor: If the 2-DEG electron mean free path is larger than the geometric dimensions of the sensor area, the sensor is in the ballistic limit. In this case, the active area is given by the square region $A = a^2$, as drawn in figures 3.2(a) and 3.2(b). It was shown by Peeters and Li, that in the ballistic case the Hall voltage measured by the device is proportional to the average magnetic flux penetrating the area A [40, 41].

If the electron mean free path is smaller than the size of the Hall cross, the device is in the diffusive regime. In this case, the active area is extended into the arms which define the sensor, when compared to the ballistic case. It was shown by Bending et

al. [42], that the Hall voltage measured in the diffusive case is still proportional to the magnetic flux penetrating the extended active area, but different parts of the active area contribute differently the Hall voltage. Due to the increased active area, the geometric filling-factor α can be affected when crossing from the ballistic to the diffusive regime.

In the samples discussed here, the mean free path is estimated to be of the order of $6\,\mu$m whereas the size of the sensor area is $8\,\mu\text{m} \times 8\,\mu\text{m}$. The sensor is hence operated in the quasi-ballistic regime at the crossover between purely ballistic and diffusive behavior.

The Hall voltage V_H is related to the magnetic flux Φ penetrating the active area by

$$V_H = \frac{\alpha}{ne}\Phi I/A. \tag{3.1}$$

Here n is the electron density of the sensor, e the electron charge, α is the geometric filling-factor of the loop within the flux sensor and I the ac driving current through the sensor [35].

It can be seen from equation 3.1 that the signal V_H can be increased by lowering the electron density of the 2-DEG. On the other hand, the technique of contacting the 2-DEG by AuGe contacts [43], sets a lower limit for the carrier density of around $1 - 2 \times 10^{11}\text{cm}^{-2}$. For even lower values of the carrier density, it turned out that it is not possible to reliably fabricate ohmic AuGe contacts to the 2-DEG.

When performing temperature sweeps, the Hall signal is superimposed by a temperature dependent signal originating from the temperature dependent longitudinal resistance of the Hall probe [44]. This contribution of the longitudinal resistance occurs due to structural imperfection of the Hall cross geometry: The shape and position of the two opposed potential probes of the sensor are never perfectly symmetric. A workaround for this temperature dependence of the signal is presented in section 4.4 where the corresponding measurements are discussed.

Figure 3.2(a) shows a schematic of the micro Hall sensor and the superconducting loop on top of the active area. The arrows indicate the inhomogeneous magnetic flux lines which originate from the circulating supercurrent in the loop and (partly) penetrate the active area A of the micro Hall sensor, denoted by the dark gray shaded area. The field produced by the loop is inhomogeneous, the exact distribution of the magnetic flux lines depends on the shape of loop as well as it's cross-section and the current distribution inside the superconductor.

In Figure 3.2(b) the cross section of the micro Hall sensor is drawn. As can be seen, some flux lines penetrate the active area once (solid line), while some other flux

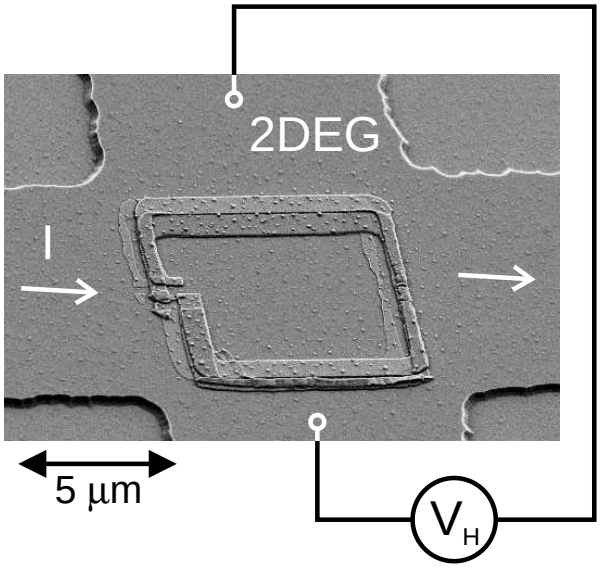

Figure 3.3: The SEM picture shows a superconducting loop with one Josephson junction situated on top of the active area of a micro Hall sensor. The sensor measures the local magnetic flux produced by the circulating supercurrents in the loop and was fabricated by optical lithography and wet etching from a GaAs/AlGaAs heterostructure. The ac driving current through the sensor ranges from $1\,\mu$A to $20\,\mu$A, depending on the investigated temperature range. The Hall voltage is pre-amplified and measured by standard lock-in technique (see section 4.1).

lines penetrate it twice, in opposite directions (dashed lines). In the latter case, the corresponding flux lines are not "counted" by the micro Hall sensor, because the Hall voltages generated by the two intersections of the flux line with the active area have opposite sign and cancel to zero. This partial coupling of the inhomogeneous flux produced by the loop into the sensor is taken into account by the geometric filling factor $\alpha < 100\%$. Knowledge of the filling factor is important in order to be able to measure the flux originating from the lops quantitatively (see section 4.3.4). For a sample like the one shown in Figure 3.3, the filling factor is about 3 % due to only partial filling of the loop in the sensor area.

Process Implementation

A brief description of the Hall cross fabrication is given below; details on the process parameters and recipes can be found in Appendix A as well as in [45].

The fabrication of the micro Hall sensors begins with spinning a layer of photoresist (Shipley S1805 or Allresist AR-P 3740) on the cleaned substrate and baking

it at 90 °C. In the subsequent steps, the mesa pattern is transferred to the substrate by optical lithography, development of the photoresist and wet etching of the GaAs/AlGaAs in a mixture of acetic acid and hydrogen peroxide. After the etching process, the remaining photoresist is washed away in acetone and the wafer is cleaned again.

Another layer of AR-P 3740 photoresist is spun on the sample and baked, then the pattern for the ohmic contacts is exposed after realignment in the mask aligner and developed. For the ohmic contacts an AuGe alloy covered by a layer of Ni is evaporated at a base pressure of around 5×10^{-6} mbar [43]. The lift-off is achieved in acetone. After that, the sample is heated up to 440 °C in an annealing oven, where the AuGe alloy melts and penetrates into the GaAs/AlGaAs heterostructure, where it is supposed to establish an ohmic contact to the 2-DEG.

At this point, the sample fabrication is interrupted and the quality of some contacts to the 2-DEG is spot tested. Therefore the I-V is taken at various conditions (illuminated/dark, room temperature/77 K). If the I-V curves are ohmic and the resistance of the sample and the contacts is reasonable, the contact pads are metalized (10 nm Cr and 200 nm Au) in a third optical lithography step, as described above for the AuGe/Ni metallization. This relatively thick Au metallization is used for bonding pads later on.

3.2 Thermostable Shadow Masks

The following section deals with the selection of a suitable shadow mask system for the electron gun evaporation of Niobium. Niobium is a very attractive material to be used as a superconductor in mesoscopic heterostructures e.g. because of its high critical temperature ($T_C^{bulk} = 9.2K$) which allows to investigate a wide temperature range. It is robust against the inverse proximity effect due to its low coherence length (see section 2.2). Furthermore, niobium forms relatively nice films when evaporated by electron gun or sputtered and oxidizes rather slowly.

The need for high critical currents across the weak link requires good interface transparencies between the superconducting electrodes and the layer which forms the weak link. Therefore the technique of shadow evaporation is applied, so all metal layers involved can be evaporated in the same vacuum run, thereby providing the best interface quality possible. As with all refractory metals, when evaporating niobium, a rather high temperature is needed to get a sufficiently high vapor pressure. These high temperatures (the melting point of niobium is 2468°C) make it necessary to use high power electron guns. The high thermal load imposes some requirements

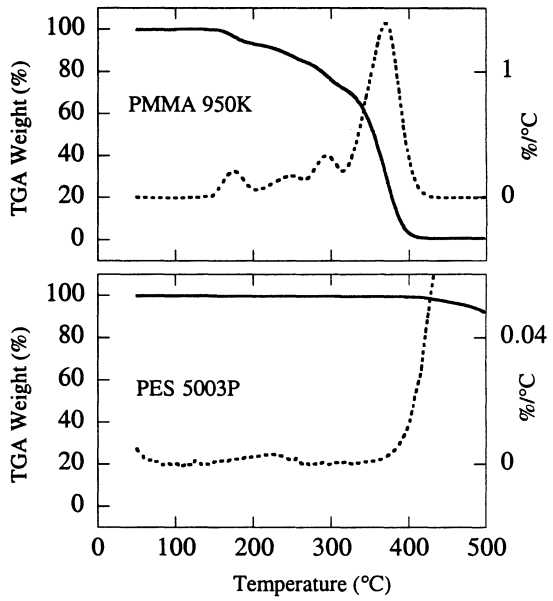

Figure 3.4: Weight loss (solid line) of PMMA (top panel) compared to PES (bottom panel) as a function of temperature and derivative of weight loss (dashed line). For PMMA, a pronounced outgassing is found for temperatures above 150 °C whereas the PES remains nearly unaffected up to temperatures of 400 °C. Note the different scales for the derivative of weight loss on both graphs [46].

upon the thermal stability of the mask system and is incompatible with standard mask systems containing Polymethylmethacrylate (PMMA).

Various mask systems have been tested for the shadow evaporation of Nb under UHV conditions. A summary of the different strategies is given in the following sections. The solution for all these requirements mentioned above is a thermostable shadow mask based on polyethersulfone (PES) as proposed by Dubos *et al.* [46].

PMMA masks

Evaporation mask systems containing PMMA are successfully used in combination with a broad variety of materials deposited in (ultra) high vacuum. PMMA is a high resolution resist for electron beam lithography and can also be used as a mask for vacuum deposition, which makes the deposition of a dedicated mask layer (and the structure transfer from the PMMA to the mask layer) unnecessary. By combining PMMA with more sensitive PMMA-MAA copolymers[3], double layer evaporation

[3]MAA stands for Methacrylic acid

masks with undercut can be produced. However, if PMMA is heated up during niobium evaporation, a pronounced decomposition and outgassing of the PMMA reduces the quality of the niobium layer, e.g. the critical temperature of mesoscopic niobium structures is significantly reduced if PMMA is present during deposition [47]. Furthermore the masks become mechanically unstable under the high heat load and suffers from deformation.

To illustrate the pronounced outgassing of PMMA, the upper part of Figure 3.4 shows the weight loss of a 950k (950.000 g/mole) PMMA sample when increasing the temperature from room temperature to 500°C, observed by a thermogravimetry analyser (TGA) [46]. It can be seen that above of 150 °C, which the sample can easily reach during electron beam evaporation of Niobium, a pronounced weight loss of the PMMA takes place which is attributed to outgassing. This outgassing causes severe contamination of the evaporated Nb which strongly getters the residual gases and makes the process useless for this application.

Si_3N_4/SiO_2 masks

To overcome this problem of organic resists like PMMA a process based on a silicon nitride mask on a spacer layer made of SiO_2 was introduced by Hoss et al. [48]. With this mask system a very good thermal stability as well as a high quality of the evaporated niobium structures was demonstrated. The drawback of this technique is the limited ability to perform a complete lift-off process after deposition. This means that remains of the deposited material which cover the whole mask can not or not completely be removed and might interfere with the investigated structure.

Anorganic Salts as Sacrificial Layer

During the early stage of this work, some efforts were made to utilize inorganic salts like AlF_3, SrF_2, MgF_2 or LiF as sacrificial layer underneath a Ge or silicon nitride mask. The salts are expected to be compatible with high temperatures and ultra high vacuum deposition.

The solubility of these salts can be tuned by using different concentrations of NaF in water. Therefore different concentrations of NaF in water could then provide a possibility to produce an undercut in a controlled way on the one hand and to perform a complete lift-off after deposition on the other.

Various deposition conditions from liquid nitrogen temperatures up to 300°C during salt evaporation have been tested in an evaporation system built up especially for

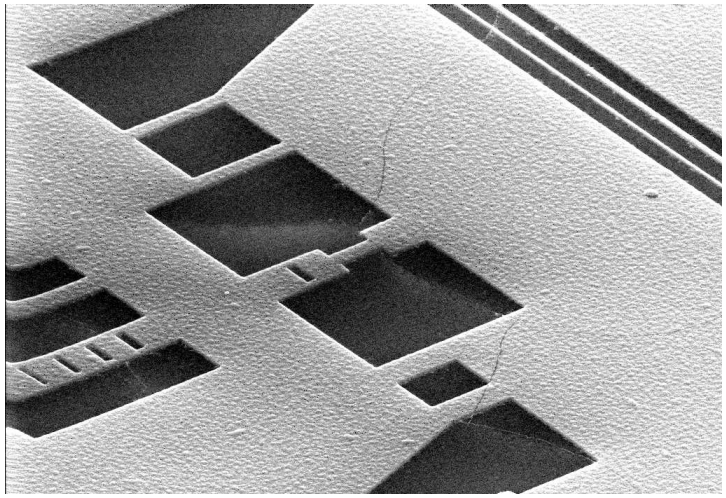

(a)

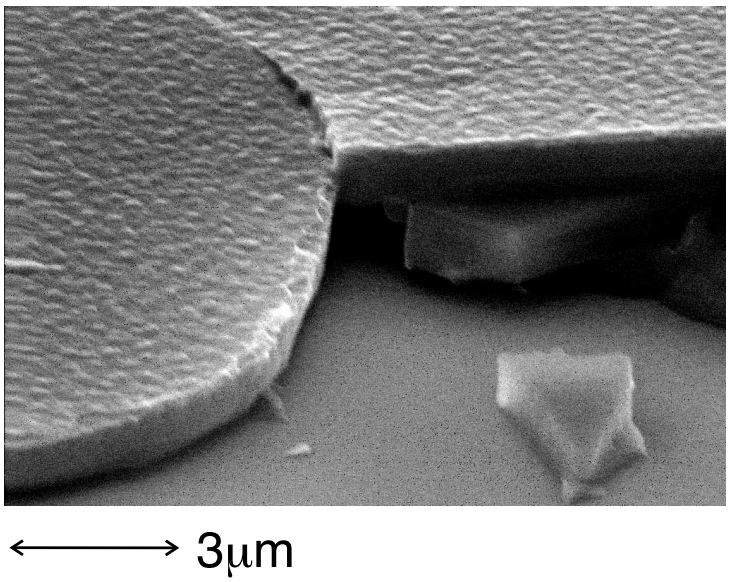

(b)

Figure 3.5: Attempts to use AlF_3 as sacrificial layer for shadow masks. (a) Test pattern etched into a Ge mask which was deposited on top of a 900 nm thick AlF_3 layer. The SEM picture shows cracks in the surface, which cover the whole sample. (b) Same mask system as in (a) after the attempt to produce an undercut by dissolving the AlF_3. The AlF_3 brakes away big chunks rather than being dissolved in a controlled way. The surface of the Ge layer is rough as a consequence of the columnar growth of the AlF_3 layer.

Material	Thickness	Description
PMMA	250 nm	e-beam resist and etch mask
Ge	50 nm	mask layer
AlF_3	900 nm	sacrificial layer

Table 3.1: Layer sequence of AlF_3/Ge masks.

this purpose. However, none of these experiments resulted in usable masks, as the evaporated salts of some hundred nm thickness formed cracked, porous, columnar layers rather than nice uniform films. Figure 3.5 shows some examples of SEM pictures of an AlF_3/Ge test mask. The conclusion of these attempts is, that the thin films formed by the evaporated salts which were used here are not homogeneous and flat enough to be used as sacrificial layers in shadow masks.

PES/Ge shadow masks

The spacer layer for the shadow masks which were finally used in this work and are compatible with Nb e-gun evaporation is made of the thermostable polymer Ultrason E2020 provided by BASF, following a process described by Dubos et al. [46]. The Ultrason resins are amorphous thermoplastics derived from polysulfone and polyethersulfone (PES) and offer very high robustness to heat, see Figure 3.4 lower panel and [49, 46]. The PES, which was provided in form of pellets, is dried and dissolved in 1-Methyl-2-Pyrrolidone (NMP) to give a 20% solution. The dissolved PES is transferred onto the sample in a resist spinner. For this step it is essential to keep the humidity of the air in the resist spinner low. Therefore the spinner is purged with nitrogen before and during the spinning of the resin. The humidity should not exceed 18% during the whole spinning process. The resulting layer thickness depends weakly on the spinning speed and mainly on the concentration of the solution, an is around 750 nm for the 20% solution at 3000 rpm (5 min.). After spinning, the PES is hard baked at 275 °C for one minute on the hotplate. The glass transition of the PES takes places around 253°C [46]. After that, a Germanium (Ge) layer of 60 nm thickness is evaporated onto the PES layer and covered by a PMMA electron lithography resist layer, which is used to structure the Ge mask. Then the PMMA is exposed and developed and the pattern is finally transferred into the Ge layer by using an Oxford Instruments reactive ion etching device (RIE, Plasmalab80Plus) with a $SiCl_4$ process. Later on in the same vacuum run, 30 minutes of O_2 plasma are applied in order to completely remove the PMMA and to produce the desired undercut by burning away the PES through the opened windows in the Ge mask.

Material	Thickness	Description
PMMA	250 nm	e-beam resist and etch mask
Ge	50 nm	mask layer
PES (20%)	750 nm	sacrificial layer

Table 3.2: Layer sequence of PES/Ge masks. This mask system was applied to fabricate the Nb/PdNi loops used in this work.

Figure 3.6 shows SEM pictures of a PES/Ge mask ready for vacuum deposition. The structure contains free standing Ge bridges, as can be seen in panel (a).

All the samples which have been measured in this PhD thesis have been fabricated using the PES/Ge masks described above. The results are usable, however it should be noted that after Nb deposition, tensions and/or thermal stress can result in cracked Ge bridges under bad conditions (see Figure 3.7). Cooling of the substrate and a larger Ge layer thickness can help to reduce this problem.

PES/Silicon Nitride Shadow Masks

To overcome this problem of cracks in the Ge bridges, a new mask system has been developed which also uses PES as sacrificial layer but a PECVD (plasma enhanced chemical vapor deposition) deposited silicon nitride layer as mask material. First test masks have been fabricated to demonstrate the capability of this process. After spinning and baking of the PES, the sample is transferred into a chamber for plasma enhanced chemical vapour deposition (PECVD, Oxford Plasmalab 80Plus) where the silicon nitride mask layer is grown at a temperature of 275°C using Silane as Si carrier and Ammonia as N_2 carrier[50]. In contrast to the Ge masks, the RIE etching of the silicon nitride is done in an Trifluoromethane plasma, which provides good selectivity to PMMA. Details of the process are given in Appendix A.

Figure 3.8 shows a SEM picture of a shadow mask made of PES and silicon nitride after deposition of a thin Au layer to enhance the contrast. It can be seen that there are free standing silicon nitride bridges due to the large undercut. To test the resistance to thermal stress, a 100 nm thick Nb layer was evaporated on the mask without cooling the substrate. This process imposes significant thermal load and stress to the mask; a PES/Ge mask is expected to break under these conditions (see Figure 3.7). The silicon nitride mask, in contrary, remained quite stable, which is attributed to the enhanced rigidity of the mask material. At two of three test loops, the Nb layer did not adhere on the nitride surface and rolled away (Figure 3.9(a)).

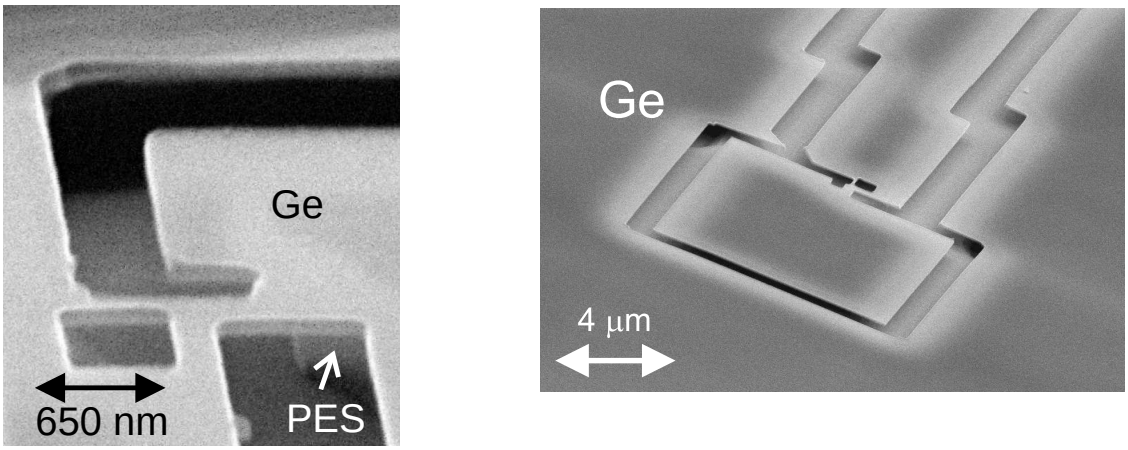

(a) (b)

Figure 3.6: (a) The SEM picture shows a shadow mask prior to evaporation. The top layer is a germanium film of 60 nm thickness which has been structured by electron beam lithography and reactive ion etching. The undercut is achieved by isotropic RIE etching of the underlying polyethersulfone (PES) layer in an oxygen plasma. The PES has been spun to a thickness of about 750 nm. (b) SEM picture of a PES/Ge shadow mask showing the complete loop. This loop is contacted by two current leads, which allow to send an external current through the loop.

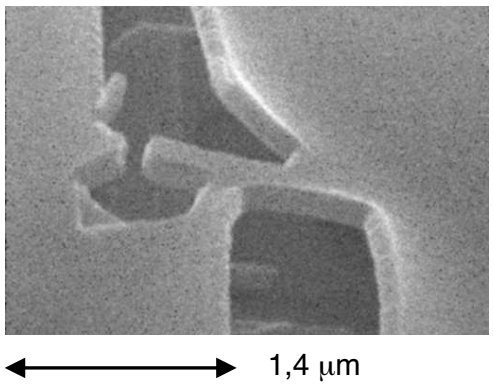

Figure 3.7: The evaporation of Nb imposes severe thermal stress upon the mask system. The SEM picture shows cracks in the Ge layer of a PES/Ge mask which occurred after e-gun deposition of 80 nm Nb without cooling.

Material	Thickness	Description
PMMA	250 nm	e-beam resist and etch mask
silicon nitride	60 nm	mask layer
PES (20%)	750 nm	sacrificial layer

Table 3.3: Layer sequence of PES/silicon nitride masks.

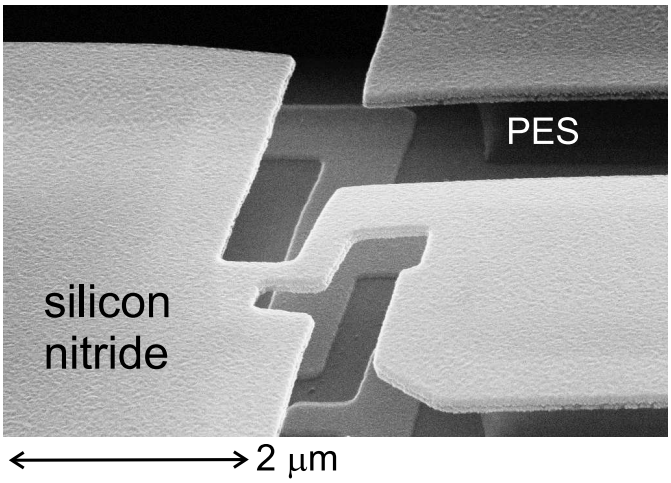

Figure 3.8: To overcome the problem of occasional cracks in the Ge layer after Nb deposition, a new mask system which uses silicon nitride as mask layer was developed. The SEM picture shows a PES/silicon nitride mask after deposition of a thin Au layer to enhance the SEM contrast.

The mask remained completely unaffected in this case. In the third structure (Figure 3.9(b)), the Nb bent the mask, however it did not brake, which reflects the mechanical stability of the material system and is a big improvement when compared to Ge masks.

3.3 Mask Layout

Figure 3.10 illustrates the mask layout used for the production of the SFS loops. The SFS junctions can not be realized by lateral bridge-type weak links due to the short coherence length in F (see section 2.2.2) and hence the small distance between the S-banks required for Josephson junctions. Instead, the junctions are designed as *planar* junctions, where the layer thickness of the ferromagnet determines the separation of the two superconducting electrodes forming the junction. The evaporation requires three metallization steps under different tilt angles which can be done within the

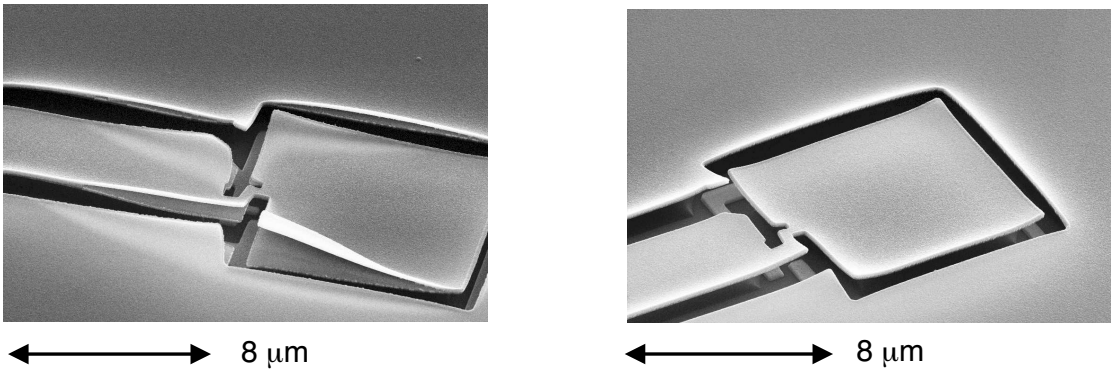

(a) (b)

Figure 3.9: SEM pictures of a PES/silicon nitride mask after deposition of 100 nm of Nb without cooling. (a) If the Nb does not adhere on the mask, the silicon nitride remains completely unaffected which reflects the good thermal stability of the system. (b) If the Nb adheres on the silicon nitride the Nb bends the mask layer. Still, no cracks occur in the Si_3N_4 layer.

Material	Thickness	tilt angle		translation on sample surface
Nb	40 nm	$\alpha = 0$	$\beta = 0$	0 nm
$Pd_{0.82}Ni_{0.18}$	7.5 nm	$\alpha = 43°$	$\beta = 0$	720 nm
Nb	40 nm	$\alpha = 0$	$\beta = 45°$	780 nm

Table 3.4: Typical evaporation schedule of a SFS loop for a mask height of 775 nm.

same vacuum run thanks to the shadow mask technique and provide the best possible interface quality. The evaporation steps are summarized in table 3.4. All evaporation sessions, most importantly the evaporation of the diluted ferromagnet PdNi used for the π-junctions (see section 3.4), were done by Dr. Marco Aprili in Orsay/Paris.

All evaporation was done by e-gun vacuum deposition at a base pressure of 10^{-9} mbar. During evaporation, the pressure typically rose up to the 10^{-8} mbar range [18]. The substrate was not cooled during evaporation. The layer sequence which is used to compose the desired loop-structure is summarized in table 3.4 and Figure 3.10. In the first step a 40 nm thick Nb layer is deposited under normal incidence to the sample surface (denoted by A in Figure 3.10). In the following step the diluted ferromagnet $Pd_{0.82}Ni_{0.18}$ (B), which is used as Josephson coupling layer, is deposited. The evaporation is done under a tilt angle of typically 40 °which shifts the PdNi pattern with respect to the Nb layer in the desired position and ensures a smooth covering of the bottom Nb, especially of the edge, by the relatively thin PdNi

layer (7.5 nm). Finally the top Nb layer is evaporated, again with an thickness of 40 nm, under a different tilt angle, to close the superconducting loop. The result is a Nb loop which is interrupted by a sandwich type ferromagnetic Josephson junction.

Final Preparation

After deposition of the metals, the shadow mask system is removed in warm (50°C) n-methyl-2-pyrollidone (NMP), possibly supported by an ultrasonic bath. This step removes the shadow mask together with all the unwanted material deposited on top of the mask layer and leaves only the material deposited on the sample surface. This metal layer consists of important parts, which form the loop, and less important parts, which are pure *ghost images*, inherent to the technique of shadow evaporation (see Figure 3.10). It should be noted that the lift-off process can be affected by detailed mask investigation in the SEM prior to the lift-off. Investigations of the masks with high magnification and high beam currents locally reduces the solubility of the PES and may prevent a complete lift-off.

A typical chip contains several Hall bar structures. The chip is cleaved and the individual Hall bars are separated. One or two Hall bars are then glued into a ceramic chip-carrier (20 pins) with PMMA. To establish the electrical connection, the fully processed chip is wire bonded to the chip-carrier using either Au or Al wires of 25 μm diameter.

3.4 Properties of the Diluted Ferromagnet PdNi

The ferromagnet which is used for the Josephson junctions in this work is the alloy PdNi. Pd is paramagnetic with a Stoner factor of 10, close to the transition to ferromagnetism. Only a small addition of the ferromagnetic Ni (2.5%) is necessary to cross the border from paramagnetic to ferromagnetic behavior. The PdNi alloy is a *diluted ferromagnet* whose magnetization and Curie temperature can be adjusted by the amount of Ni. Figure 3.11 shows the dependence of the Curie temperature and the magnetization of the PdNi alloy on the Ni concentration [51, 52]. It was found in [52] that below a concentration of 5% of Ni, the magnetization of the alloy is not homogeneous. The Curie temperature and the magnetization increase with increasing Ni concentration.

In the Stoner model, the short-range potential corresponding to the screened Coulomb interaction between electrons can be replaced by a constant [53]. The exchange field

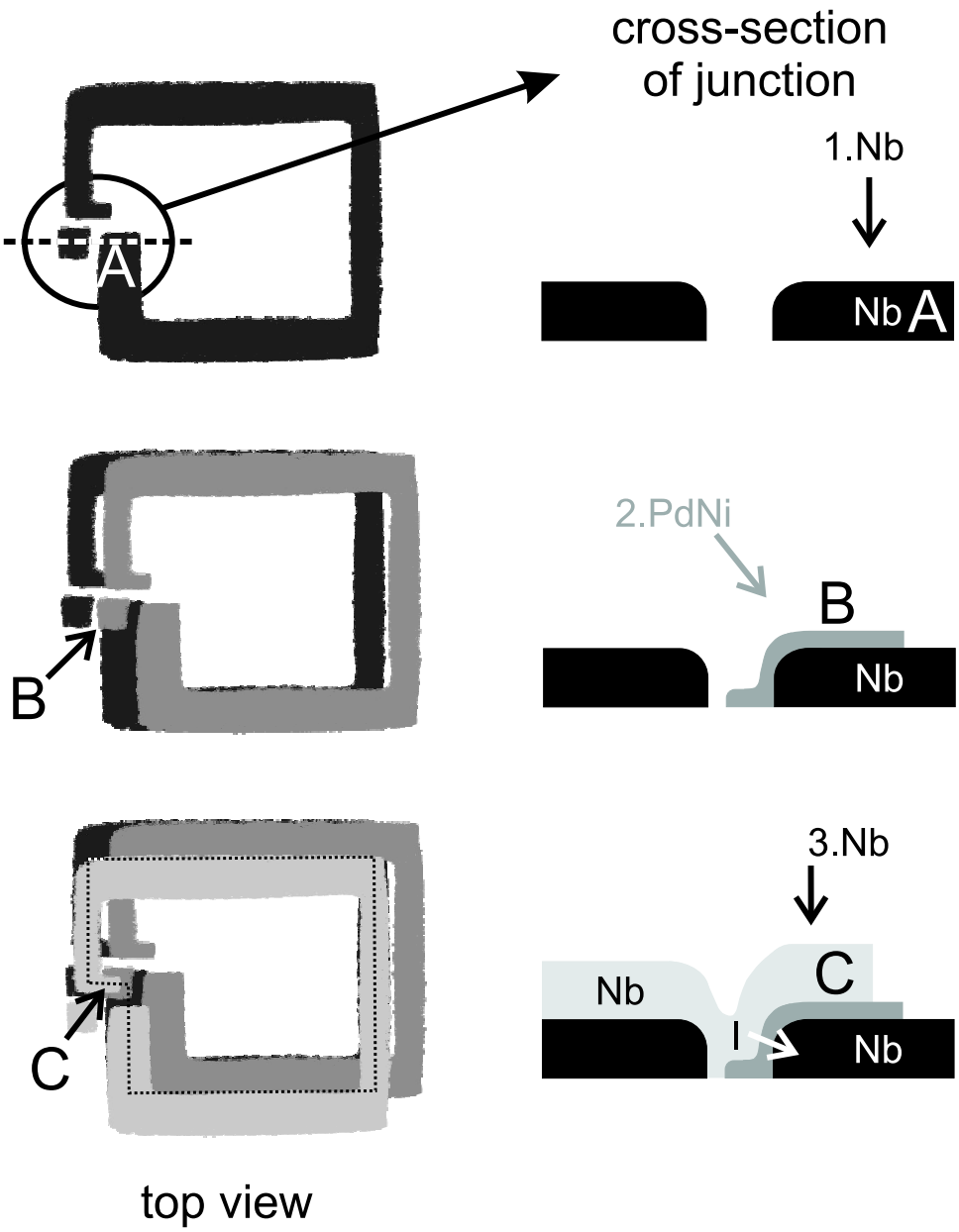

Figure 3.10: The evaporation of the SFS loop layer by layer using the shadow mask technique. By evaporating the three metal layers under different tilt angles, the desired structure on the sample is achieved with the best possible interface quality, as the evaporation is done without breaking the vacuum. In the first step, the bottom Nb layer (A) is evaporated under normal incidence. In the second step, the ferromagnetic alloy PdNi is evaporated. To do so, the mask is tilted in such a way that the square window (B) overlaps the bottom electrode (A). As the PdNi beam arrives from the side, the edge of the bottom electrode is covered smoothly, and cracks in the PdNi layer are prevented. Finally, the top Nb electrode (C) completes the loop. The black dotted line in the panel at the left side at the bottom illustrates a current path.

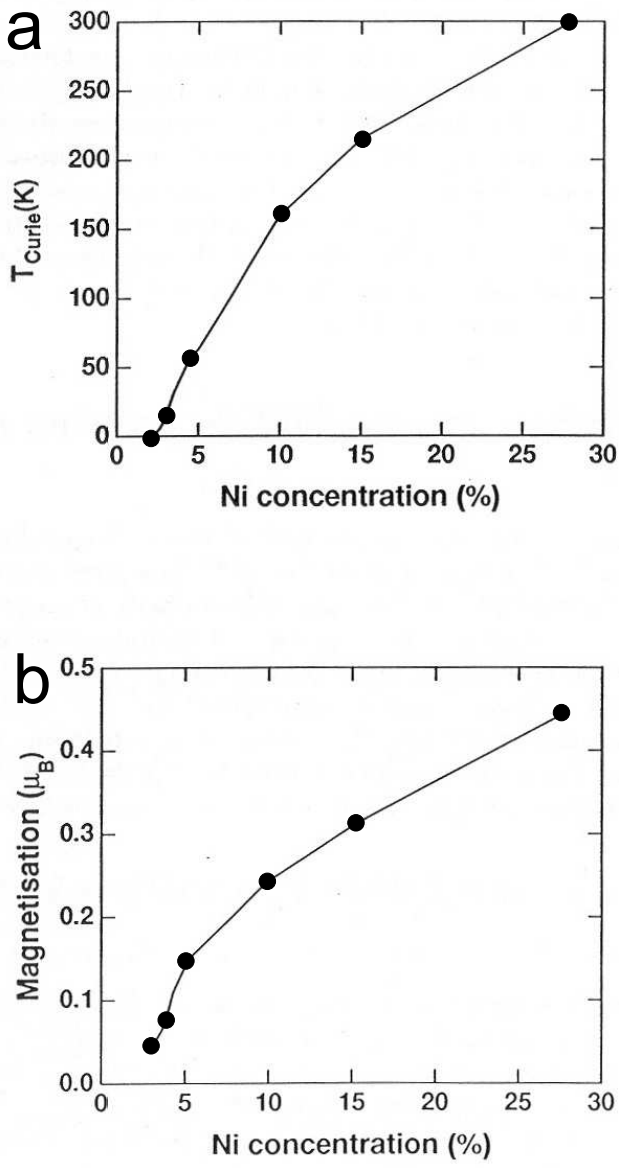

Figure 3.11: Dependence of the Curie temperature (a) and the magnetization (b) of PdNi layers on the Ni concentration ([51], there from [52]). In the samples used in the present work, the Ni content is 18 %.

can then be derived from the saturation magnetization by

$$M_S = \mu_B N(E_F) S_{Stoner} H_{ex}, \tag{3.2}$$

S_{Stoner} is the Stoner factor of Pd, $N(E_F)$ the density of states at the Fermi energy in Pd and μ_B Bohr's magneton. $N(E_F)$ has been estimated to $1.97\,eV^{-1}at.^{-1}$[51]. The Stoner factor enhances the static susceptibility relative to that of the free electron gas. If magnetic impurities (e.g. Fe or Ni) are diluted in a metal close to the magnetic instability (e.g. Pd), this enhancement of the susceptibility gives rise to bubbles of polarized electrons in the vicinity of the magnetic impurities [53].

The evaporation is done by e-gun from one crucible which contains a slug of PdNi alloy. The composition of the alloy undergoes some gradual enrichment of Ni due to a distillation effect which results from the different vapor pressures of the two materials.

In our samples the composition of the alloy is $Pd_{0.82}Ni_{0.18}$. For this Ni concentration, the Curie temperature measured by the anomalous Hall effect in a bare thin film is of the order of 200 K [51]. The exchange energy has been estimated by fitting the $I_C R_N$ product as a function of d_F [5] (Figure 2.8). For a Ni content of 12 % (used in [5]), E_{ex} was estimated to be about 35 meV. By assuming a linear growth of the exchange energy with Ni content, E_{ex} is estimated to be of the order of 52 meV in this experiment [18].

Figure 3.12 shows a hysteretic curve of a PdNi layer (upper panel) and the temperature dependence (lower panel) of the saturation magnetization as measured by the anomalous Hall effect. In the hysteretic curve, it can be seen that the coercive field is of the order of 400 mT, which is much larger than the fields typically applied during the measurements of this work (some 100 μT). Therefore it is concluded, that the magnetization of the PdNi layer is not affected by the small fields used to measure the samples as described in the next chapter. From the temperature dependence in the lower part of Figure 3.12 it can be further concluded that the temperature variation during measurement, typically between 1 K and 10 K also does not affects the magnetization of the PdNi layer, which shows no significant temperature dependence in this region.

Another example for a successfully applied diluted ferromagnet to fabricate ferromagnetic π junctions is CuNi. It is used by Ryazanov et al. (e.g. $Cu_{0.48}Ni_{0.52}$ [26, 54]) and Sellier et al. ($Cu_{0.52}Ni_{0.48}$ [24, 23]). The onset of ferromagnetism in $Cu_{1-x}Ni_x$ is at x=0.44.

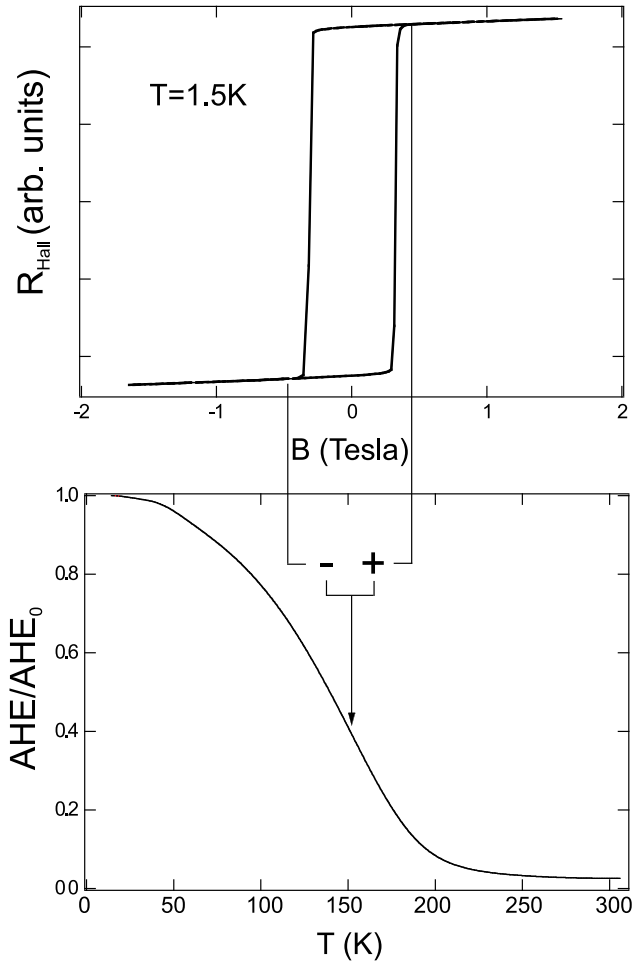

Figure 3.12: Magnetic properties of a plain $Pd_{0.80}Ni_{0.20}$ layer of 12 nm thickness. The upper curve shows an (out-of-plane) hysteretic curve obtained by the measurement of the anomalous Hall effect. The coercive field is around 400 mT and is much larger than the fields applied during the measurements described in chapter 4. In the lower curve the temperature dependence of the saturation magnetization is shown. The Curie temperature is about 190 K [18].

Chapter 4

Measurements and Discussion of Results

In this chapter the low-temperature measurement setup and the results of this work will be discussed. In the first section, the measurement setup is introduced. After that, measurements which are required to characterize the quality of the mask system and the Nb are presented. In section 4.3 magnetic field sweeps of a superconducting loop with integrated ferromagnetic Josephson junction are presented, which reveal the π-character of our junctions. An estimation of the residual magnetic field at the sample and the temperature dependence of the critical current of the investigated junctions is given. Section 4.4 contains the main result, the direct observation of the spontaneous magnetic flux in π-loops [7]. Finally, in section 4.5, some results from loops which show additional features in the flux quantization pattern are presented.

4.1 Measurement Setup

An overview of the low temperature measurement setup and the used electrical equipment is given in Figure 4.1. The Hall voltage is measured by standard Lock-in amplifiers, optionally supplemented by rf-shielded low-noise preamplifiers. For the data acquisition, *Measure XP*, an adaptive Windows program[1] was used, which features an automated batch mode to conveniently cover a big range of measurement parameters.

[1] developed by Johannes Bentner [25]

Cryostat

The core of the measurement setup is an Oxford Heliox ^{3}He cryostat which allows to adjust and sweep the temperature from nearly room temperature down to 300 mK. The measurements presented here were done in the temperature range between 300 mK and 10 K. The system is equipped with an superconducting magnet which can produce fields up to 12 T. This magnet however is not employed in the presented measurement and was demagnetized in order to avoid trapped flux.

Filtering and Shielding

There are 20 measurement lines from room temperature to the sample which are implemented as 10 twisted pairs. Four pairs are realized by coaxial wires, the remaining 6 pairs are simple lacquer insulated wires. The measurement lines are π-filtered at room temperature and additionally filtered by copper powder filters [55] at cryogenic temperatures.

In the cryostat, the sample can be magnetically shielded. For effective magnetic shielding, a tradeoff between permeability and saturation magnetization of the shielding material is necessary to achieve best attenuation of residual magnetic stray fields. *Cryoperm 10* is a Ni based alloy especially designed for magnetic shielding applications at cryogenic temperatures. In our Oxford Heliox system, a cryoperm cup can be installed. It encloses the sample holder, only the cap remains open. The cup is reducing the residual magnetic field present at the sample by a factor of 30 and 10, in horizontal and vertical direction, respectively (see Figure 4.2).

The remaining residual magnetic field is estimated to about 4 μT, as determined by symmetry properties of magnetic field sweeps, see section (4.3.3).

An external magnetic field can be applied to the sample by a pair of small superconducting Helmholtz coils, which are wrapped directly around the ceramic sample holder inside the cryoperm cup. The wire used for the coils consists of superconducting filaments embedded in a copper matrix.

Electrical Equipment

The ac driving current for the operation of the micro-Hall sensors is provided by a Stanford Research SR-830 digital lock-in amplifier. Because the lock-in amplifier has a fixed voltage output, a defined current is applied via a series resistance of 100 kΩ or 1 MΩ at room temperature, which is much larger than the typical resistance of the

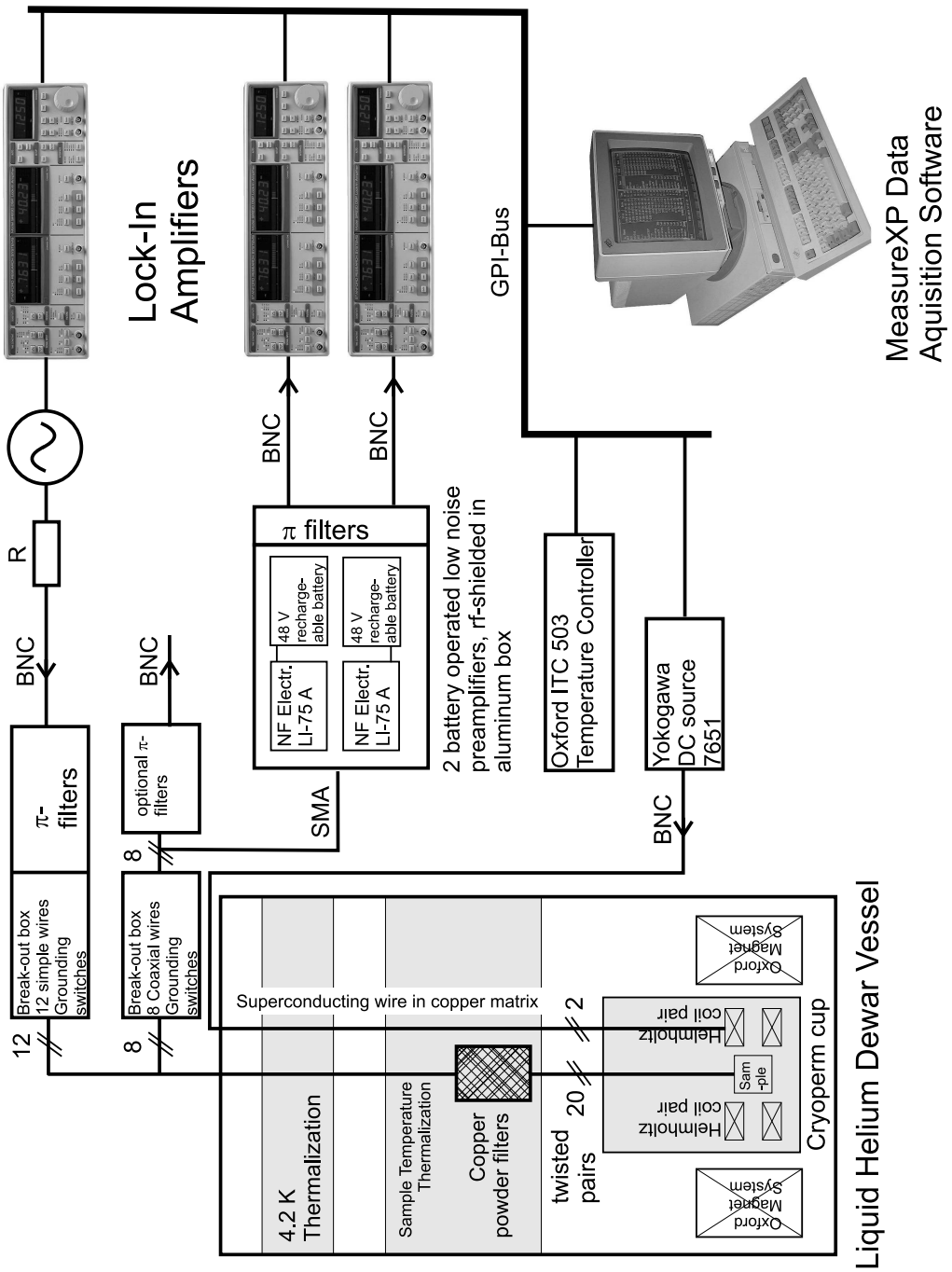

Figure 4.1: Overview of the low temperature measurement setup based on an Oxford Heliox cryostat and Stanford Research lock-in amplifiers.

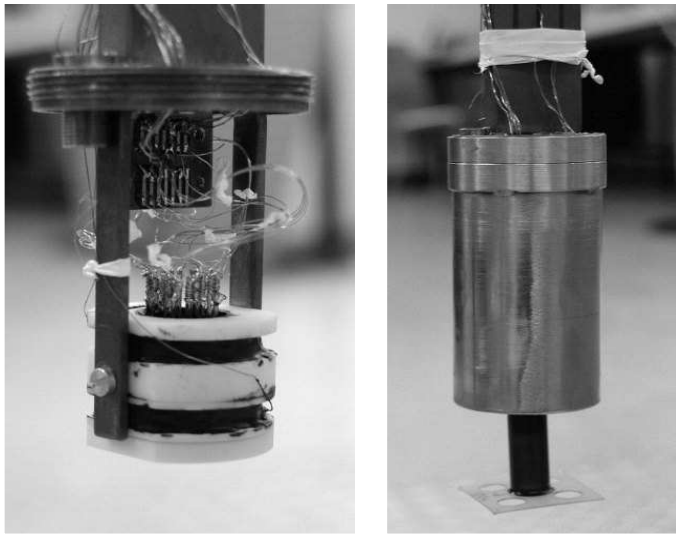

Figure 4.2: Picture of the low temperature sample holder without (left) and with (right) fitted cryoperm cup for magnetic shielding. The residual magnetic field is damped by a factor of 30 and 10 in horizontal and vertical direction, respectively. The black bars around the ceramic sample holder (white), shown in the left picture, are the Helmholtz coils which are used to apply an external magnetic field to the sample.

current path at 4 K, which is of the order of 1 kΩ. The driving current ranged between 1 μA and 20 μA, depending on the temperature; at low temperatures the driving current has been reduced to avoid heating. The frequency of the driving current was between 100 Hz and 300 Hz. Typically the current is applied via the simple lacquer isolated lines; the coaxial cables are normally used for the measurement of the Hall signals. The Hall voltages of up to four Hall crosses on the sample can be measured at the same time by a stack of SR-830 digital lock-in amplifiers. To improve the signal to noise ratio, two Hall voltages can be amplified by a pair of battery operated low-noise preamplifiers (NF-electronics) at room temperature. The preamplifiers and the batteries are rf-shielded in a massive aluminum box. To drive a current through the Helmholtz coils at the sample holder, a Yokogawa current source is used. The temperature is measured and controlled by an Oxford ITC-503 temperature controller.

All the measurement and controlling equipment is connected to a Windows PC by GPIB. The homemade [25] measurement software allows for fully automated data acquisition and controls all relevant parameters by employing batch jobs.

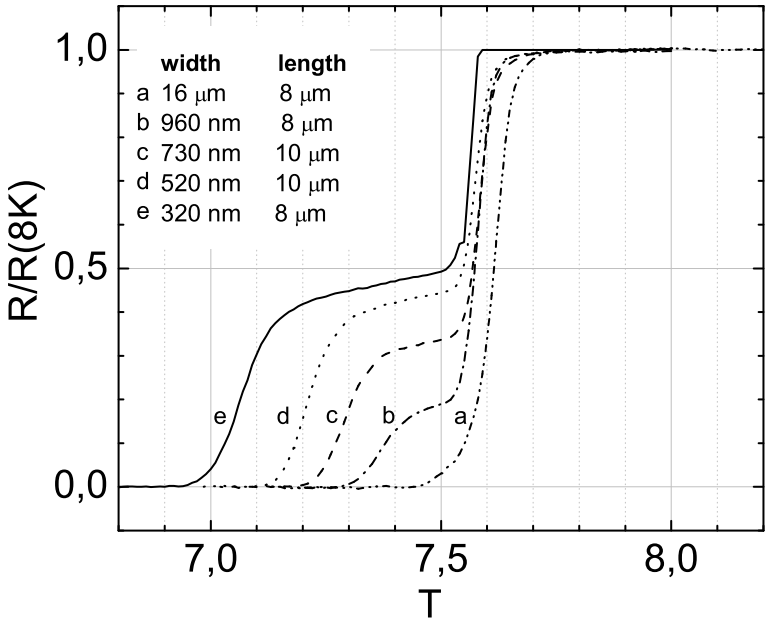

Figure 4.3: To test the quality of the shadow mask system and to verify the compatibility with the e-gun evaporation of Nb, the transition temperature of mesoscopic Nb wires has been measured. The transition is observed at 7.1 K for the smallest wire (e), which is acceptable compared to a bulk value of 9.2 K.

4.2 Verification of the Nb Quality

Before the actual measurements started, the quality of the shadow masks and the resulting quality of the evaporated Nb was verified. Therefore wires of Nb were structured and the corresponding T_C was measured in a four probe setup. The shadow mask system which was used is made of PES/Ge and is identical to the system used in the following experiments with SFS loops. The length of the investigated Nb wires ranged from 8 μm to 10 μm, the width from 320 nm to 16 μm (see inset of Figure 4.3). Except for the widest wire with a width of 16 μm, all samples consist of 5 identical wires in parallel. The deposition of the Nb was done with a rate of 3–4 Å/s at a background pressure of 10^{-8} mbar by e-gun in Regensburg. A cryogenic cooling shroud was used and the sample temperature during deposition was kept between -65° C and -10° C. The thickness of the Nb film is 60 nm.

Figure 4.3 shows the reduced resistance of various test wires as a function of temperature. The measurement current was 100 nA. For the thinner wires, the transition

to the zero resistance state occurs in two steps. The first step (at 7.6 K) is attributed to the contact pads and the feeding lines. The second step reflects the superconducting transition of the test wires. For the smallest wire (width 320 nm, length 8 μm) the transition was observed at 7.1 K. This value is acceptable for the dimensions of the device. The best T_C obtained for unstructured films deposited from this source at that time[2] was 8.4 K. The residual resistance ratio of the Nb thin films is $RRR = R_{293\,K}/R_{10\,K} = 1,9$.

4.3 Magnetic Field Sweeps

The characteristic signature of the π-junctions is the π-shifted current phase relation compared to 0-junctions (see Figure 2.7). To measure the characteristic fingerprint the CPR impresses upon the switching pattern (see Figures 2.10(a) and 2.10(b)), it is necessary to be able to adjust the phase difference φ across the Josephson junction and to observe the supercurrent across the junction associated with the adjusted phase difference.

4.3.1 Controlling the phase difference

In order to be able to tune the phase difference, the Josephson junction is inserted into a superconducting loop, as discussed in section 2.4. It was derived that the gauge invariant phase difference across the weak link φ_J^* depends on the total flux Φ through the loop according to

$$\varphi_J^* = 2\pi n - 2\pi\frac{\Phi}{\Phi_0}, \tag{4.1}$$

where Φ_0 is the flux quantum (equation 2.28) and n is an integer. The total flux through the loop Φ is given by the externally applied flux and the flux produced by circulating currents in the loop

$$\Phi = \Phi_{applied} - LI_S(2\pi\frac{\Phi}{\Phi_0}). \tag{4.2}$$

If the LI_s term can be neglected (small LI_C product), the phase difference across the weak link can be conveniently controlled by applying an external magnetic flux

[2]The quality of the Nb slug in the e-gun crucible improves with an increasing number of heat-up cycles; at that time, the slug was relatively new.

$\Phi_{applied}$ through the loop. For large LI_C products, a self agitation of the loop has to be taken into account and the total flux through the loop depends on the applied flux in a non-linear way (see equations 2.33 and 2.34).

4.3.2 Measurement of the circulating current

The circulating supercurrent I_S together with the inductance L of the loop produces local magnetic flux which is detected by the micro-Hall sensor in these experiment. The inductance of the loop with a diameter of $8\,\mu$m is estimated to 26 pH [56], see section 4.3.4.

Not only the magnetic flux produced by the loop but also the magnetic flux from the externally applied field is detected by the Hall-sensor. A typical raw-data measurement curve which shows the Hall voltage V_H over $B_{applied}$ is displayed in Figure 4.4(a). It can be seen that the curve is governed by a linear dependence resulting from the homogeneous externally applied field, which couples to the sensor by 100 percent. The inhomogeneous magnetic flux originating from the loop adds only small modulations to the linear background (indicated by circles in Figure 4.4(a)). These modulations couple to the sensor by less than 100 percent, which is reflected by the geometric filling factor α from equation 3.1 which was estimated to be about 3.5 % for this sample. The geometric filling factor depends on several factors, e.g. how complete the loop covers the active area of sensor, the thickness of the cap layer and the loop's cross section.

To extract the magnetic signal resulting from the loop, the contribution of the applied field has to be removed by subtracting a straight line in the V_H over $B_{applied}$ plot. This has been done in Figure 4.4(b): the remaining Hall signal δV_H originates from the circulating currents in the loop and is two orders of magnitude smaller than the original Hall-voltage. The characteristic sawtooth-shape of this signal will be explained in the following sections.

It should be noted that exact knowledge of both, the inductance of the loop and the geometric filling factor α in equation 3.1 is required in order to measure the circulating supercurrent quantitatively. The filling factor can be estimated by relating the jump height of the Hall-voltage to one (fraction) of a flux quantum deep in the hysteretic regime (large LI_C product). However, in order to extract the exact value of α knowledge of the shape of the CPR would be necessary or vice versa [25].

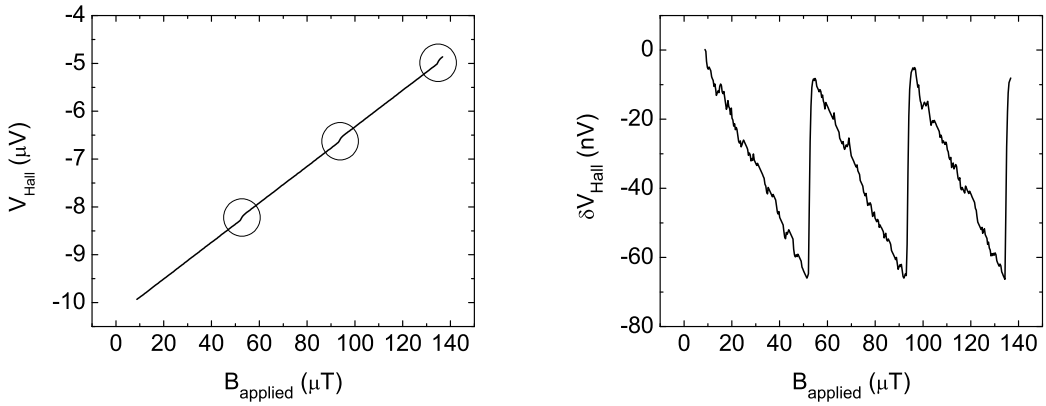

(a) (b)

Figure 4.4: Panel (a) shows the measured Hall voltage resulting from a superconducting loop with Josephson junction when sweeping an external magnetic field. The curve is dominated by a linear dependence which results from the external field, whereas the small modulation is generated by the loop, which couples to the sensor much weaker and can hardly be seen in the raw data (highlighted by the circles). By subtracting a straight line, the linear contribution is removed and the response of the loop is extracted, as shown in panel (b). The measurement current was $20\,\mu$A at a temperature of 2 K.

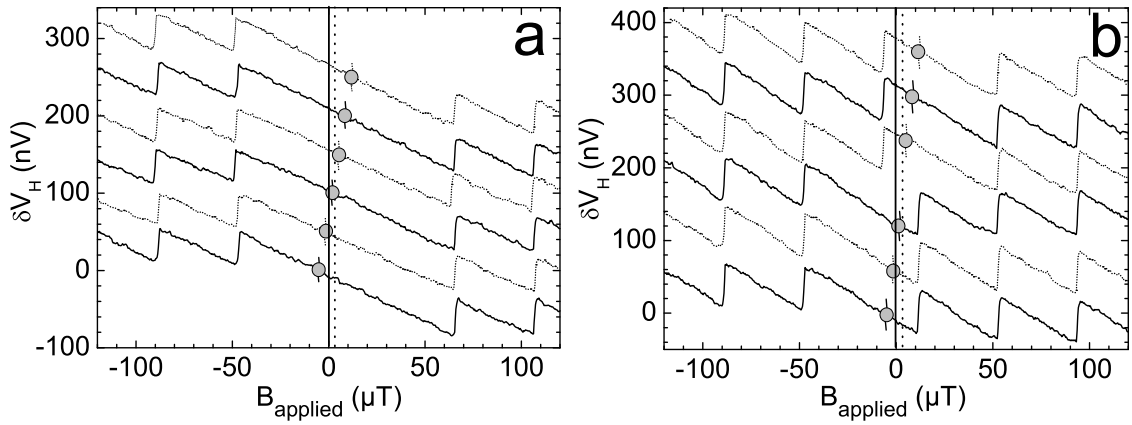

Figure 4.5: (a) Hall voltage produced by the 0-loop as a function of the applied magnetic field. Six different values of the starting field B_{start} (denoted by the gray dots) between -10 μT and 10 μT are shown; the curves are offset for clarity. The symmetry of the Hall voltage jumps with respect to zero applied field allows for an estimation of the residual magnetic field of about 4 μT (indicated by the dotted vertical line). (b) The same plot for the π-loop: By choosing various values of B_{start} around zero applied field, two different branches of the flux-plot (Figure 2.10(b)) can be selected, resulting in the asymmetric switching pattern (discussion see section 4.3.5).

4.3.3 Estimation of the residual magnetic field

The first type of measurements, to characterize the loops, consists of a series of magnetic field sweeps. All traces are obtained after field cooling from above T_C and start at slightly (some μT) different values of the magnetic field (B_{start}). A selection of these curves is plotted in Figures 4.5(a) (0-loop) and 4.5(b) (π-loop). The dots in each graph mark the six different values of the fields B_{start}, which range from about -10 μT to 10 μT. It can also be seen that each value of B_{start} has been measured twice, once in the up- and down-sweep direction. The curves are offset for clarity.

The 0-loop (Figure 4.5(a)) and the π-loop (Figure 4.5(b)) show a characteristic difference in the symmetry properties with respect to reversal of the magnetic field. This is already a signature of the 0- and π-state of the corresponding Josephson junctions, as will be discussed in detail in section 4.3.5. Here, graph 4.5(a) shall be used to illustrate how the residual magnetic field (with fitted cryoperm cup, see section 4.1) can be estimated from this type of measurement.

The position of the Hall voltage jumps in the traces shown in Figure 4.5(a) have to be symmetric with respect to $B_{applied}$=0 (see the flux-plot for a 0-loop Figure 2.10(a)). Therefore, with a known value of B_{start} and one up- and down-sweep starting at

this field, the real zero magnetic field is just exactly in the middle between the first jump in the down- and upsweep-trace and can directly be measured from the plot. By doing so, the value of the residual field has been identified to be about 4μT, and is indicated in Figures 4.5(a) and 4.5(b) by the dotted vertical line. In all the following graphs, the offset field has been corrected.

4.3.4 Estimation of the Critical Current Density

The complete magnetization cycles (Figure 4.6) can be used for an indirect estimation of the critical current density of the Josephson-junction enclosed in the loop. This procedure is less accurate and less straight forward than a transport measurement, however it is the only non-destructive way to get the value of the critical current from the isolated loop. To do transport measurements, it would be necessary to cut the superconducting loop, e.g. by dry etching, and to connect current and voltage leads to the junction in additional lithography and metallization steps in order to be able to perform a four point measurement.

Starting point for the estimation of the critical current density is the assumption, that at low temperatures ($LI_C \gg \Phi_0/2$) the jump height of the Hall voltage corresponds to one flux quantum, see Figure 2.10(a). It can be seen that this assumption is in general not justified. The jump height depends on $k = \Phi_0/2\pi LI_C$ (see equation 2.35), that is I_C and L, and on the shape of the CPR. To specify the fraction of one flux quantum which corresponds to the jump height, the knowledge of the exact shape of the CPR is necessary [25]. This knowledge requires the value of the filling factor α whose assignation relies basically on the same assumption[3]. As there are two unknown variables with one equation this problem can not be solved exactly.

To estimate the filling factor α, the jump height deep in the hysteretic regime at 1 K ($k \approx 0.1$ for the 0-loop) is related to one flux quantum Φ_0. Using this value of α, the critical currents are estimated, as shown in the following paragraphs. At the end of the section, the systematic error occurring thereby is quantified.

The Hall voltage (equation 3.1) can be related to an homogeneous flux penetrating the active area of the sensor by sweeping the external magnetic field and measuring the Hall voltage of an empty Hall cross. By doing so, the Hall voltage $V_H^{\Phi_0}(homogeneous)$ which corresponds to one flux quantum for a filling factor of 100 % can be obtained. The signal resulting from one flux quantum produced by the loop $V_H^{\Phi_0}(loop)$ is smaller, because the field produced by the loop is not homogeneous and couples to the sensor much weaker than the externally applied flux (see

[3] that one Hall voltage jump corresponds to Φ_0

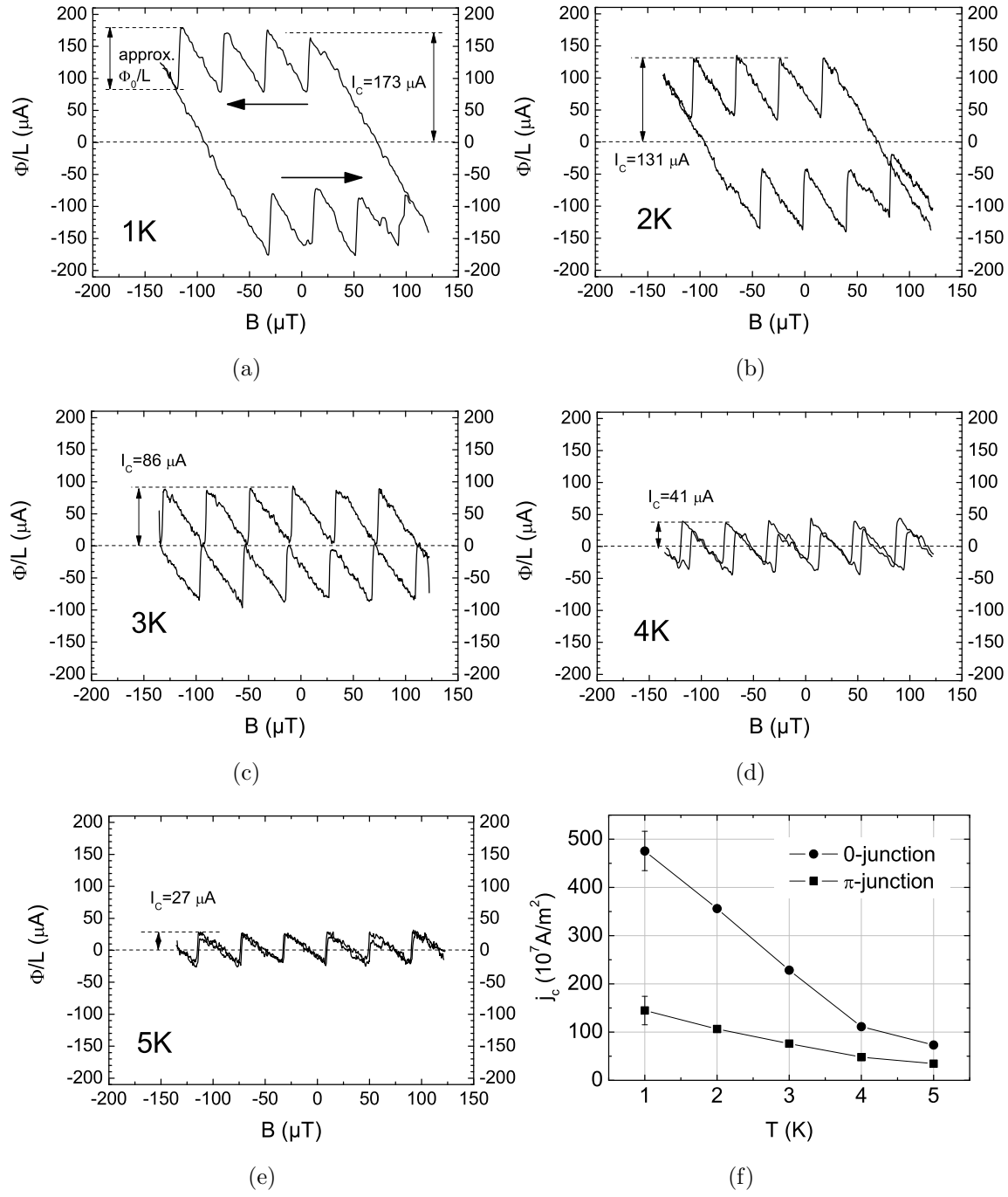

Figure 4.6: The magnetization curves plotted in panels (a) through (e) show data obtained from a 0-loop measured at different temperatures. As indicated by the arrows, these curves are used for an indirect estimation of the critical current density of the Josephson-junctions as a function of temperature, which is displayed in panel (f). The error bars represent the statistical error, the systematic error is about 20 % and results from the approximation that the jump height of the Hall voltage corresponds to one flux quantum (see text).

section 3.1). The geometric filling factor α (equation 3.1) can be calculated by comparing the actually measured jump height resulting from the loop (corresponding to approximately one flux quantum) to the expected height assuming α =100 %

$$\alpha = \frac{V_H^{\Phi_0}(loop)}{V_H^{\Phi_0}(homogeneous)}. \tag{4.3}$$

The fraction of the measured in the expected Hall signal is the geometric filling factor. In these experiments, it was relatively small ($\alpha \approx 3.5\,\%$), due to only partial filling of the active area by the loop (see Figure 3.3).

If α is known, the Hall voltage resulting from the loop can be translated in magnetic flux. To convert the axis which measures the magnetic flux in a circulating current in the loop, the axis has to be divided by the inductance of the loop. Therefore, the inductance of the loop is approximated using a formula for the inductance of a square of round wire, found in the textbook of Grover, p. 60 [56]:

$$L(s,r) = 0.008 \left[\ln \frac{s}{r} - 0.77401 + \frac{1}{4}\right] s \tag{4.4}$$

where s is the sidelength of the square and r is the radius of the wire. The radius of the wire is set to 25 nm, thereby assuming a penetration depth for Nb of 50 nm; as an average sidelength 6.5 μm is used. The resulting calculated inductance of the loop is L=26 pH.

The procedure to extract the critical current density from the magnetization cycles is shown in Figure 4.6, panels (a) through (e). A complete magnetization cycle (down- and up-sweep) is taken at various temperatures (1 K in panel (a) up to 5 K in panel (e), in steps of 1 K). The maximum circulating current, which is reached immediately prior to a jump, is the critical current of the junction. If the critical current is divided by the junction area, the critical current density is obtained. By averaging over some peaks in the curve, the statistical error is below 10 μA.

The result is plotted in Figure 4.6(f) for a 0- and π-loop for the temperature range between 5 K and 1 K. The corresponding values of the parameter k (equation 2.35) and the expected spontaneous flux (Figure 2.14) are given in table 4.1. For 6 K the jumps can not be distinguished from the noise. The amplitude of the noise is equivalent to 10 μA (0-loop) and 15 μA (π-loop), which is taken as an upper limit for $I_C(6\,K)$. For these value of the critical current k is larger than 1 and the corresponding flux is 0 (see Figure 2.14).

If the parameter k obtained from the critical current at 1 K and the calculated inductance is used to generate a flux-plot for the two limiting cases of the CPR (sinusoidal

	zero-loop			π-loop		
T [K]	I_C [μA]	k	Φ/Φ_0	I_C [μA]	k	Φ/Φ_0
1	173	0,07	0,47	73	0,17	0,42
2	131	0,09	0,46	54	0,23	0,4
3	86	0,15	0,43	38	0,32	0,37
4	41	0,3	0,37	24	0,51	0,3
5	27	0,51	0,3	17	0,72	0,22
6	< 10	> 1	0	< 15	> 1	0

Table 4.1: Values of the critical current and the corresponding parameter k at different temperatures. The critical current has been extracted from magnetization curves as shown in Figure 4.6 by assigning the jump height to one flux quantum (see text). The data is given for a zero- and a π-loop. Φ/Φ_0 is the normalized flux which was obtained from the relation plotted in Figure 2.14 for the corresponding values of k.

and sawtooth), the fraction of one flux quantum which *r*eally corresponds the jump height of the Hall voltage can be extracted. It turns out that the jump height corresponds to $0.75\,\Phi_0$ for a sinusoidal CPR and to $0.81\,\Phi_0$ for a sawtooth CPR. This means, the values of the critical current given in table 4.1 are systematically overestimated by about 19 to 25 % due to the uncertainty of α.

4.3.5 Signature of the π-Junction in the Experimental Data

In Figures 4.7(a), 4.7(b) and 4.8(b), again the Hall signal δV_H is plotted as a function of the applied magnetic field. The linear background has been subtracted, as described in section 4.4(a). In each panel, the upper graph (solid line) corresponds to the 0 loop, the lower graph (dashed line) to the π-loop. The curves have been offset for clarity. The sweeps in both directions have been traced immediately after field cooling and are therefore virgin-curves. This is important because the hysteretic behavior for large LI_C products might result in trapped flux in the loops otherwise. The vertical line denotes the cooling field from which magnetization traces started.

If the magnetization starts close to zero (-1,72 μT in Figure 4.7(a) and 1,72 μT in Figure 4.7(b)), the Hall voltage of the 0-loop (solid) falls or rises monotonically in the vicinity of the starting field. Whether the voltage in- or decreases depends on the sweep direction as the loop tries to screen the applied field. This monotonic in- or decrease is interrupted by a sudden jump if the critical current of the loop is reached. During the jump flux enters the loop and upon further sweeping the

applied flux, the loop again tries to screen the applied flux until the critical current is reached again. This leads to a sequence of jumps of the Hall voltage and results in the observed sawtooth shaped pattern.

This pattern is characteristic for the flux quantization in superconducting loops and is illustrated in Figure 4.8(a), where the total flux through the loop is schematically plotted as a function of the applied flux. This plot represents the graphical solution of equations 2.33 and 2.34. The case of the 0-loop is displayed on the right side of the graph (solid line). The black dots correspond to the cooling fields of the curves presented in Figs. 4.7(a), 4.7(b) and 4.8(b). This $\Phi(\Phi_{applied})$ relation (referred to as flux-plot in the following) is shown for $k < 1$ (eqn. 2.35), therefore the flux-relation of the loop is (partly) multi-valued, what makes the flux-relation hysteretic as only the parts of the curve with positive slope are traced (see Figs. 2.10(a)).

It can be seen in Figure 4.8(a) that it is characteristic for the 0-loop, that the jumps in the Hall voltage occur symmetrically with respect to the cooling field for up- and down-sweeps if the cooling field is close to zero applied flux in the single valued region.

The signature of the π-junction in the loop is found in the position of the jumps of the Hall voltage with respect to the cooling field. For cooling fields close to zero, the jumps in the Hall voltage of the π-loop (dashed lines in figures 4.7(a) and 4.7(b)) are clearly asymmetric with respect to the cooling field. For the cooling field of -1.72 μT, the jump occurs earlier when sweeping the field up ($\sim$10 μT) than for sweeping the field down (at about -50 μT). The position of the jumps for the two sweep directions is reversed by choosing a cooling field of +1.72 μT. For this cooling field the early jump occurs in the down-sweep direction. The explanation is found in 4.8(a): At zero applied field two energetically degenerate states exist for the π-loop, both characterized by a spontaneous circulating current in the loop, which generates the non zero total flux in the loop. The degeneracy is due to the two possible directions for the circulating currents, clockwise or counter-clockwise. The magnetic flux produced by these currents saturates close to $\pm\Phi_0$ for sufficiently high values of LI_C (see Figs. 2.14 and 4.8(a)). In particular, there is no stable state with zero applied flux and zero total flux for the π-loop. By applying a small field of $\pm$1.72 μT during cool-down, the degeneracy is lifted and one of two states is selected. In this way, different branches of the $\Phi(\Phi_{ext})$ relation are selected (Figure 4.8(a)) and cause the observed asymmetry of the jump positions.

In figure 4.8(b) the same type of measurement is shown, but for a cooling field close to the value corresponding to half a flux quantum in the loop. At this cooling field, the π-loop is described by a single-valued branch of the flux-plot, while the flux-plot corresponding to the 0-loop is multi-valued. It is found in Figure 4.8(b) that

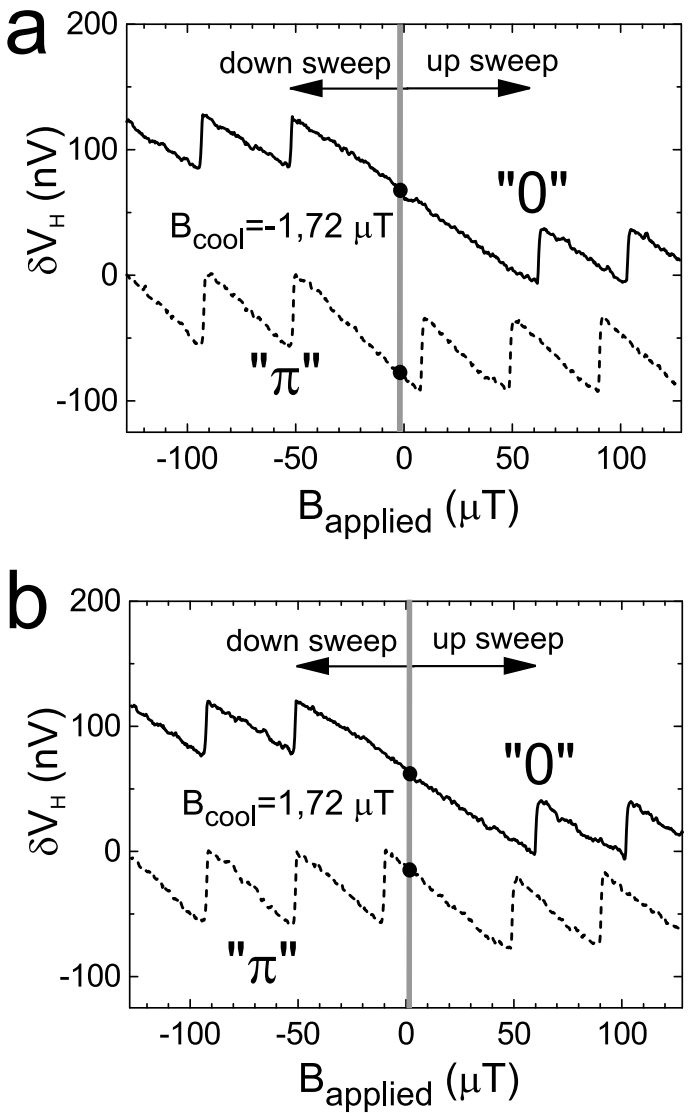

Figure 4.7: Magnetic field sweeps which reveal the character (0 or π) of the junction incorporated in each loop. The data was obtained after field cooling at a temperature of 2 K. The position of the jumps in the measured Hall-voltage contains the important information. (a) and (b) show the magnetization curve starting slightly below and above zero applied field. The jumps of the 0-loop (solid line) are symmetric with respect to the starting field for either curve. The π-loop (dashed line), in contrast, shows clearly asymmetric jumps with respect to the starting field.

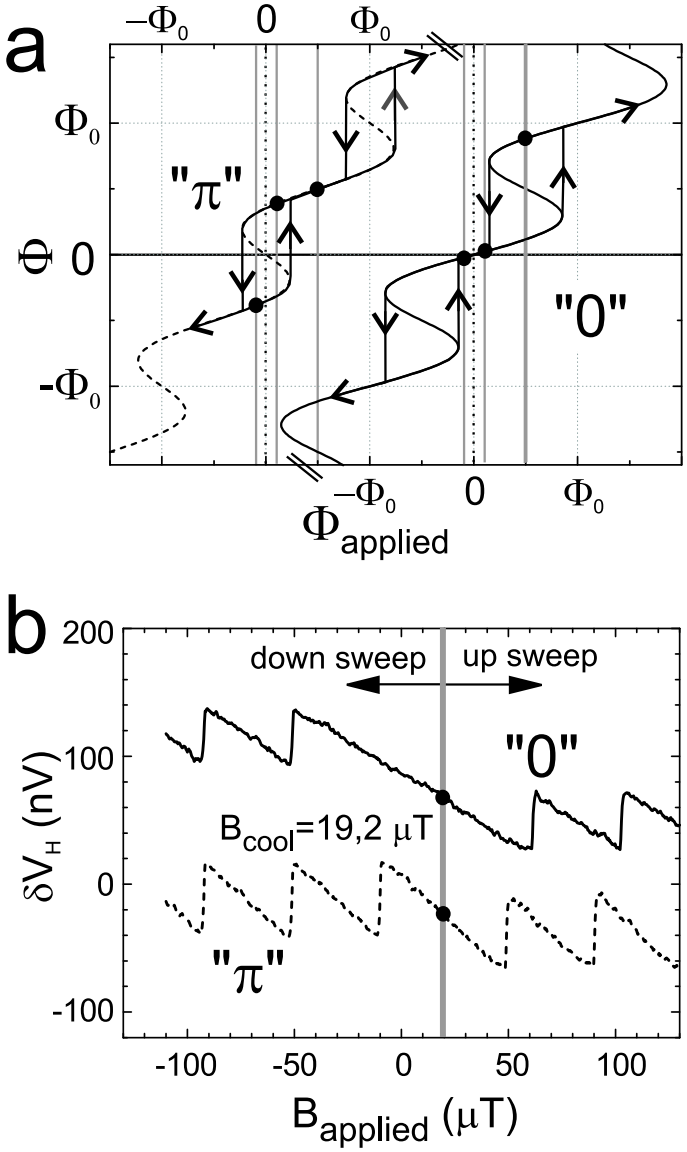

Figure 4.8: The data plotted in Figs. 4.7 and panel (b) is explained by the sketch (a), which shows the dependence of the total flux on the applied flux for a 0- and a π-loop (see text for details). When the cooling field corresponds to half a flux quantum in the loop, as shown in panel (b), the symmetry properties of the two types of loops are exchanged when compared to the data for zero field cooling (Figs. 4.7 (a) and (b)).

the magnetic field sweeps of the π-loop show a symmetric pattern with respect to the cooling field, while the trace produced by the 0-loop shows clearly asymmetric jumps. The symmetry properties are interchanged between 0- and π-loop when compared to cooling fields close to zero. The explanation is, that the 0-loop produces a spontaneous flux to screen the cooling field of about half a flux quantum. Again the two possible directions of the circulating currents are energetically degenerate at a cooling field of exactly half a flux quantum. By applying a cooling field slightly above or below this value, one of the directions can be chosen. The subsequent field sweeps lead to an asymmetric pattern (solid line in Figure 4.8(b)). The π-loop on the other hand produces no magnetic flux upon cool-down in a field equal to half a flux quantum, as this value is compatible with the condition of half integer flux quantum applicable for a π-loop (see section 2.4.3).

4.4 Temperature Sweeps

It was derived in section 2.4.3), that the ground state of a superconducting loop with inserted π-junction is a state with spontaneous circulating current and magnetic flux. The following paragraph describes the first direct experimental observation of this spontaneous magnetic flux in loops with ferromagnetic Josephson junctions.

In order to detect the emergence of this flux, temperature sweeps are performed starting from 10 K, well above T_C, down to 300 mK. While sweeping the temperature, the Hall voltage is monitored to watch the magnetic moment upon cool-down.

The obtained raw data shows a monotonic decrease of the measured (Hall-)voltage with temperature which is much larger than the signal corresponding to the expected spontaneous flux produced by the loop. This dominant decrease is attributed to a decreasing channel resistance of the 2-DEG with temperature, which is reported e.g. in [44] for a 2DEG with similar mobility and carrier concentration to the one used here[4]. Because of the extremely weak impurity scattering in the high quality material a considerable temperature dependence remains even in the range between 1 K and 10 K. This resistance variation is caused by inelastic electron-phonon and electron-electron scattering and depends fortunately only on temperature but is independent of the magnetic field.

It is plausible that the longitudinal resistance is partly measured by the Hall leads: the Hall-crosses are microfabricated using optical lithography and wet etching. Therefore (small) imperfections of the Hall-cross geometry due to edge roughness have to

[4] n=$2.66 \times 10^{15}\,\mathrm{m}^{-2}$, $\mu = 75\,\mathrm{m}^2\mathrm{V}^{-1}\mathrm{s}^{-1}$

be taken into account. But a small asymmetry of the voltage leads, which define the Hall cross is sufficient to mix a fraction of the longitudinal resistance to the Hall-voltage.

This effect is also observed in form of an offset of the Hall-voltage: the Hall voltage is non-zero although the magnetic field through the active area is zero. To be able to benefit from the maximum dynamic range the lock-in amplifiers offer, it is therefore advantageous to compensate this offset. This is accomplished by using a tunable potential divider, which adds a fraction of the driving voltage to the measured Hall-signal. This bridge can be adjusted to compensate the Hall signal to zero in zero applied field. However this is just a static compensation, which works at a given temperature, and is not capable of compensating the temperature dependent offset dynamically during a temperature sweep.

The solution to extract the magnetic signal from the raw data is to subtract two temperature sweep datasets measured at slightly different values of the applied magnetic flux ($\Phi_1 = -\Phi_2$, $\Phi_1 \ll \Phi_0$). As described above, the measured raw-data voltage has two contributions, the Hall signal U_{Hall} which depends on the magnetic flux Φ penetrating the active area and the and the temperature dependent voltage resulting from the longitudinal resistance U_{long}

$$U_{raw}(\Phi, T) = U_{Hall}(\Phi) + U_{long}(T). \tag{4.5}$$

Subtraction of two temperature sweeps at slightly different applied fields cancels the spurious contribution of the longitudinal resistance and leaves only the Hall signal

$$\begin{aligned} U_{diff}(\Phi_1, \Phi_2) &= U_{raw}(\Phi_1, T) - U_{raw}(\Phi_2, T) \\ &= U_{Hall}(\Phi_1) - U_{Hall}(\Phi_2). \end{aligned} \tag{4.6}$$

The measured Hall signal is the sum of the signal resulting from the applied flux Φ_{app} and the flux produced by the loop LI_S. Above the critical temperature LI_S is zero, while at low temperatures possibly an increasing magnetic moment caused by the loop emerges

$$U_{Hall}(\Phi) = U_{Hall}(\Phi_{app}) + U_{Hall}(LI_S). \tag{4.7}$$

If two temperature sweeps are subtracted where the applied flux is chosen e.g. slightly above and below zero the spontaneous flux in the π loop will emerge with opposite sign but equal absolute value due to the symmetry properties of the flux-plot, leading to

$$\begin{aligned} U_{diff}(LI_S) &= U_{Hall}(\Phi_1) + U_{Hall}(LI_S) - (U_{Hall}(\Phi_2) + U_{Hall}(-LI_S)) \\ &= 2 * U_{Hall}(LI_S); \end{aligned} \tag{4.8}$$

here $U_{Hall}(-\Phi) = -U_{Hall}(\Phi)$ was used. As a result, the subtraction isolates the required Hall signal originating from the loop. As shown, to investigate the loop at $\Phi_{app} = 0$ two temperature sweeps measured in $\Phi_1 > 0$ and $\Phi_2 < 0$ have to be subtracted. This measurement method can be extended to arbitrary values of Φ_{app}; in this more general case, the result of the subtraction is again twice the signal from the loop plus an constant offset, which has been removed in the following measurement data.

The data which was obtained by this procedure is plotted in Figures 4.9(a) and 4.9(b). The measurement was done for a 0-loop (black trace) and a π-loop (gray trace) at the same time. The right axis denotes the measured Hall voltage, which is of the order of 20 nV, the left axis converts the voltage into magnetic flux, as described in section 4.3.4.

Figure 4.9(a) shows the results for zero applied flux. The Hall signal corresponding to the 0-loop remains constant over the whole temperature range, because the state with zero total flux and hence zero circulating current is the ground state of a 0-loop in zero applied field. The situation is different for the π-loop: Only in the range from 10 K down to 5 K the signal from the π-loop is constant; but for even lower temperatures, when LI_C becomes larger than $\Phi_0/2\pi$, an increasing magnetic moment which saturates close to half a flux quantum at low temperatures can be detected. This spontaneously generated flux is necessary to fulfill the *half-integer* flux quantization of a π-loop: In zero applied field, the ground state is a state with magnetic flux equal to *half* a flux quantum in the loop, which is produced by circulating currents in the loop.

In Figure 4.9(b) the same measurement is plotted for an applied field equal to half a flux quantum in the loop, which alters the magnetic response of the investigated loops considerably. In this case, the π-loop shows no magnetic signal over the complete investigated temperature range. This is expected, as the applied flux equal to $\Phi_0/2$ satisfies the half-integer flux quantization of the π-loop, no circulating currents are induced upon cool-down. Instead, the 0-loop shows a magnetic response: Below 5.5 K, currents start to circulate in the loop and produce a field equal to half a flux quantum, which either adds up with the applied field to one flux quantum, or cancels the applied field flux to zero, according to the integer flux quantization applicable for 0-loops.

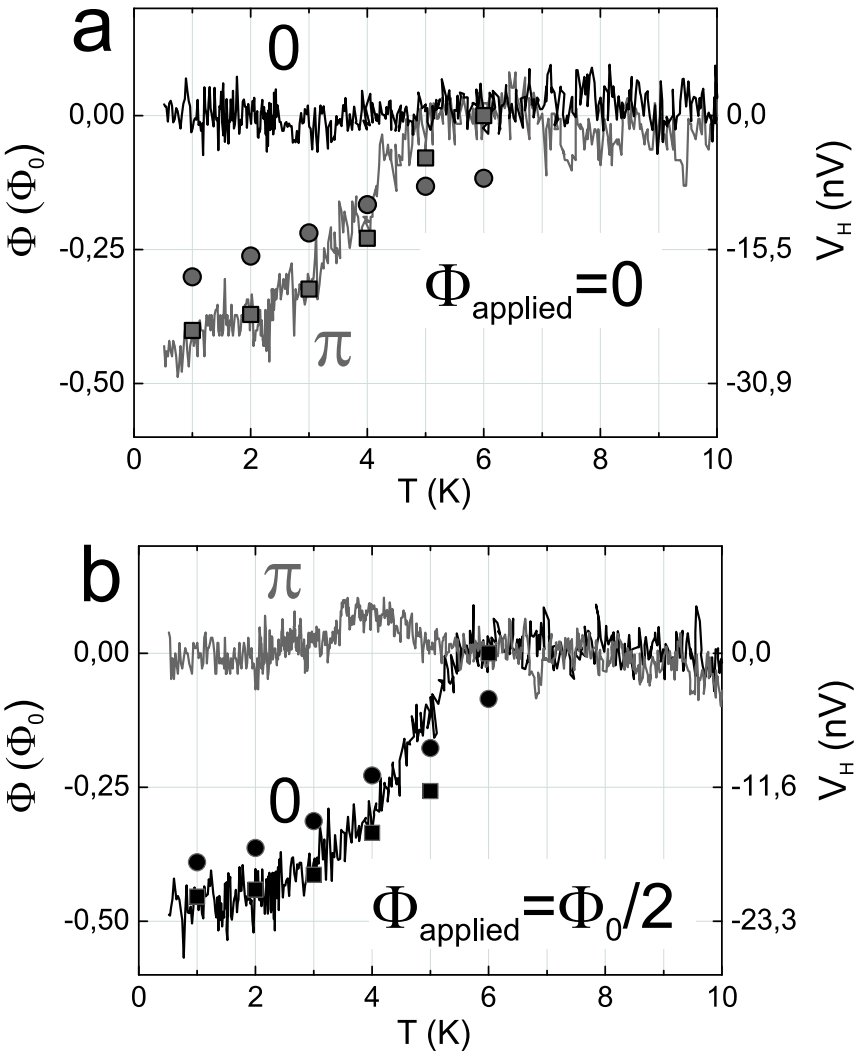

Figure 4.9: By sweeping the temperature, the emergence of the spontaneous magnetic flux can be observed. (a) When cooling down the π-loop below T_C in zero applied field, a spontaneous current develops which leads, together with the loop's inductance, to a magnetic flux (gray trace). The flux is detected by the micro-Hall sensor and saturates close to $\Phi_0/2$ for low temperatures. The 0-loop, in contrast, shows no magnetic signal upon cooling down (black trace). (b) The same measurement but in an applied flux equal to half a flux quantum. In this case, there is no magnetic response of the π-loop over the whole temperature range (gray trace), whereas the 0-loop develops circulating currents to compensate the applied flux and therefore fulfills the condition of integer flux quantization (black trace). The dots in both panels mark the value of the magnetic signal as expected from the estimation of the critical current (see table 4.1), assuming a sinusoidal (squares) and sawtooth (circles) CPR.

The dots in Figures 4.9(a) and 4.9(b) represent the values of the produced flux expected for the values of the critical current (section 4.3.4) given in table 4.1. The expected flux has been calculated by converting the LI_C product at different temperatures in k-values (equation 2.35), and translate these into magnetic flux, using the relations plotted in Figure 2.14. The squares show the flux calculated for an assumed sinusoidal CPR, the circles for a sawtooth CPR. The assumption of a sinusoidal CPR seems to describe the measured data better, especially in the temperature range below 4 K a good fit is obtained.

4.5 Junctions close to the 0-π Crossover

The thickness of the magnetic coupling layer for the samples discussed in this section is adjusted to the crossover between 0- and π-coupling (see Figure 2.8). At this point, the critical current is strongly reduced, and the CPR is expected to be periodic in $\Phi_0/2$, as compared to Φ_0 in the usual case [23, 30, 59]. The measurements were motivated by the search for a change in frequency of the jump pattern obtained by sweeping the magnetic field. The curves which are presented indeed show an interesting change in the periodic sawtooth pattern during magnetic field sweeps but, to come to the point, so far lack a plausible explanation. The loops from which these measurements were obtained have Josephson junctions which consist to one part of a junction with magnetic interlayer and to another part of a junction without magnetic interlayer.

4.5.1 Double Junction Loops

For the shadow evaporation, the mask height is an important parameter. Together with the tilt angle it determines the translation of the evaporated pattern on the sample surface (see Figure 3.10). To improve the success rate, during each time-consuming evaporation session[5] not only a single Hall-bar, but a batch of several identical mesas was evaporated at a time. Because the mask height varies slightly between the edge and the center of the chip (due to edge effects during spinning of the relatively small chips of typically 4 mm × 5 mm), the adjusted tilt angle is never ideal for all mesas on the chip at the same time. As a consequence, a mismatch of mask height and tilt angle results in a mismatch of the evaporated metal layers on the chip (see section 3.3). This led to Josephson-junctions, which consist to one part of a SFS junction with magnetic coupling layer and to another part of a plain

[5] each session required one transfer to and back from Orsay

Nb-Nb superconducting short circuit without magnetic interlayer, but possibly with some kind of barrier gettered by the bare Nb electrode during the PdNi deposition.

In Figure 4.10 these type of Josephson junction are schematically sketched. If the ferromagnetic part of the Josephson junction would be in the π-state, spontaneous half-integer flux quanta (semi-fluxons) would be expected to appear at the border between the 0- and the π-part of the junction [57, 58]. If semi-fluxons were present, they would probably reduce the critical current of the junctions. Further effects the semi-fluxons might have on the measurements presented here are not clear.

In the right panel of Figure 4.10 two possible paths for the supercurrent to flow across the junction are indicated. If the *double junction* is considered as a whole, the question arises to what amount the different parts of the junction contribute to the total supercurrent. The critical currents of both parts can be obtained by multiplying the area of the junctions with the ratio of the critical current densities j_c^0 and j_c^π (see section 4.3.4). But the value of j_c^π found there can not really be applied here, because in these samples, the thickness of the magnetic interlayer is adjusted such that the junction with magnetic interlayer is close to the transition point between 0- and π-behavior (marked by the arrow in Figure 2.8, [5]). The thickness d_F of the ferromagnetic layer is 7.5 nm, the Ni concentration is 9 % and the thickness of the Nb electrodes is 40 nm. At this point, the critical current of the SFS junctions is expected to be especially low and the CPR is expected to have a $\Phi_0/2$ periodicity [23].

At first glance it seems reasonable to assume that the total supercurrent across the structure is dominated by the plain S-S junction, if the area of the magnetic part of the junction is not much bigger than the area of the S-S part. Therefore it could be assumed that the behavior of such a *double junctions loop* is similar to that of a superconducting loop with only one plain Nb-Nb junction. However, the phenomena described below indicate that in some cases effects from the mixed character of the junctions are present.

4.5.2 Example I

A SEM picture of such a junction is shown in Figure 4.11. The (dark) Nb top electrode covers not only the (bright) magnetic coupling layer (as intended), but also makes a "superconducting short circuit" to the bottom Nb electrode. The resulting structure is a superconducting loop interrupted by two parallel Josephson junctions of different critical current densities. A weak link in the part of the junction without ferromagnetic layer might be formed by adsorbates on the bottom Nb electrode

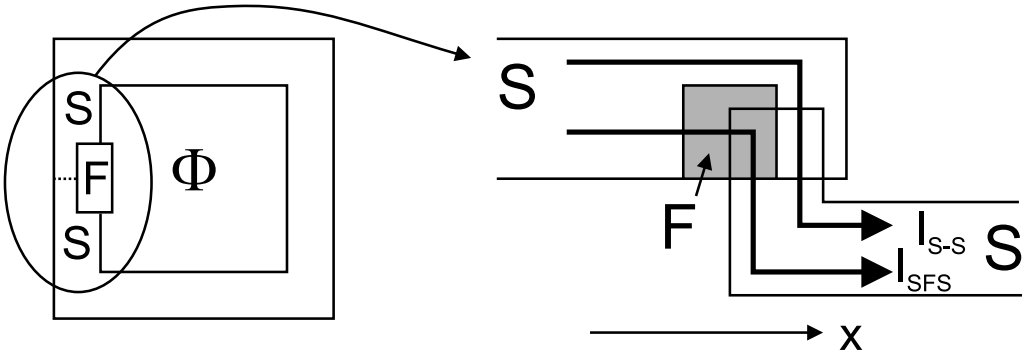

Figure 4.10: Schematic representation of a *double junction loop*, a superconducting loop interrupted by two Josephson junctions in parallel (left). The right panel shows a detailed schematic of the junction area. Two current paths with supercurrents j_S and j_F are possible; they correspond to a supercurrent flowing across the junction with and without ferromagnetic coupling layer.

(S-S), which are deposited from the residual gases in the chamber during the evaporation of the PdNi layer. Close to the loop, there are some residues of the PES/Ge mask with Nb and PdNi on top, which could not be removed by the lift-off (outside the visual field of the SEM picture 4.11). The ratio of the area with (A_F) and without (A_S) magnetic interlayer can be estimated from the SEM picture and is about $A_F : A_S = 3.6 : 1$. If a ratio of the current density from Figure 4.6(f) is considered $j_F : j_S \approx 1 : 3$ (at 3K), it turns out that the two junctions in parallel would have roughly the same critical current $I_c^F : I_c^S \approx 1.2 : 1$. However, if the ferromagnetic junction has a thickness close to the transition point between 0 and π, as intended, the critical current density of this π-junctions is expected to be reduced, and the plain S-S junction would dominate again.

A typical measured curve obtained from this sample is shown in Figure 4.12(a). When performing a complete magnetization cycle, the expected hysteretic magnetization trace is obtained. The measurement was done at 3 K.

The first interesting observation is, that in this measurement additional jumps of the Hall voltage are found during the part of the trace after reversal of the sweep direction. This might be due to the contribution to the signal coming from two junctions with different critical currents. While the overall hysteretic opening would then be given by the junction with the larger critical current, the jumps in the linear part after sweep direction reversal might result from the junction with the smaller critical current. The latter junction might produce a sawtooth pattern which is added to the trace of the other junction.

The second interesting feature is the occurrence of parts in the sawtooth shaped magnetization trace, where the frequency of the Hall voltage jumps changes. For

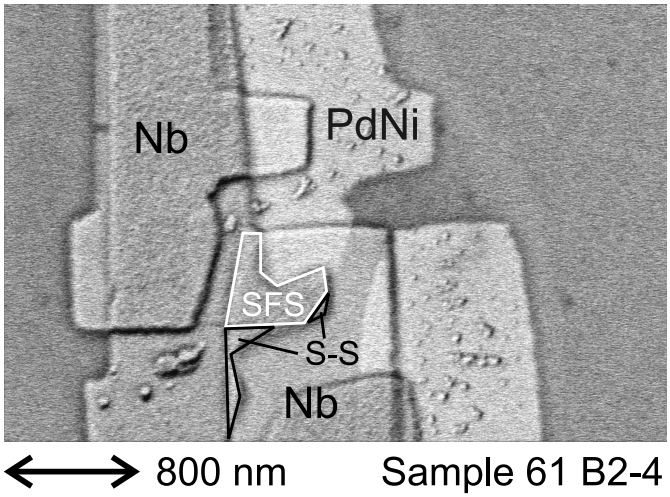

Figure 4.11: SEM picture of a double junction. The area enclosed in the white frame and labeled SFS is the part of the junction with ferromagnetic coupling layer. The areas in the black frame are the parts of the junction without ferromagnetic interlayer. The ferromagnetic part of the junction has an area about 3.6 times larger than the part without ferromagnetic layer.

example, in Figure 4.12(a) in the upsweep part of the curve, starting at a field of about $250\,\mu$T the Φ_0 periodic pattern first shows small additional peaks, then the frequency is doubled while the amplitude is bisected at about $400\,\mu$T, and finally, upon further increasing the applied field, frequency and amplitude recover their initial values. In the down-sweep part of the trace, similar structures are found at negative values of the applied field.

Figure 4.13 shows the same measurement as Figure 4.12(a), but extended to larger values of the applied field ($\pm 2.5\,$mT). The measurement was taken at 500 mK. It can be seen, that the change in the periodicity of the jump pattern (indicated by arrows) appears and disappears upon sweeping the applied field twice in each sweep direction. The feature seems not to appear periodically, as might be expected from a beating pattern, as can be seen in Figure 4.13. In each sweep direction, a third possible appearance is missing, indicated by an question mark.

The field B^*, at which this frequency change is observed in Figure 4.12(a), is plotted in Figure 4.14 as a function of temperature for the up- and the down-sweep direction. For low temperatures the values of B^* are close to zero magnetic field. With increasing temperature, the crossover fields evolve towards higher values.

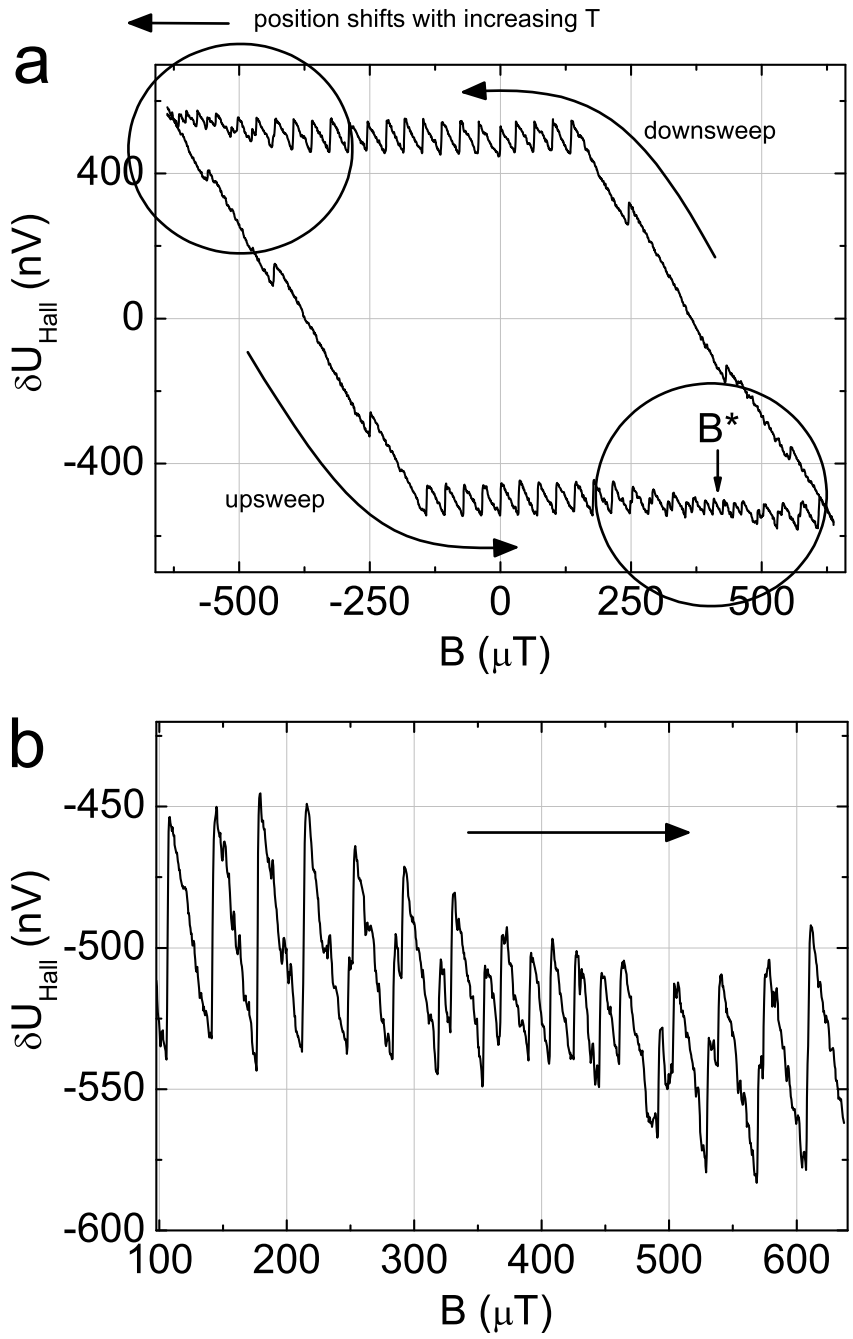

Figure 4.12: Magnetization trace obtained from the double junction loop shown in Figure 4.11 measured at 3K. The curve shows additional steps in the part of the sweep after reversing the sweep direction. The circles highlight the areas of the curve where the sawtooth pattern, resulting from the flux quantization, temporarily changes to the doubled frequency. Panel (b) shows this part of the curve in more detail.

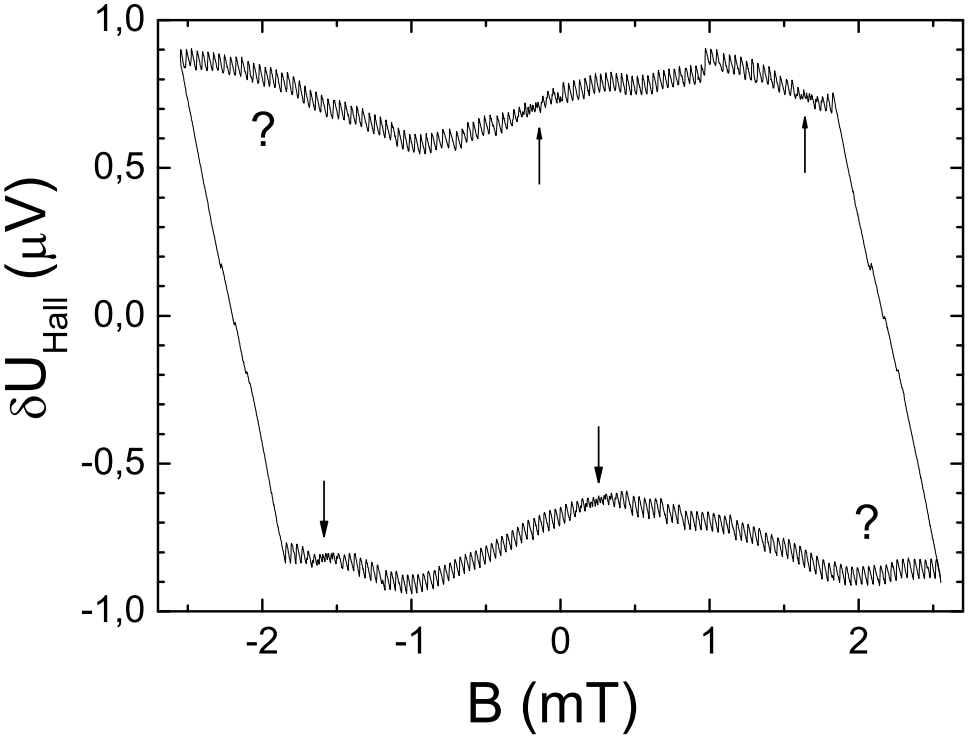

Figure 4.13: Magnetic field sweep over an extended range (± 2.5 mT), measured at 500 mK. The arrows indicate the position of the appearance of the frequency doubling in the switching pattern. As can be seen, the feature appears twice in each sweep direction. The question-marks indicate the position at which one might expect a third appearance if a beating effect would be assumed, which is absent.

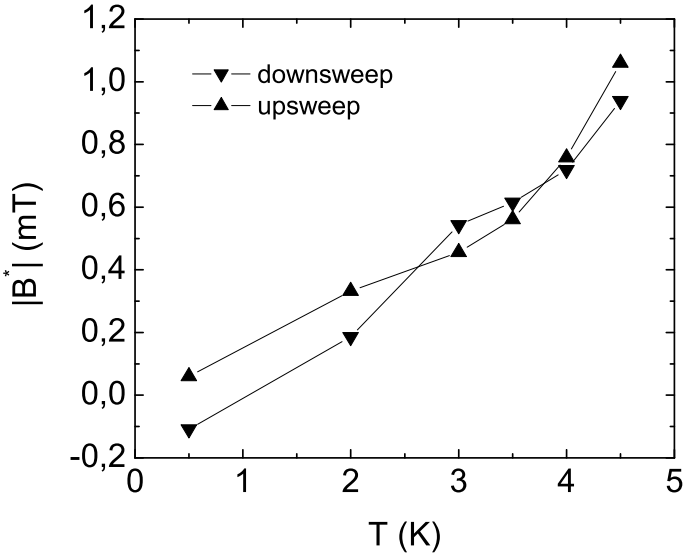

Figure 4.14: Temperature dependence of the absolute value of the magnetic field B* at which the frequency changes appear in the magnetic field sweeps of the double junction loops. The symbols correspond to the up- and downsweep.

4.5.3 Example II

An other example of a double junction loop is shown in the SEM picture 4.15. The ratio of the areas of the two parts of the junction is about $A_F : A_S = 1 : 2$. Together with the assumption that the critical current of the part without ferromagnetic interlayer is (much) bigger, the total critical current of this double junction should be dominated by the S-S part.

Curves obtained form this loop are plotted in Figures 4.16(b) and 4.16(a). The temperature is 2 K, the sensor current is 5 μA. The complete magnetization cycle plotted in Figure 4.16(a) is not fully closed due to the magnetic previous history of the loop prior to this measurement. Figure 4.16(b) shows only a small part of the complete magnetization cycle shown in Figure 4.16(a). The sawtooth pattern in the Hall signal shows an exact doubling of the frequency, which is expected for a ferromagnetic Josephson junction close to the transition point between the 0- and the π-state (see section 2.3.3) . This observation is certainly in contradiction to the statement above, that the contribution from the SFS junction can be neglected.

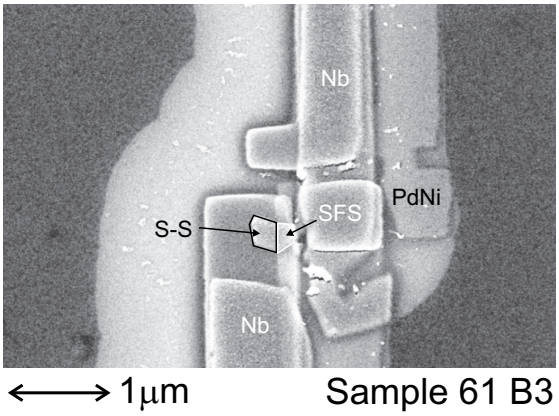

Figure 4.15: SEM picture of the second example of a double junction loop. The corresponding measurements are shown in Figures 4.16(b) and 4.16(a). The ratio of the areas of the two types of junctions is roughly $A_F : A_S = 1 : 2$, which means that the behavior of this loop should be dominated by the plain S-S junction (without magnetic interlayer).

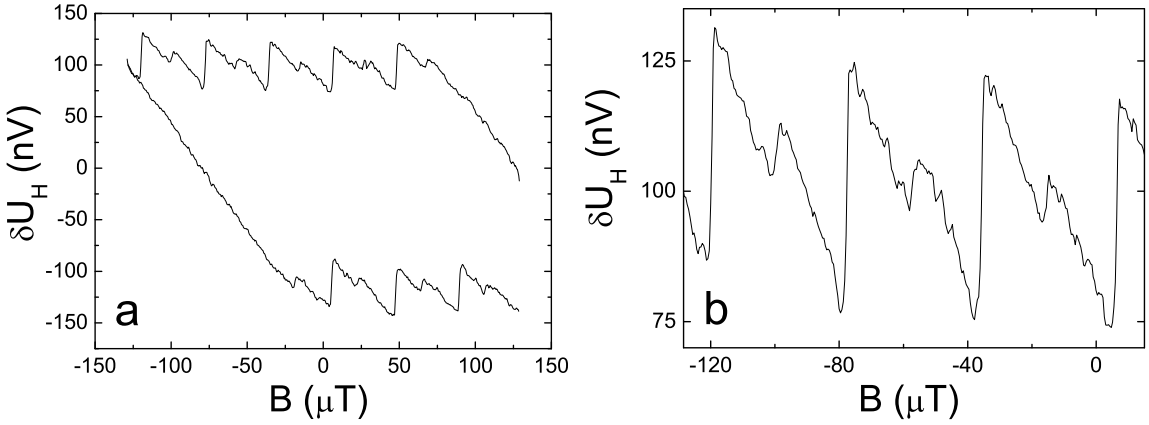

Figure 4.16: (a) The trace was obtained from the sample shown in 4.15 and shows jumps of the Hall voltage with a frequency corresponding to half a flux quantum. The curve is not closed due to the magnetic previous history. Panel (b) shows a part of the trace in detail. The measurement temperature is 2 K, the driving current for the Hall sensor is 5 μA.

4.5.4 Discussion

Shown above are some examples of measurements obtained from samples which contain two Josephson junctions in parallel, one without and one with ferromagnetic coupling layer. The samples were initially intended to examine the behavior of a ferromagnetic Josephson junction close to the 0-π transition. Therefore the thickness of the ferromagnetic layer is adequately adjusted, which is expected to result in a especially low critical current of the ferromagnetic part of the junction.

The main features of these measurements are summarized below:

- The sawtooth pattern defined by the jumps of the Hall voltage measured when sweeping the magnetic field changes its periodicity when sweeping the applied field.
- For some values of the magnetic field B^*, this jump pattern exactly doubles its frequency.
- The magnetic fields B* for the behavior described above is temperature dependent.
- The change in frequency of the switching pattern is observed twice in each sweep direction, if the range of the applied magnetic field is large enough.
- The monotonic in-/decrease of the circulating current when reversing the sweep direction is superimposed by additional jumps.

As the two junctions are incorporated into the same superconducting loop they should both be biased by the same phase difference φ. The exact current distribution in the area of two junctions might result in a more complicated behavior. To model the observed features, the two contributions to the supercurrent $I_{SFS}(\varphi)$ and $I_{S-S}(\varphi)$, resulting from the two junctions with and without magnetic interlayer have to be combined. The ratio of the critical currents of the two junctions depends on the ratio of the junction areas and critical current densities. The total supercurrent would then be given by the sum of both contributions.

The ratio of the junction areas can be measured from the SEM pictures, and the current density of the S-S junction was estimated in section 4.3.4. However the critical current density of the ferromagnetic junction close to the 0-π transition point is not known, but expected to be very low.

Another issue which makes the modeling difficult is the unknown shape of the CPRs of both junctions. Both might be assumed sinusoidal

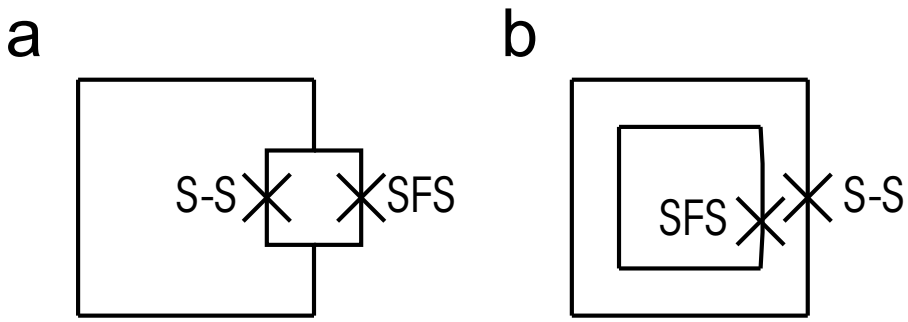

Figure 4.17: Two possible equivalent circuit diagrams to model the double junction loop. (a) The S-S and the SFS junction are incorporated in parallel into one common superconducting loop. This picture seems to be more realistic than the one plotted in (b): The two junctions are treated as if they were embedded into impendent superconducting loops.

$$I_{S-S}(\Phi) = I_C^{S-S} \sin\left(2\pi \frac{\Phi_{S-S}}{\Phi_0}\right) \tag{4.9}$$

$$I_{SFS}(\Phi) = I_C^{SFS} \sin\left(2\pi \frac{\Phi_{SFS}}{\Phi_0} + \pi\right). \tag{4.10}$$

Two possibly different effective loop diameters for the two parts of the junction would result in two different values of the applied flux for a given applied flux density B. This is taken into account by two different values of the total flux for both junctions Φ_{S-S} and Φ_{SFS} above.

Figure 4.17 shows two possible equivalent circuit diagrams for the double junction loops. In panel (a) they are connected in parallel and included in a superconducting loop. In panel (b), both junctions are treated as if they were incorporated into independent loops of similar diameter.

Two possible fluxplots generated with these assumptions are shown in Figure 4.18. The plot labeled (a) corresponds to the equivalent circuit (a) in 4.17. In this case, the S-S junctions is modelled by a conventional sinusoidal CPR (equation 4.9), whereas the SFS junction is assumed to have a $\sin(2\pi\frac{2\Phi_{app.}}{\Phi_0})$ dependence on the applied flux (see equation 4.10). As can be seen, the derived jump pattern seems not to be characterized by the 2Φ-periodic contribution.

The flux-plot in panel (b) shows two independent flux-plots (corresponding to the equivalent circuit (b) in Figure 4.17), both CPRs are assumed conventional (equation 4.9). Two different diameters of the loops were assumed. The resulting jump pattern

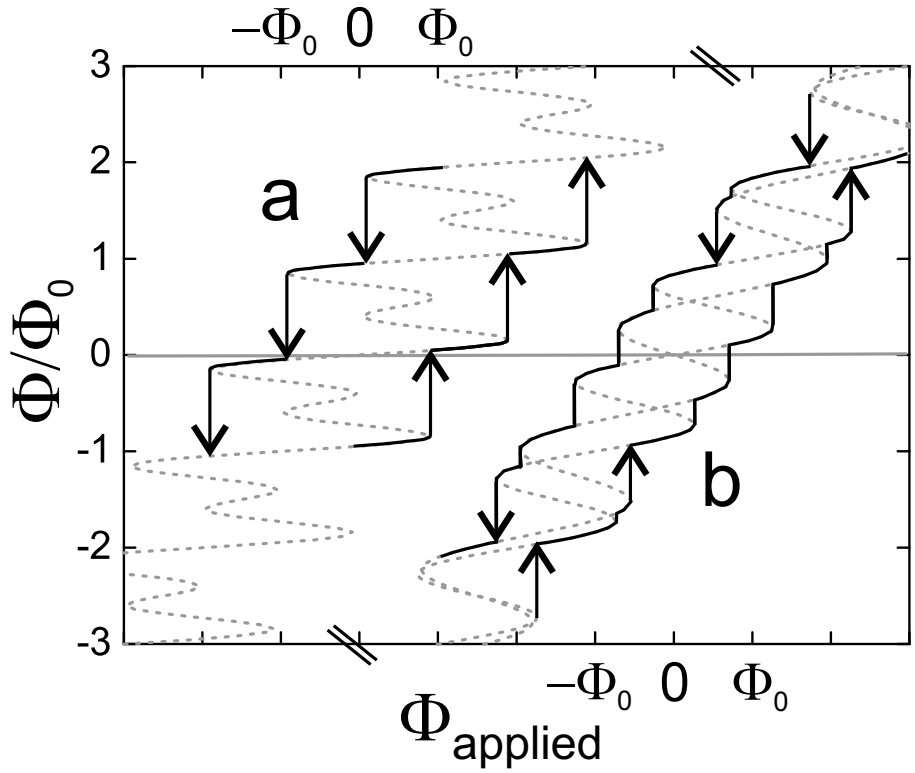

Figure 4.18: flux-plots for the two different equivalent circuit diagrams described in Figure 4.17.

shows additional jumps when compared to fluxplot (a). However, the treatment of the system as two independent loops seems not to be justified.

The temperature dependence of the observed features might by taken into account by considering that temperature alters the current distribution along the cross section of the double junction due to the temperature dependent magnetic penetration depth.

The assumptions made above are problematic and explain the observed data only partly. It is probably not justified to consider both parts of the junction as two independent loops. Furthermore, only some of the examined loops with two junctions in parallel show the characteristic features discussed in this section, some others behave as if they had only one 0-junction, which seems more plausible. Also the influence of lift-off remains, which is present close to the loops discussed in this section, is not clear. Therefore the conclusion is that the curves discussed in this section are not understood, although they show interesting features.

Chapter 5

Summary and Outlook

In the present work the magnetic moment of superconducting loops with integrated ferromagnetic Josephson junctions are investigated by means of micro-Hall magnetometry.

The superconducting loops are made of Nb, the ferromagnetic weak links are realized by the diluted ferromagnet PdNi. To get clean interfaces, the technique of shadow evaporation is applied. A mask system which is capable of e-gun shadow evaporation of Nb had to be chosen. Therefore several different material systems were tested. The shadow masks which are finally used successfully in these experiments are made of the high temperature stable plastic polyethersulfone (PES) as sacrificial layer and of Ge, which is used as mask-layer. The mask layer is structured by e-beam lithography and dry etching. The individual Nb loops with PdNi Josephson junction are placed onto the active area of micro Hall-sensors. These sensors are fabricated from a modulation doped GaAs/AlGaAs heterostructure which was provided by Prof. Dr. W. Wegscheider in Regensburg. The shadow evaporation of the loops was done by Dr. M. Aprili in Orsay/Paris.

By sweeping the applied magnetic field and measuring the magnetic response of the loop at low temperatures, a hysteretic switching pattern, which is typical for a superconducting loop with integrated Josephson junction, is observed. From the symmetry properties of this switching pattern, evidence for the π character of the ferromagnetic junctions is found.

The main result is the detection of the spontaneous magnetic flux produced by a superconducting loop interrupted by a ferromagnetic π-junction upon cooling down below the superconductors critical temperature in zero field. The emergence of the spontaneous flux, which saturates close to half a flux quantum at low temperatures, is seen in the Hall voltage while the reference loop with a 0-junction shows no

magnetic signal during the same temperature sweep. If the experiment is repeated with an applied flux equal to half a flux quantum, the 0-loop develops magnetic flux in order to compensate the applied flux, whereas the π-loop shows no response. This can be explained by the integer and half-integer flux quantization which is applicable for superconducting loops with integrated 0- and π-junctions, respectively.

In the last stage, ferromagnetic junctions close to the transition point between the 0- and the π-state are fabricated in order to search for the expected $\Phi_0/2$ periodic current phase relation [23, 30, 59]. The results on these loops are not conclusive although some change in the flux-quantization pattern is observed. Further investigation of this regime, where the junction is close to the transition between the 0- and π-state, and the search for the frequency doubling by means of micro-Hall magnetometry is certainly interesting.

Appendix A

Collection of Recipes

Collection of recipes

Fabrication of Hall-sensors

Wafer cleaving

- Basic material: GaAs/AlGaAs wafer #C021009C
- Cleaning in acetone/ultrasonic and isopropyl alcohol
- Spinning of AR-P 3740, 1500 rpm, 30 s as protection layer
- Cleaving of the wafer in 5 x 6 mm chips

Mesa Etching

- Cleaning in acetone/ultrasonic and isopropyl alcohol
- Spinning of Shipley S-1800 resist at 4500 rpm for 30 s
- *pre-bake* hotplate 90°C for 2 min.
- Exposure of mesa structure for 11 s at 275 W
- Development for 40 s in Microposit Developer : H_2O (1:4)
- Stopping for 15 s in H_2O
- *post-bake* Hotplate 110°C for 2 min.
- Dektak: resist height 430 nm

- HCl-Dip 30 s HCl:H_2O (1:1)
- Wet etching for 30 s in acetic acid : H_2O_2 : H_2O (5:1:5)
- Dektak: step height after etching 658 nm (resist and GaAs)
- Stripping in acetone and isopropyl alcohol
- Dektak: etched step height 240 nm

Ohmic Contacts to the 2DEG

- Cleaning in acetone and isopropyl alcohol
- Spinning of AR-P 3740 resist at 3000 rpm for 5 s (Acceleration 0) and 6000 rpm for 30 s (Acceleration 0)
- *pre-bake* Hotplate 90°C for 6 min.
- Exposure of Au/Ge contacts for 30 s at 275 W
- Development for 40 s in NaOH: H_2O (1:3)
- Stopping for 20 s in H_2O
- O_2-Plasma for 5 s, Power 30%, to remove residual resist
- Metallization at a background pressure of 9×10^{-6} mbar
  $Au_{0.88}Ge_{0.12}$ 210 nm, Ni 52.5 nm
- Lift-off in acetone
- Annealing oven
  Step 1 350° C 120 s type II (forming gas)
  Step 2 450° C 50 s type II (forming gas)
  Step 3 50° C 2 s type III (gas flow)

Bonding Pads

- Cleaning in acetone and isopropyl alcohol
- Spinning of AR-P 3740 resist at 3000 rpm for 5 s (acceleration 0) and 6000 rpm for 30 s (acceleration 0)
- *pre-bake* Hotplate 90°C for 6 min.
- Exposure of metallization pads for 30 s at 275 W

- Development for 40 s in NaOH: H_2O (1:3)
- Stopping for 20 s in H_2O
- Dektak: resist height 935 nm
- Metallization at a background pressure of 5×10^{-6} mbar
  Cr 10 nm (adhesion layer), Au 200 nm
- Lift-off in acetone

Preparation of 20% PES solution

- Drying of Ultrason E 2020 P (BASF) flakes at 200° C for 24 h
- Dissolving of 2 g Ultrason in 10 ml n-methyl-2-pyrollidone (NMP) at 60° C and agitation with magnetic stir bar in a closed jar
- Absorbtion by syringe
- Attachment of teflon filter (0.2 μm) to syringe

Trilayer PES mask

- Purging of resist spinner with nitrogen during the whole process
- Humidity should be kept below 18 % during the whole process
- Put some drops of PES by syringe through Teflon filter (0.2 μm) on the sample; the chip should by completely covered by PES
- Spinning of PES at 3000 rpm for 5 minutes (acceleration 9)
- Hotplate 275° C for 1 minute
- The PES layer thickness for these parameters should be around 750 nm
- **The samples should be stored dry and under vacuum from now on**
- Evaporation of Ge 70 nm at 5×10^{-7} mbar
  alternatively: deposition of Si_3N_4 in Oxford Plasmalab 80+ PECVD, SiH_4 1000 sccm and NH_3 20 sccm, 20 W, 650 mTorr at 275° C for 4 min. (about 60 nm)
- Spinning of PMMA 950k 4% 3000 rpm for 5 s (acceleration 0), 8000 rpm for 30 s (acceleration 9)
- Hotplate 150° C for 6 min.

E-beam Lithography and Structuring of PES/Ge mask

- E-beam lithography (Topcon SM 510): dose 240 μC/cm^2, spotsize 4, magnification 5000x, pre-exposure during realignment at 250x, 2500x and 5000x
- Development 7 s in 2-Ethoxy-ethyl-alcohol: Methanol (6 ml : 14 ml), 10 s in Methanol and 30 s stopping in isopropyl alcohol
- Reactive ion etching of Ge in Oxford Plasmalab 80+: $SiCl_4$ 30 sccm, 25 mTorr, 100 W, 65 s
  alternatively (Si_3N_4-mask): Reactive ion etching of Si_3N_4 in Oxford Plasmalab 80+: CHF_3 50 sccm, O_2 5 sccm, 30 mTorr, 150 W, 60 s
- Isotropic reactive ion etching of PMMA and PES (undercut) in Oxford Plasmalab 80+: O_2 20 sccm, 300 mTorr, 50 W, 30 min
- Dektak: measurement of mask height for shadow evaporation

Lift-off

- 10 min in n-methyl-2-pyrollidone (NMP) at 50° C, if necessary weak ultrasonic bath
- Cleaving of the chip to separate the individual Hall-bars
- Cleaning in acetone/ultrasonic and isopropyl alcohol

Bibliography

[1] L. N. Bulaevskii, V. V. Kuzii, and A. A. Sobyanin. Superconducting system with weak coupling to the current in the ground state. *JETP Lett.*, 25:290–294, 1977. [Pis'ma Zh. Eksp. Teor. Fiz. **25**, 314].

[2] C. C. Tsuei, J. R. Kirtley, C. C. Chi, Lock See Yu-Jahnes, A. Gupta, T. Shaw, J. Z. Sun, and M. B. Ketchen. Pairing symmetry and flux quantization in a tricrystal superconducting ring of $YBa_2Cu_3O_{7-delta}$. *Phys. Rev. Lett.*, 73:593–96, 1994.

[3] J. R. Kirtley, C. C. Tsuei, J. Z. Sun, C. C. Chi, Lock See Yu-Jahnes, A. Gupta, M. Rupp, and M. B. Ketchen. Symmetry of the order parameter in the high-tc superconductor ybacuo. *Nature*, 373:225–8, 1995.

[4] J. A. Baselmans, B. J. van Wees, and T. M. Klapwijk. Direct demonstration of circulating currents in a controllable π-squid generated by a 0 to π transition of the weak links. *Phys. Rev. B*, 65:224513, 2002.

[5] T. Kontos, M. Aprili, J. Lesueur, F. Genet, B. Stephanidis, and R. Boursier. Josephson junction through a thin ferromagnetic layer: Negative coupling. *Phys. Rev. Lett.*, 89:137007, 2002.

[6] W. Guichard et al. Phase sensitive experiments in ferromagnetic-based josephson junctions. *Phys. Rev. Lett.*, 90:167001, 2003.

[7] A. Bauer, J. Bentner, M. Aprili, M. L. Della Rocca, M. Reinwald, W. Wegscheider, and C. Strunk. Spontaneous supercurrent induced by ferromagnetic pi junctions. *Phys. Rev. Lett.*, 92:217001, 2004.

[8] W. Buckel and R. Kleiner. *Supraleitung.* Wiley-VCH, Weinheim, 2004.

[9] M. Tinkham. *Introduction to superconductivity.* McGraw-Hill, New York, 1996.

[10] T. Schaepers. *Superconductor/Semiconductor Junctions.* Springer-Verlag, Berlin, 2001.

[11] P. DeGennes. *Superconductivity of Metals and Alloys*. W.A. Benjamin Inc., New York, 1966.

[12] K. D. Usadel. Generalized diffusion equation for superconducting alloys. *Phys. Rev. Lett.*, 25:507, 1970.

[13] A. A. Golubov, M. Yu. Kupriyanov, and E. Il'ichev. The current-phase relation in Josephson junctions. *Rev. Mod. Phys.*, 76:411–461, 2004.

[14] A. K. Gupta, L. Crtinon, N. Moussy, B. Pannetier, and H. Courtois. Anomalous density of states in a metallic film in proximity with a superconductor. *Phys. Rev. B*, 69:104514, 2004.

[15] B. Pannetier and H. Courtois. Andreev reflection and proximity effect. *Journal of Low Temp. Phys.*, 118:599, 2000.

[16] E. A. Demler, G. B. Arnold, and M. R. Beasley. Superconducting proximity effects in magnetic metals. *Phys. Rev. B*, 55:15174, 1997.

[17] R. Fazio and C. Lucheroni. Local density of states in superconductor-ferromagnetic hybrid systems. *Europhys. Lett.*, 45:707, 1999.

[18] M. Aprili, personal communication.

[19] A. I. Buzdin and M. Yu. Kupriyanov. Josephson junction with a ferromagnetic layer. *JETP Lett.*, 53:321, 1991. [Pis'ma Zh. Eksp. Teor. Fiz. **53**, 308].

[20] Z. Radovic., M. Ledvij, L. Dobrosavljevic-Grujic, A. I. Buzdin, and J. R. Clem. Transition temperatures of superconductor-ferromagnet superlattices. *Phys. Rev. B*, 44:759, 1991.

[21] F. S. Bergeret, A. F. Volkov, and K. B. Efetov. Local density of states in superconductor-strong ferromagnet structures. *Phys. Rev. B*, 65:134505, 2002.

[22] B. D. Josephson. Possible new effects in superconductive tunneling. *Phys. Lett.*, 1:251–3, 1962.

[23] H. Sellier, C. Baraduc, F. Lefloch, and R. Calemczuk. Half-integer shapiro steps at the 0-π crossover of a ferromagnetic josephson junction. *Phys. Rev. Lett.*, 92:257005, 2004.

[24] H. Sellier, C. Baraduc, F. Lefloch, and R. Calemczuk. Temperature-induced crossover between 0 and pi states in S/F/S junctions. *Phys. Rev. B*, 68:54531, 2003.

[25] J. Bentner. *Zur Strom-Phasen-Relation diffusiver Supraleiter/Normalleiter /Supraleiter Josephson-Kontakte*. PhD thesis, Universität Regensburg, 2004.

[26] V. V. Ryazanov, V. A. Oboznov, A. Yu. Rusanov, A. V. Veretennikov, A. A. Golubov, and J. Aarts. Coupling of two superconductors through a ferromagnet: evidence for a π junction. *Phys. Rev. Lett.*, 86:2427–30, 2001.

[27] A. A. Golubov, M. Yu. Kupriyanov, and Ya. V. Fominov. Nonsinusoidal current-phase relation in sfs josephson junctions. *JETP Lett.*, 75:588, 2002.

[28] N.M. Chtchelkatchev, W. Belzig, Yu. V. Nazarov, and C. Bruder. pi-0 transition in superconductor-ferromagnet-superconductor junctions. *JETP Letters*, 74:323, 2001.

[29] Z. Radovic., N. Lazarides, and N. Flytzanis. Josephson effect in double-barrier superconductor-ferromagnet junctions. *Phys. Rev. B*, 68:014501, 2003.

[30] S. M. Frolov, D. J. Van Harlingen, V. A. Oboznov, V. V. Bolginov, and V. V. Ryazanov. Measurement of the current-phase relation of sfs pi-josephson junction. *cond-mat*, page 0402434, 2004.

[31] J. J. A. Baselmans, A. F. Morpurgo, and T. M. Van Wees, B. J. and. Klapwijk. Reversing the direction of the supercurrent in a controllable josephson junction. *Nature*, 397:43–45, 1999.

[32] S. Backhaus, S. Pereverzev, R. W. Simmonds, A. Loshak, J. C. Davis, and R. E. Packard. Discovery of a metastable π-state in a superfluid ^{3}He weak link. *Nature*, 392:687–90, 1998.

[33] A. Barone and G. Paterno. *Physics and applications of the Josephson effect*. Wiley, New York, 1982.

[34] A. H. Silver and J. E. Zimmerman. Quantum states and transitions in weakly connected superconducting rings. *Phys. Rev.*, 157:317–41, 1967.

[35] A. K. Geim, S. V. Dubonos, J. G. S. Lok, I. V. Grigorieva, J. C. Maan, L. Theil Hansen, and P. E. Lindelof. Ballistic hall micromagnetometry. *Appl. Phys. Lett.*, 71:2379–81, 1997.

[36] S. Pedersen, G. R. Kofod, J. C. Hollingbery, C. B. Sorensen, and P. E. Lindelof. Dilution of the giant vortex state in a mesoscopic superconducting loop. *Phys. Rev. B*, 64:104522, 2001.

[37] Michael Rahm. Herstellung und Charakterisierung ferromagnetischer Nanostrukturen mittels Mikro-Hall-Magnetometrie. Master's thesis, Universität Regensburg, 2000.

[38] Johannes Bentner. Mikro-Hall-Magnetometrie an magnetischen Nanostrukturen. Master's thesis, Universität Regensburg, Oktober 2000.

[39] A. Bauer. Magnetometrie an ferromagnetischen Dot-Arrays. Master's thesis, Universität Regensburg, 10 2000.

[40] F. M. Peeters and X. Q. Li. Hall magnetometer in the ballistic regime. *Appl. Phys. Lett.*, 72:572, 1998.

[41] F. M. Peeters, X. Q. Li, and A. K. Geim. The hall effect of an inhomogeneous magnetic field in mesoscopic structures. *J. Phys. Condens. Matter.*, 9:8065, 1997.

[42] S. J. Bending and A. Oral. Hall effect in a highly inhomogeneous magnetic field distribution. *J. Appl. Phys.*, 81:3721, 1997.

[43] U. Graumann. Ohmsche Kontakte zu zweidimensionalen Elektronensystemen, 1998. unpublished.

[44] M. A. Paalanen, D. C. Tsui, A. C. Gossard, and J. C. M. Hwang. Temperature dependence of electron mobility in GaAs-$Al_xGa_{1-x}As$ heterostructures from 1 to 10 K. *Phys. Rev. B*, 29:6003–4, 1984.

[45] D. Schuh. *Mikro-Hall-Magnetometrie*. PhD thesis, Universität Regensburg, 11 2000.

[46] P. Dubos, P. Charlat, Th. Crozes, P. Paniez, and P. Pannetier. Thermostable trilayer resist for niobium lift-off. *J. of Vac. Sci. and Technol. B*, 18:122–126, 2000.

[47] S. I. Park and T. H. Geballe. Tc depression in thin films. *Physica*, 135B:108, 1985.

[48] T. Hoss, C. Strunk, and C. Schönenberger. Nonorganic evaporation mask for superconducting nanodevices. *Microelectron. Eng.*, 46:149, 1999.

[49] http://www.basf.de/basf/html/plastics/englisch/pages/konstr/ultraso.htm. webpage.

[50] J. L. Vossen and W. Kern. *Thin Film Processes*. Academic Press, Inc., San Diego, 1978.

[51] T. Kontos. *Coherence et Interference Quantiques dans des Nanostructures Supraconducteur/ Ferromagnetique*. PhD thesis, Universite Paris XI UFR Scientifique D'Orsay, 1 2002.

[52] J. Beille. PhD thesis, Universite Joseph Fourier Grenoble, 1975.

[53] L.-P. Lévy. *Magnetism and Superconductivity*. Springer, Berlin, 2000.

[54] V. V. Ryazanov et al. Intrinsically frustrated superconducting array of superconductor-ferromagnet-superconductor π junctions. *Phys. Rev. B*, 65:020501, 2002.

[55] J. M. Martinis, M. H. Devoret, and J. Clarke. Experimental tests for the quantum behavior of a macroscopic degree of freedom: The phase difference across a josephson junction. *Phys. Rev. B*, 35:4682, 1987.

[56] F. W. Grover. *Inductance Calculations: Working Formulas and Tables*. Dover Publ., New York, 1962.

[57] R. Kleiner E. Goldobin, D. Koelle. Semi-fluxons in long josephson 0-pi-junctions. *Phys. Rev. B*, 66:100508, 2002.

[58] T. Gaber D. Koelle R. Kleiner E. Goldobin, A. Sterck. Dynamics of semifluxons in nb long josephson 0-pi junctions. *Phys. Rev. Lett.*, 92:057005, 2004.

[59] J. J. A. Baselmans et al. Direct observation of the transition from the conventional superconducting state to the state in a controllable josephson junction. *Phys. Rev. Lett.*, 89:207002, 2002.

Acknowledgements

This work would not have been possible without the support of many people, whom I would like to express my thanks at this point. Especially I would like to thank ...

- Christoph Strunk, who gave me the chance to participate in his young group as one of his first PhD students. He proposed this experiment and kept me motivated by being interested and supportive at any point of the project.
- Marco Aprili, who provided an essential ingredient for our experiment: the evaporation of Nb and in particular the PdNi alloy. He also shared his long standing experience with ferromagnetic π-junctions and was a valuable discussion partner many times.
- Werner Wegscheider, Matthias Reinwald and Peter Tranitz, who provided us with the starting material for the micro Hall sensor: GaAs/AlGaAs heterostructures containing the 2DEG with tailored properties.
- Dieter Weiss, who shared the infrastructure of his group, among other things all the machines in the cleanroom, which actually made the sample preparation possible.
- Martin Furthmeier, Martin Bachfischer, Uli Gürster and the team from the mechanical workshop for their quick and professional help with any possible an impossible mechanical issues.
- Karl Weigert and Lothar Rother from the helium station for the supply with the cold liquid, we depend on.
- Jonathan Eroms for the introduction to the secrets of PES processing and Claus Zwing at BASF for the supply with Ultrason samples.
- Joachim Stahl and Michael Huber for the AFM investigations.
- My colleagues Franziska and Johannes for sharing the office and a good time.
- The proof-readers: Ivan, Johannes, Leonid and Markus.
- Barbara and Vincent for cheering me up when samples were down.

... and the complete chair for the outstanding working atmosphere.